Dottorato di ricerca in Fisica XXX Ciclo

UNIVERSITÀ DEGLI STUDI DI MESSINA

DIPARTIMENTO DI SCIENZE MATEMATICHE E INFORMATICHE, SCIENZE FISICHE E SCIENZE DELLA TERRA (MIFT)

Pressure dependence of the intermediate-range structure and the boson peak in oxide glasses

PhD Thesis

Giovanna Ruello

PhD Coordinator: ***Prof. L. Torrisi***

Tutor: ***Prof. G. D'Angelo***

SETTORE SCIENTIFICO DISCIPLINARE FIS 01

Anno accademico 2016-2017

"When you are looking, look wide…
And even when you think you are looking wide,
look wider still"

Sir Robert Baden Powell

Introduction

Glasses can be realized with very good homogeneity in a variety of forms and sizes, from small fibers to meter-sized pieces. Moreover, unlike crystalline materials, glasses can be doped with rare earth ions and micro-crystallites, so to change their chemical and physical properties over a very wide range in order to meet the needs of different applications, from photonics to optic fibers and solid-state memories.

However, despite glasses are widely used in several applications, the full understanding of their unique properties is still lacking. In particular, the detailed knowledge of the atomic-scale structure is of great importance.

Another issue of relevant interest is the low frequency dynamics that is characterized by the presence of the 'boson peak', i.e. an anomalous excess of low energy vibrational modes with respect to the corresponding crystalline systems.

The boson peak is a distinctive poorly understood feature of glasses and in general of amorphous systems. Therefore, explaining its origin would permit to clarify the puzzling issues regarding the vibrational dynamics and the structure of disordered systems.

Although the boson peak shows properties, such as its shape, underlining the universality of some characteristics for the amorphous state, its frequency position and intensity strongly depend on the peculiar structure of the investigated system.

Detailed information on the low-energy vibrational dynamics can be obtained by low-temperature specific heat and inelastic neutron scattering measurements, which allow the determination of the vibrational density of states. Raman spectroscopy, as well, represent a valuable technique to investigate low frequency dynamics of amorphous systems.

In this thesis, the issues of the vibrational properties of glasses, the origin and nature of the Boson peak and the structural order on the intermediate length scale will be addressed.

The change of glass composition and of external pressure have been chosen as strategies for elucidating these features.

The investigated samples were a series of alkaline borate glasses $(M_2O)_x(B_2O_3)_{1-x}$, with M=Li, Na, K, Cs ions, a series of permanently densified B_2O_3 glasses and an α-quartz.

These samples have been chosen as model systems because they are being studied from a long time and many of their macroscopic physical and chemical properties are well known. Most importantly, the composition of alkaline borate glasses can be changed in a wide range, whereas the vitreous B_2O_3 can be easily hydrostatically pressurized. These characteristics make these systems interesting for the scopes of the present study.

The thesis is organized into five sections. An overview of the structural and low energy-dynamical properties of glassy systems is given in Chapter 1.

The Chapter 2 shows how these properties change with pressure. A description of the investigated samples is provided in the Chapters 3, whereas the description of Diamond Anvil Cell for high-pressure Raman measurements and an overview of all the experimental techniques used for the present study are given in the chapter 4. Finally, the experimental results and the discussion are illustrated in Chapter 5.

TABLE OF CONTENTS

Chapter 1

LOW ENERGY VIBRATIONAL ANOMALIES IN AMORPHOUS SYSTEMS

1.1 Structural properties of disordered systems

Unlike the well-defined order that distinguishes crystals, the atomic order in amorphous systems is still not completely understood.

The order of a material can be classified in three different levels:

- *short range*, which concerns the nearest neighbor atoms located at distances in the range between 3-5 Å;
- *intermediate range*, which involves structures located on length scales between 5-20 Å;

- *long range*, which interests structures with a reciprocal distance greater than 20 Å.

The atomic arrangement in crystals (Figura 1a) is characterized by a translational periodicity in the disposition of the atoms.

Differently, amorphous systems *(Figura 1b*) exhibit an unordered distribution of constituent atoms, thus not showing any long-range translational order over 20 Å; nevertheless, in glasses (and similarly in gases and liquids) a certain correlation between the atomic positions over the intermediate length scale is typically observed.

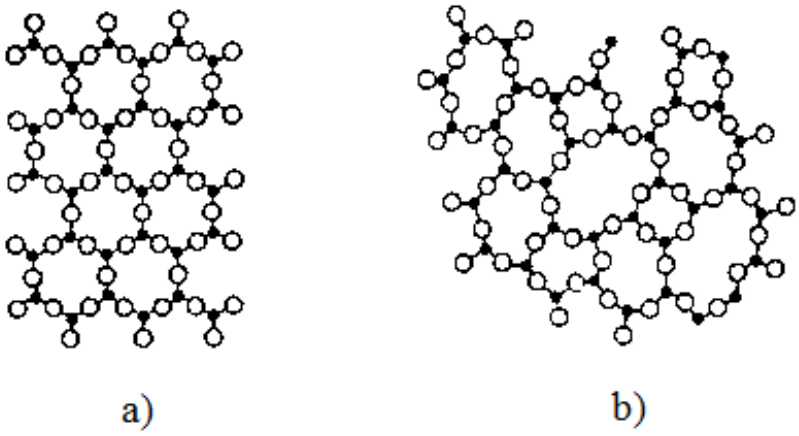

Figure 1. Two-dimensional representation of a) a crystalline structure and b) of its corresponding amorphous structure.

1.1.1. Intermediate Range Structure and the First Sharp Diffraction Peak

The atomic order in the intermediate range scale is peculiar of disordered systems that have predominantly directional bonds and it is generally attributed to the bonding lengths between the nearest neighbor atoms, the coordination number and the bonding angles.

The structural correlations, which define the intermediate range order in glasses, are associated to the appearance in the neutron and X-ray diffraction pattern of a peculiar peak at scattering vector values Q lower than 2 $Å^{-1}$ (1; 2). This peak, named First Sharp Diffraction Peak (FSDP), has been observed in a wide range of disordered systems, including glass-forming liquids, solid glasses, molecular glasses, metallic glasses and polymers (3; 4; 5; 6).

Furthermore, it has a typical full-width at half maximum FWHM of 0.4–0.5 $Å^{-1}$ that is much sharper than the peaks at higher Q.

The modulus of the momentum transfer wave vector Q is defined as

$$Q=4\pi\cdot\sin\theta/\lambda \qquad (1)$$

λ and 2θ being the wavelength of the incident radiation and the scattering angle, respectively. By the Fourier transformation of the structure factor S(Q), it is possible to obtain the corresponding reciprocal r-space, where the components of period $\approx 2\pi/Q \approx$ 4-6 Å are involved (7).

The Fourier analysis on the diffraction components localized in the limited Q region of the FSDP, results in delocalized features in the r space, with width $\approx 2\pi/\Delta Q$ of the order of 15-25 Å. It corresponds to a remarkably long range for materials that by definition have no long range order, but, so far, no exhaustive and clear information about the involved interatomic correlations was given. Moreover, unlike the other peaks in the S(Q), this peak shows

anomalous and puzzling dependences on temperature, pressure and composition:

- *by increasing temperature*, the FSDP intensity increases (see *Figure 2*), unlike the peaks in the S(Q) at higher Q values which follow the behavior predicted by the Debye-Waller model (8; 9; 10);

- *by increasing pressure or density*, the FSDP decreases in intensity and shifts to higher values of Q (see *Figure 3*) (11; 12).

- *by changing the glass composition*, as well as upon the addition of network modifier atoms, the intensity of FSDP markedly changes and/or splits (6; 13; 14; 15).

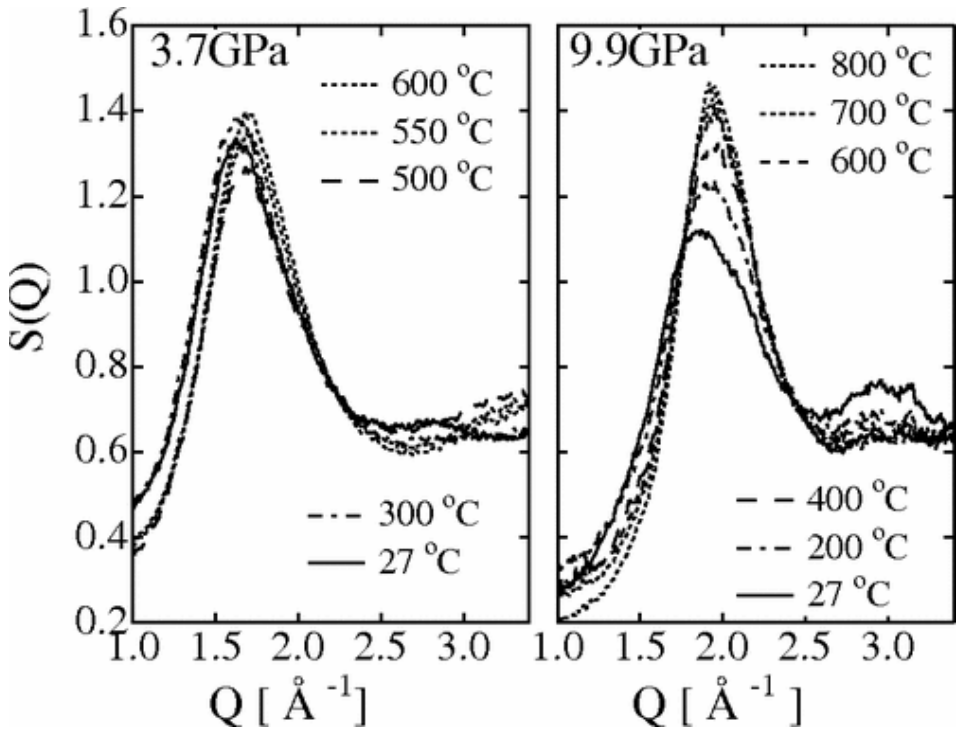

Figure 2. Temperature dependence of S(Q) at 3.7 and at 9.9 GPa of SiO_2 Glass **(9)**.

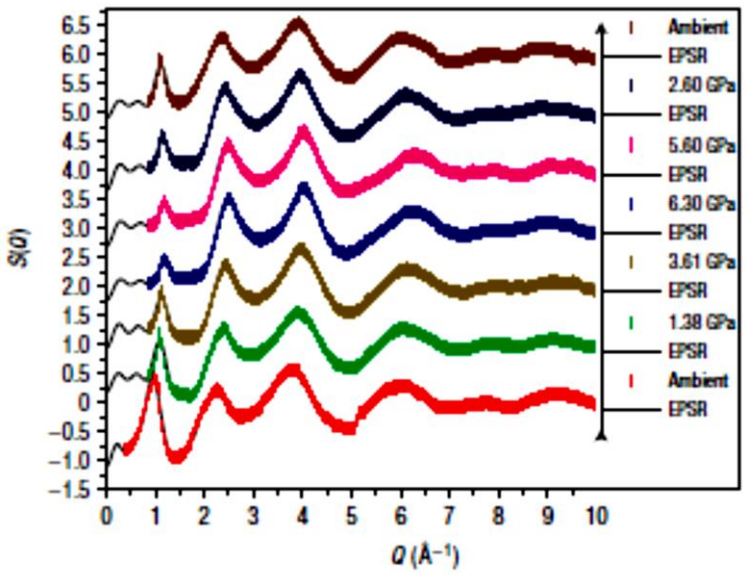

Figure 3. Neutron diffraction pattern for ambient pressure and permanently densified lithium disilicate glasses. Data are vertically offset to enhance clarity **(16)**.

The position Q_1 of the FSDP is related to a real space periodic distance, $d=c/Q_1$ (where c is a constant, whose value has not been yet univocally defined); conversely, the width of the peak is attributed to the damping in amplitude of the real space oscillations even though the origin of such correlations is still unknown.

1.1.2 Structural models for the FSDP in glasses

Several interpretations have been elaborated to justify the structural origin of the FSDP characterizing the intermediate range order in amorphous and glassy systems; however it still remains a subject of theoretical controversy, since no convincing model accounting for all its anomalous behaviors has been proposed yet (17; 18).

Most of the tentative explanations relates the FSDP to the presence of super-structural units (19; 20; 21).

Several authors assume that FSDP arises from an underlying crystalline order (17; 18; 22) or, quite differently, from the chemical ordering of interstitial voids occurring in the structure (15; 23; 24; 25).

The crystalline-like model is based on the hypothesis that the FSDP is the result of a characteristic distance corresponding to the set of Bragg planes in the related crystals with the largest inter-planar spacing (26).

The traces of these lattice planes are believed to remain in the disordered phase and the FSDP is the result of the scattering from these planes: indeed, it had been observed that in many amorphous materials the wave vector of the FSDP is close to the position of the diffraction peak with the lowest wave vector of the related crystalline phase (*Table 1).*

	Q_1 (nm^{-1})	$2\pi/d_{cryst}$ (nm^{-1})	Crystal phase
SiO_2	15.2	15.5	Cristobalite
		15.3	Tridymite
GeO_2	15.5	15.4	Cristobalite
B_2O_3	15.8	22.5	Hex. (high press.)
		10.3, 19.6	Cub. (high press.)
BeF_2	16.3	16.0	Cristobalite-type
GeS_2	10.4	11.0	High temp. mod.
$GeSe_2$	10.1	10.6	High temp. mod.
As_2S_3	12.8	12.7	
$ZnCl_2$	10.8	12.8	(Devit. glass)
		10.2; 11.7; 11.4	$\beta;\gamma;\delta$
$Li_2Si_2O_5$	17.3	17.4	
$Na_2Si_2O_5$	18.3	16.2	
$CaSiO_3$	20.2	21.1	Wollastonit-2*M*
$SrSi_2O_5$	20.4	19.2	Metastable *c*-$SrSiO_3$
		21.7	Stable *c*-$SrSiO_3$
$LiAlSi_2O_6$	16.1	18.0	β spodumene
l-$ZnCl_2$	10.1	10.2; 11.7; 11.4	$\beta;\gamma;\delta$
l-$ZnBr_2$ (693 K)	9.4	10.0	(25 kbar)
l-ZnI_2 (743 K)	8.8	9.0	
l-$NiCl_2$	9.9	10.9	
l-$NiBr_2$	9.2	10.3	
l-NiI_2	8.8	9.6	

Table 1. *Comparison of the position Q_1 of the FSDP, for several glass and liquid systems, with $2\pi/d_{cryst}$, d_{cryst} being the lattice spacing of the first peak obtained by X-ray diffraction in compositionally similar crystals* **(26)**.

The FSDP position, Q_1, is related to the interlayer separation D via the relation (27)

$$Q_1 \sim 2\pi/D \qquad (2)$$

A more wide-ranging explanation for the origin of the FSDP is provided by the void-based model (28), which attributes the FSDP to structural voids, whose presence is a distinctive feature of glasses.

This model interprets the FSDP in the structure factors of covalent glasses as a pre-peak in the concentration-concentration structure factor due to the chemical short range ordering of interstitial voids around cation-centered clusters. The Elliott's model gives a satisfactory explanation also for network-modified glasses (i.e. glasses with a considerable amount of network modifiers in the structure), proposing a simple interstice-stuffing model, in which the network-modifying ions (NMI) occupy the structural interstices.

A decreased intensity of the FSDP is predicted if the filling ion has a positive neutron scattering length, whereas an increased intensity of the FSDP is foreseen if the network-modifying ion has a negative neutron scattering length.

Unfortunately, despite the merit of their generality and simplicity, both the crystalline- and the void-based models are found to generate contradictory results, being so dependent on the specificity of the questioned system.

The crystalline-like model is inconsistent with some experimental observations, such as the unjustified persistence of the FSDP into the liquid (29), or the evidence of layered-like structures in systems which do not exhibit a FSDP (4).

Furthermore, more recently, ab initio study has shown that the appearance of the FSDP is not correlated to crystalline-like layers, while cluster–void correlations were found (30).

Even the Elliot's void–cluster-based model is not infallible: it fails to justify the appearance of a pre-peak in the FSDP region of glassy networks

modified by the addition of metal cation (31; 32); furthermore, this model has been ruled out by evidence of the lack of a FSDP in the concentration-concentration partial structure factor of silica glasses (6).

Nevertheless, it is worth to note that, despite some inconsistencies, the Elliot's model has lately received a renewed interest.

In fact, recent atomic resolution transmission electronic microscopy measurements (33) have evidenced the existence of a continuous random network of rings in two-dimensional silica glasses, giving new support to the idea that voids could be the key to explain the microscopic origin of the FSDP.

Very recent investigations of the structure of a series of alkaline borate glasses on the intermediate range length scale have shown that the FSDP in the structure factor is preceded by a pre-peak (15), whose position and intensity depend on the content and type of metal oxide added. Then, a revised void-based model has been proposed, in which the FSDP in glasses arises from the periodicity of boundaries of small voids, homogeneously distributed in the network.

1.2 Vibrational dynamics in disordered systems

In solid systems, the atoms execute small oscillations around their equilibrium positions at every temperature, both at the absolute zero, as a result of zero-point motion and at high temperatures, as a result of thermal fluctuations.

Vibrational states of periodic crystals can be well described as quantized plane-waves (phonon modes), but the nature of vibrations in amorphous systems remains difficult to understand.

Furthermore, topologically disordered systems exhibit unusual thermal, vibrational and dynamics properties when compared with their crystalline counterparts, such as the acoustic dispersion and attenuation, the thermal conductivity and expansion, the low temperature specific heat, the low frequency inelastic Raman scattering and the vibrational density of states.

1.2.1 Vibrations in solid

The theory of the dynamical properties of a solid can be treated by using two approximations: Born-Oppenheimer and harmonic approximations. The first is the adiabatic approximation, which allows to separate the electronic dynamics from the nuclear one. The second one is based on considering the hypothesis of small nuclear oscillations around the equilibrium positions. The adiabatic approximation permits to describe the vibrational dynamics of a system of N atoms in positions{r}, by a Hamiltonian of the form:

$$H = \frac{1}{2}\sum_{\alpha i} m_i \dot{r}_{\alpha i}^2 + V(r_1,...,r_N) \qquad (3)$$

where α indicates a Cartesian coordinate, m_i is the mass of the i^{th}-atom, and V (r_1; r_2, ..., r_N) is the N-body potential which describes interactions of all atoms in the solid. Since, the atomic motions are small displacements *u* around an equilibrium position r_0, hence r_i can be written as

$$r_i = r_{0i} + u_i \qquad (4)$$

The use of the harmonic approximation simplifies the formula of the potential V, which, as a matter of fact, can be expanded in series of u's until the first non-vanishing term, which is the quadratic one:

$$V = V_0 + \sum_{n\alpha i} \frac{\partial V}{\partial u_{n\alpha i}} u_{n\alpha i} + \frac{1}{2} \sum_{n\alpha i n'\beta j} \frac{\partial^2 V}{\partial r_{n\alpha i} \partial r_{n'\beta j}} u_{n\alpha i} u_{n'\beta j'} \qquad (5)$$

where n runs over the number of Wigner-Seitz cells in the volume of the material N; α runs over the number of atoms in the basis r; i is one of the three Cartesian coordinates.

The first term in this expansion is constant and represents the potential energy of the ion lattice in equilibrium. It can be omitted since does not appear in equations of motion. The second term is linear in $u_{n\alpha i}$ and it disappears because only equilibrium positions are considered. The third term is usually written in the following form:

$$\frac{1}{2} \sum_{n\alpha i n'\beta j} \frac{\partial^2 V}{\partial r_{n\alpha i} \partial r_{n'\beta j}} u_{n\alpha i} u_{n'\beta j} = \frac{1}{2} \sum_{n\alpha i n'\beta j} \Phi^{n'\beta j}_{n\alpha i} u_{n\alpha i} u_{n'\beta j} \qquad (6)$$

where the force constant matrix $\Phi^{n'\beta j}_{n\alpha i}$, having 3rN rows and columns, represents the force in the i-th direction acting on the α-th atom in the n-th cell, when the β-th atom in the n'-th cell is displaced by unit distance in the j-th direction.

On these bases, the Hamiltonian of the system becomes:

$$H = \sum_{n\alpha i} \frac{m_\alpha}{2} \dot{s}^2_{n\alpha i} + \frac{1}{2} \sum_{n\alpha i n'\beta j} \Phi^{n'\beta j}_{n\alpha i} u_{n\alpha i} u_{n'\beta j} \qquad (7)$$

where m_α is the mass of the α–th atom and $u_{n\alpha}$ is the instantaneous vector displacement from equilibrium. Therefore, we can write the equations of motion of the system as:

$$m_\alpha \ddot{u}_{n\alpha i} = -\sum_{n'\beta j} \left. \frac{\partial^2 V}{\partial r_{n\alpha i} \partial r_{n'\beta j}} \right|_0 u_{n'\beta j} = -\sum_{n'\beta j} \Phi^{n'\beta j}_{n\alpha i} u_{n'\beta j} \qquad (8)$$

Considering a solution that is periodic in time, having thus the form of a plane wave $u_{n\alpha i}(t) = \sqrt{m_\alpha} u_{n\alpha i} e^{i\omega t}$ (where $u_{n\alpha i}$ are time independent), Equation 8 may be rearranged in:

$$\omega^2 e_{n\alpha i} = \sum_{\mathbf{n'\beta j}} \mathbf{D}^{\mathbf{n'\beta j}}_{\mathbf{n\alpha i}} \mathbf{u}_{\mathbf{n'\beta j}} \qquad (9)$$

The problem is thus reduced to an eigenvalue problems for the 3N x 3N matrix D, whose elements are:

$$D^{n'\beta j}_{n\alpha i} = \frac{\Phi^{n'\beta j}_{n\alpha i}}{\sqrt{m_i m_j}} \qquad (10)$$

The real symmetric matrix D is called dynamical matrix, it has 3Nr real eigenvalues ω^2_k and the 3N-dimensional eigenvectors u_k are called normal modes.

In this way, the coupled oscillations of the atoms are replaced formally by decoupled collective excitations, the phonons.

1.2.2 Vibrations in crystal and glasses

In the case of a perfect crystal the situation is simplified by considering the lattice periodicity.

The Bloch theorem allows to restrict the problem to a single unit cell of r atoms. Moreover, the vibrational eigenvectors in a crystal will be plane waves, labeled by well-defined wave vectors q, lying in the First Brillouin zone.

In a quantum mechanical description, the 3N decoupled collective vibrations of a crystal can be described in terms of bosonic quasi particles called phonons. For each allowed q there are 3r real eigenvalues denoted as $\omega_k^2(q)$ and the frequencies $\omega_k(q)$ are real for the stability of the lattice.

For each q, the 3r functions can be regarded as branches of a multivalued function and the relation $\omega = \omega(q)$ is defined dispersion relation.

In general, there are three branches called acoustic branches for which $\omega(q)$ goes to zero when q approaches zero. In this case, the vibrations of the atoms are in phase and there are one acoustic mode with longitudinal polarization and two with transverse one.

If $r > 1$, moreover, there are further $3(r-1)$ optic branches. These branches tend to a finite value as q approaches zero and if $q=0$ the basis atoms vibrate against each other.

These conclusions in harmonic approximation do not hold in the case of amorphous solids, not allowing to predict the damping of the vibrational excitations.

Because of the loss of periodicity, there are no restrictions to the values that the quantum number q can take. Thus, several vibrational modes with the same frequency, but different values of q, can coexist in amorphous solids.

As it is possible to observe in the schematic representation of the dispersion curve in Figure 4, ω doesn't follow a single curve vs q.

The curve shows that q is well defined at small wave-vector values, while at larger q-values the uncertainty in q considerably increases.

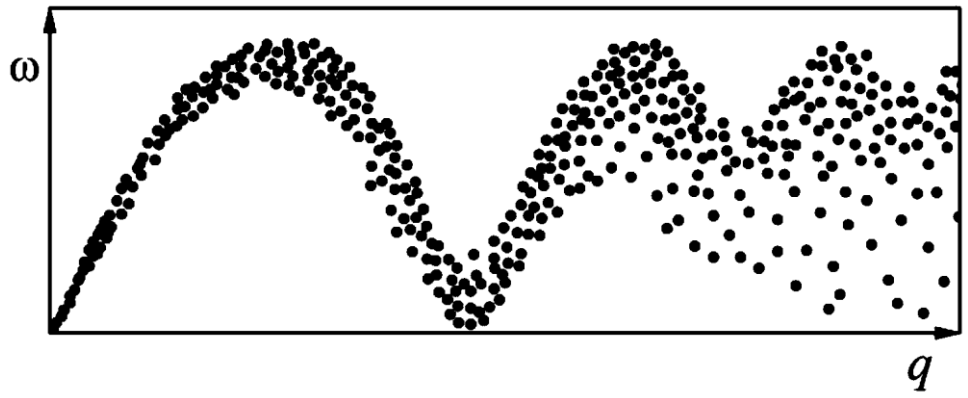

Figure 4. Schematic representation of the dispersion curve ω (q) of an acoustic branch in a glass.

This is due to the fact that, at low frequencies, i.e. in the long wavelength limit, a glass appears as an elastic continuum medium and the disorder does not affect the vibrational dynamics. By increasing the q-value, the excitation wavelength becomes shorter and the local structure is more and more relevant.

As q approaches to zero, the vibrational excitations have the characteristic of linearly propagating acoustic waves, with speeds of sound v_L and v_T and the two transverse branch are degenerate because of the isotropy. At higher q-values, the well-defined sound waves turn into a complex pattern of atomic motions that mirrors the structural disorder.

Moreover, although the Brillouin zone is not rigorously defined, the dispersion relation shows a structure which can be related with the peaks of the static structure factor S(Q) which act as smeared reciprocal lattice vectors.

1.2.3 The vibrational density of states

To describe the vibrational properties in crystals as well as in disordered systems we can use the vibrational density of states (VDOS), which is defined as:

$$g(\omega) = \sum_k \delta(\omega - \omega_k) \tag{11}$$

where g(ω)dω is the number of vibrational states having frequencies between ω and ω + d ω.

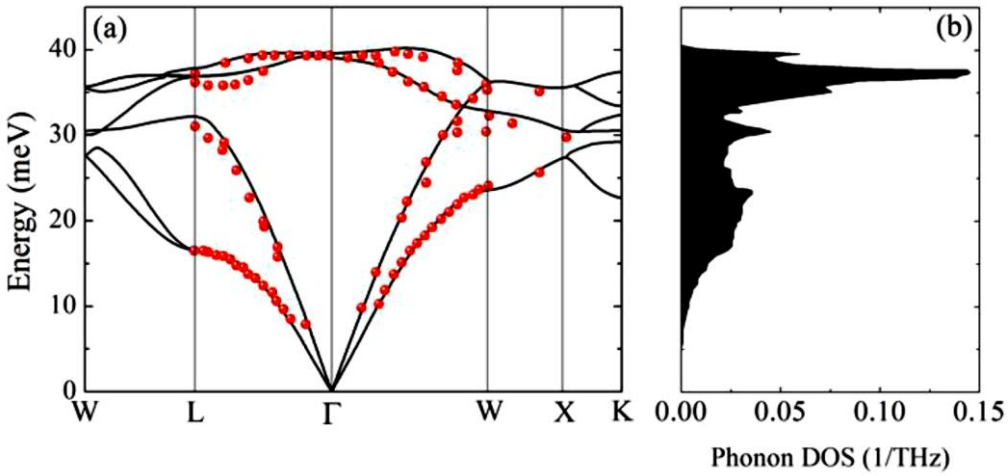

Figure 5. a) Phonon dispersion relation and b) phonon density of states VDOS of diamond. Solid curves show the calculated dispersions. Experimentally, dispersion relations over the Brillouin zone have been obtained by measurements such as neutron scattering, electron energy-loss spectroscopy, and x-ray scattering techniques **(34)**.

In crystals, the sum over k is executed over all branches and covers the first Brillouin zone. The relation between the dispersion curve and the DOS of a crystal is shown in Figure 5: the peaks in the DOS of a crystal are associated with the Van Hove singularities that define the regions where the dispersion curve is flat ($\partial\omega/\partial q = 0$).

In glasses, the index k in Equation (11) is a label for the vibrational eigenstates. The typical sharpness of the crystalline DOS disappears and the Van Hove singularities are smeared out as a consequence of the finite width of the energy distribution of vibrational excitation about a given q value.

The vibrational density of states represents a link between a microscopic description of a solid and its macroscopic properties. Therefore, knowing the g(ω) we can derive thermodynamic properties such as the heat capacity C and the thermal conductivity κ.

1.2.4 Low temperature properties and specific heat

The differences in the structures between glasses and crystals are considered responsible for the peculiar glassy anomalies observed in various physical properties, as the low temperature thermal properties.

Thermal properties in crystals are predicted by the Debye's theory, proposed in 1912 (35). Statistical mechanics describes atoms in solids as harmonic oscillators, and their specific heat is obtained by differentiating the average total energy of the system (36):

$$C_V = \frac{1}{V}\frac{\partial \bar{E}}{\partial T} = 3nNk_B \int \frac{\left(h\upsilon_q / K_B T\right)^2 e^{\hbar\omega_q / K_B T}}{\left(e^{\hbar\omega_q / K_B T} - 1\right)^2} D(\omega) d\omega \qquad (12)$$

where D(ω) is the density of vibrational states and D(ω)dω is the fraction of modes within the frequency range ω, ω +dω. Equation (12) can be solved only if the analytical expression of the density of vibrational states is known.

Debye proposed two simplifications. First of all, he considered the acoustic modes all having the same constant sound velocity v_D. Since the sound velocity depends on the crystallographic direction of propagation and on the two different types of acoustic modes longitudinal and transverse, Debye defined v_D as a weighted average of longitudinal v_l and transverse velocities v_t:

$$\frac{3}{v_D^{\ 3}} = \frac{1}{v_l^{\ 3}} + \frac{2}{v_t^{\ 3}} \tag{13}$$

The second hypothesis formulated by Debye concerns the Brillouin zone (BZ) and affects the integration limits: Debye replaced the true shape of BZ with a sphere having the same volume in reciprocal space. This assumption implies the existence of a maximum allowed wavevector for lattice waves, the Debye wave-number q_D equal to $q_D = (2\pi\rho_N)^{1/3}$ and corresponding to the typical inverse inter-particle distance of the system. The wave-number q_D is associated to the so-called Debye frequency ω_D, defined as

$$\omega^3{}_D = 6\pi^2 \rho_N v_D^3 \tag{14}$$

The VDOS predicted by the model has the following form

$$g(\omega) = \frac{3}{\omega^3{}_D}\omega^2 \tag{15}$$

In this framework, Equation 12 becomes:

$$C_V = 3nNk_B\left(\frac{T}{\Theta_D}\right)^3 3\int_0^{\Theta_D/T}\frac{z^4 e^z}{\left(e^z-1\right)^2}dz \qquad (16)$$

where $z=\hbar\omega/KT$ and Θ_D is the Debye temperature which is defined by $k_B\Theta_D=\hbar\omega_D$.

When T/Θ_D is large ($T>>\Theta_D$), the upper limit in the integral is small, so the integrand can be expanded giving the Dulong - Petit law:

$$C_V=3Nk \qquad (17)$$

At low temperatures ($T<\Theta_D$), the upper limit Θ_D/T can be taken as infinite so the integral tends to a known value and the specific heat becomes:

$$C_V=\frac{12\pi^4}{5}Nk_B\left(\frac{T}{\Theta_D}\right)^3 \qquad (18)$$

Equation (18) represents the well-known T^3-law of specific heats, valid only at low temperatures.

Since at temperatures lower than Θ_D (the temperature needed to excite all the acoustic modes) the mean free path of phonons is high, it is expected that structural disorder is unimportant; therefore, amorphous and crystalline solids could be both described within the same approximation, resulting in the same thermal properties.

However, this is not experimentally observed: in many types of glasses the low temperature specific heat C_v increases linearly with the temperature T, unlike T^3 as expected from the Debye model.

The Figure 6 shows the specific heat Cv measured in both crystalline (α-quartz) and amorphous SiO_2: the two systems display a markedly different behavior in the low temperature range: the heat capacity of crystalline quartz data follow the Debye ~ T^3 behavior, described by Equation

$$C_V = \frac{12\pi^4}{5} N k_B \left(\frac{T}{\Theta_D} \right)^3 \tag{18}$$

whereas the specific heat of the vitreous silica decreases much more slowly with temperature than predictions and its trend can be described by an equation of the form:

$$C_v = aT + bT^3 \tag{19}$$

where the coefficient b exceeds the values predicted by Equation (18).

The thermal properties of glasses can be described separately in two temperature regimes. For T > 2K the theoretical models suit well to experimental data; for T < 2K the specific heat is essentially linear in temperature, indicating an approximately constant density of states in addition to the Debye one.

As it is possible to see in Figure 6 b), in the region T > 2K, the reduced glassy heat capacity C_V/T^3 exceeds the crystalline one. Both phases show a asymmetric band at about 10 K (37), which reflects the presence of an excess of modes in the vibrational density of states g(ω) over the Debye density of states $g_D(\omega)$: in crystalline system, it is related to an excess of the transverse acoustic vibrational excitations near the boundary of the First Brillouin zone;

in glassy system this hump appears shifted to lower temperatures, also showing an increased magnitude.

The presence of an excess specific heat at low temperature is a distinctive feature of all glassy and amorphous investigated systems and the question of its origin is far to be completely clarified.

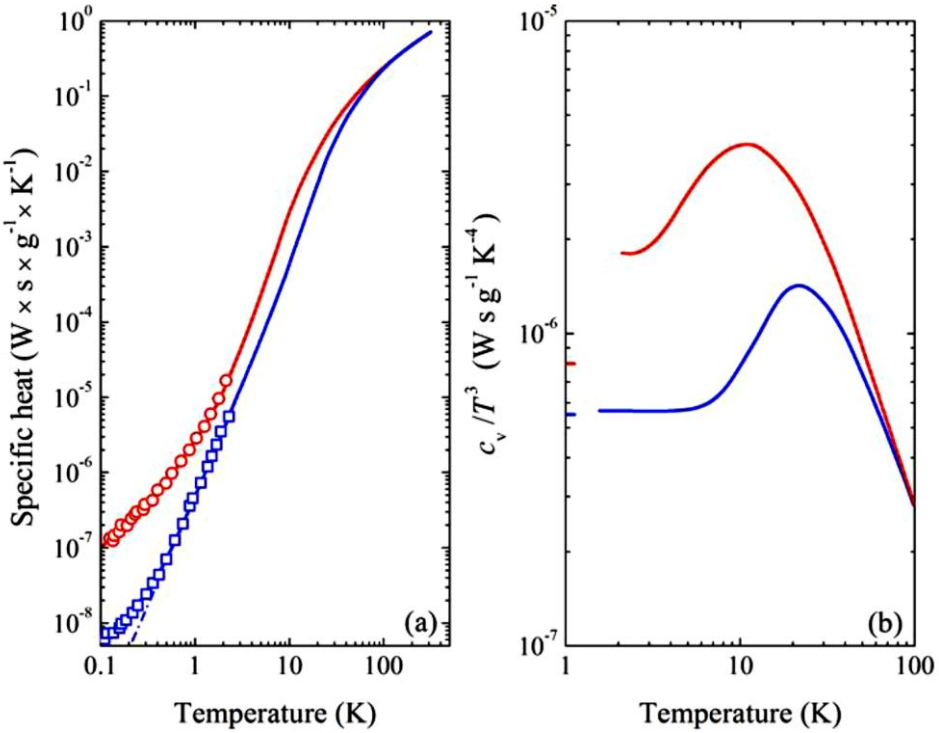

Figure 6. a) Specific heat of vitreous SiO_2 (red circles), compared with that of crystalline α-quartz (blue squares). b) Specific heat divided to T^3 for crystals (blue line) and glass (red line); dashed lines are the Debye model predictions **(38)**.

1.2.5 The excess of vibrational states vibrational density of states and the Boson Peak

The excess of specific heat, observed in glassy systems at temperature above 1K, is related to the presence of an excess in low energy vibrational states. It is usually observed as a broad bump in the energy region lying between 2 and 10 meV of the vibrational density of states $g(E)/E^2$, and usually referred to as the "Boson Peak" (BP), because its intensity scales with temperature approximately following the Bose Einstein statistics.

Although the BP has been observed in a wide range of materials, both in experiments (Raman, neutron, X-ray, and other inelastic scattering experiments (39; 40; 41; 42) and in computer simulations (43; 43), its physical origin and the nature of the modes responsible for this excess are object of a very intense and controversial debate (44; 45; 46).

In particular, although a peak is often present in the reduced density of states $g(E)/E^2$ of the crystalline phase, it is found at lower frequencies and with an enhanced intensity in the glassy counterpart, indicating the existence of an higher number of low energy states.

Moreover, its energy (or frequency) position and intensity depend strongly on the peculiar structure of the investigated system, and consequently on the chemical bonds of the atoms forming the network: the number of modes contributing to this peak results higher in strong (like covalent systems) than in fragile glasses (molecular and ionic systems) (47).

Therefore, a study of the changes of BP in intensity, position or width induced by variations of external parameters (i.e. pressure, temperature, composition) would let to explain the nature of low energy vibrational modes.

Numerical simulations (48) and recent experimental investigations (49) on several glass-forming systems showed that an increase in BP position and a decrease in its intensity take place if a hardening of the medium occurs (see *Figure 7*).

This behavior has been tested for hardening of the systems originated by temperature (50) (51), aging (52) or densification (due to an increased polymer connectivity (53) or to applied pressure (42)).

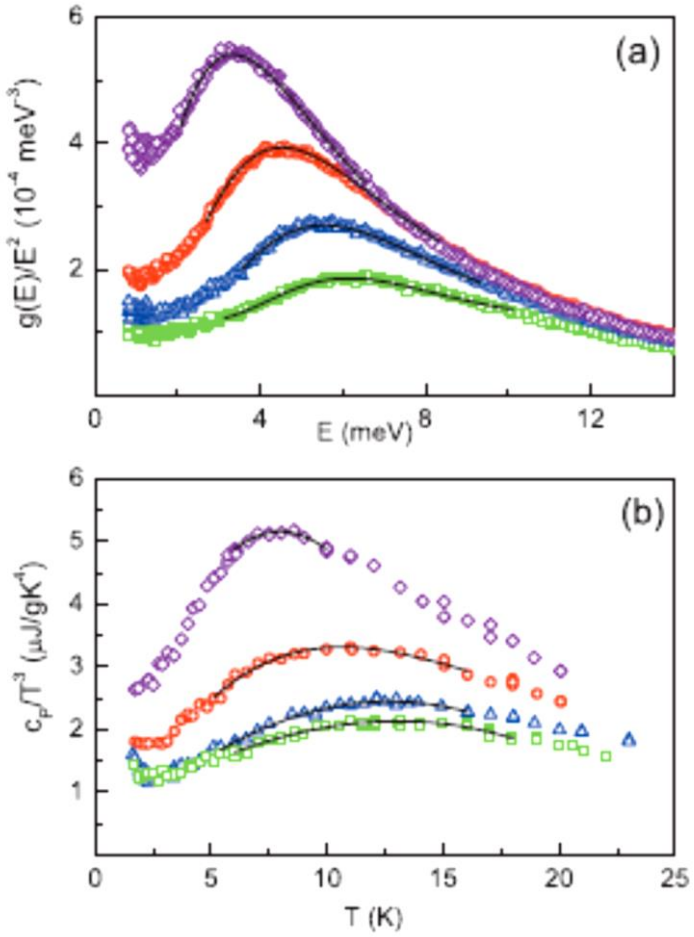

Figure 7. (a) Reduced density of vibrational states $g(E)/E^2$, obtained by Inelastic Neutron Scattering, of normal GeO_2 glass (violet diamonds) and permanently densified samples: 2 GPa (red circles),4 GPa (blue triangles), and 6 GPa (green squares); (b) Temperature dependence of C_p/T^3 for permanently densified glasses (49). *The continuous lines represent the fits of the data.*

1.2.6. Experimental determination of vibrational density of states

The nature and type of vibrations occurring in systems can be investigated by several experimental techniques. Since it is believed that the Boson peak is related to an anomaly in the density of states g(ω), this is the actual quantity to be determined.

In particular, in glasses the density of vibrational states can be directly determined by means inelastic neutron scattering, low frequency light scattering experiments (Raman) or measurements of low temperature specific heat.

The equation that relates the density of states to the specific heat (54) is given by:

$$C_V = \frac{\partial}{\partial T}\int g(\omega)\langle n(\omega)\rangle \hbar\omega d\omega \tag{20}$$

Therefore, if C_V is measured, g(ω) can be determined within an additive constant.

In the case of first-order Raman scattering on a disordered system, the Raman experimental intensity is proportional to the vibrational density of states g(ω). For a Stokes process, the relation between the Raman scattering intensity and the density of vibrational states is given by the following equation (55):

$$I_{\exp}(\omega) = \frac{C(\omega)g(\omega)[n(\omega,T)+1]}{\omega} \tag{21}$$

where ω is the frequency shift, given by the difference between the incoming radiation frequency and the scattered light frequency; I(ω) is the Stokes component of the Raman scattering intensity; n(ω) is the Bose factor; C(ω) is the Raman phonon-photon coupling coefficient.

Removing the trivial temperature dependence given by the Bose factor and dividing by ω, we obtain the so called reduced Raman intensity $I_N(\omega)$ which is directly proportional to $g(\omega)/\omega^2$ trough the coupling function $C(\omega)$:

$$I_N(\omega) = \frac{I_{\exp}}{\omega[n(\omega,T)+1]} = C(\omega)\frac{g(\omega)}{\omega^2} \qquad (22)$$

The Raman spectrum in solids can be usually divided in two parts:

- *the low frequency region* (below 100 cm^{-1})
- *the high frequency region* (above 100 cm^{-1})

The low frequency range is characterized only by acoustic-type vibrations, while the high frequency region is connected to optical phonons.

Owing to photon properties, Raman spectra of crystals do not exhibit any contribution in the acoustic range of vibrational states below 100 cm^{-1}. This is due to the fact that light photons have wave-vector of the order of 10^5 cm^{-1}, while the first Brillouin zone is about 10^8 cm^{-1}; so only information at q=0 is provided. Thus the acoustic contributions never appear, since their dispersion curves are almost zero in this region.

In glassy systems, the low frequency region can be further divided in:

- *the Boson peak region* (above 10 cm^{-1})
- *the quasi-elastic scattering region* (below 10 cm^{-1})

The quasi elastic scattering contribution (QES) appears as a strong peak centered at ω=0 and having a characteristic width of a few cm^{-1}. It dominates the Raman spectra at frequencies below 10 cm^{-1} and exhibits a strong temperature dependence. Although many models have been suggested to explain the QES, its nature is still a matter of intensive debate.

Scattering of photons on structural relaxations or scattering of photons by vibrations, which are damped by some relaxations are the most prevalent interpretations.

On the other hand, the spectral region above 10 cm^{-1} is dominated by the presence of the broad asymmetric peak, which is the Boson Peak.

1.2.7 On the origin of the Boson Peak

It is believed that understanding the behavior of the boson peak is the key to clarify the anomalies of the vibrational states of glassy and amorphous materials, which are beyond the simple plane-wave phonon picture valid for crystals.

A common consensus considers the boson peak as an expression of the structural disorder. However, its physical origin is a controversial topic in condensed-matter physics and materials science: different theoretical interpretations have been suggested that include localized vibrational states (56), soft anharmonic vibrations (44), intrinsically diffusive relaxational motions (57; 58) and propagating modes (59). Two points of views can be mainly distinguished to sum-up all the phenomenological and material-specific models concerning the nature of the Boson Peak:

- the first one attributes the origin of BP and the anomalies in the low temperatures thermal properties to propagating acoustic modes in the regime where the structural disorder comes into play (41; 60);
- the second one ascribes this excess in the density of states to the localizations of phonons strongly scattered at the BP energy or strictly introduced by the disorder (61). In this regards one of the most interesting model is the soft potential model (SPM) (62).

In particular, the SPM assumes the existence in glasses of some typical soft structure (defects with very small elastic constants) whose dynamics can be described by soft anharmonic potentials with parameters distributed according to a probability law because of the randomness of their local environment. The resulting potentials can be single (soft vibrations) or double wells and, depending on barrier height, it gives additional tunneling states and relaxations.

It is also worth mentioning the models with spatially fluctuating elastic constants, the most important of which was proposed by Schirmacher (63; 64). He solved a fluctuating force-constant scalar-vibration model using a Gaussian distribution of nearest-neighbour force constants, with a lower cutoff, which also include the negative force constants. The disorder in this model was found to give rise to a BP. Schirmacher showed that shifting the cutoff of the Gaussian distribution down, the disorder increases leading to downshift of the maximum of the Boson peak and to a simultaneous increase in intensity. Furthermore, he found that shifting the cutoff below a critical negative value led to an instability and concluded that the Boson peak is a precursor of an elastic instability.

Other recent advances consider the boson peak as being the result of the contribution of a transverse acoustic branch (65). Indeed, in glasses, a further peak, in addition to that associated with the acoustic longitudinal modes, occurs in the spectra of the dynamic structure factor S(Q,E) at high Q-values (at least above $Q_0/2$, Q_0 being the position of the FSDP), whose position is weakly Q-dependent and the intensity increases with Q. The origin of this behavior seems to be harmonic and suggests the existence of a transverse dynamics: the presence of transverse vibrational modes in a longitudinal spectrum derives from the fact that the polarization characteristic of a mode is well defined only in the limit of large wavelengths (i.e. low Q). Conversely, it is loosely defined at small wavelengths, especially in the range where the wavelength is comparable with the scale of the topological disorder. In this limit condition, it is no longer possible to define a purely transverse or

longitudinal excitation. This explains why we can better observe the transverse dynamics with the increase of Q. According this theory, the excess of the BP arises from the states related to the transverse modes. This idea is validated by the experiments on vitreous silica and glycerol where the boson peak has its maximum at the same energies at which the transverse excitation is revealed in the dynamic structure factor (65; 66).

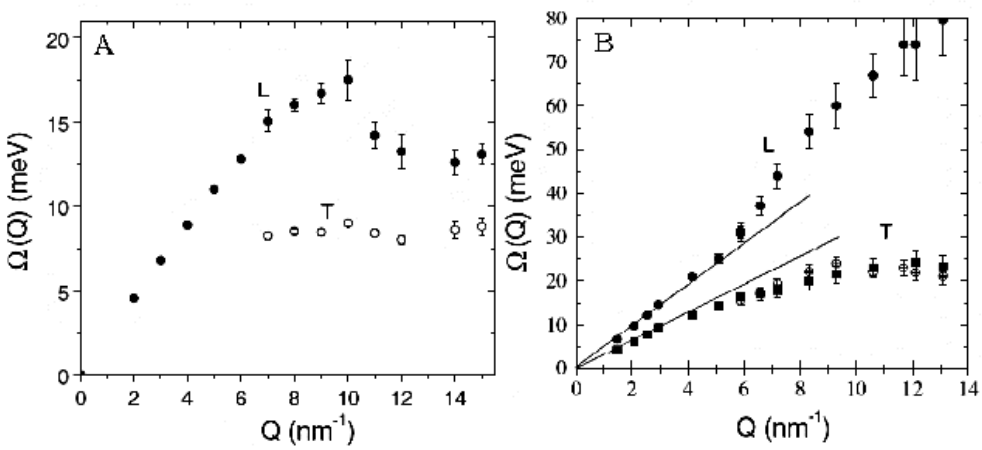

Figure 8. Dispersion curves for a) glycerol and b) vitreous silica. The transverse branches are responsible for the excess states, which generates the boson peak (65; 66).

1.3 Relations between structure and dynamics in glassy systems

A full comprehension of the origin of the FSDP can provide useful information to clear up unsolved questions on the Intermediate Range Order of glasses, but also would allow to explain other anomalous behaviors of glasses. Indeed, recent emerging studies support the existence of a strict relation between the structural correlations of glasses in this length scale and their low energy thermal and vibrational properties, as well as on their

stability (67). In particular, it has been found that the wavelength associated to the low frequency modes in amorphous systems lies just in the length scale of the IRO, defining the size of structural heterogeneities (68; 69). Moreover, the IRO limits the thermal conductivity by means the strong scattering of acoustic phonons (10). Therefore, the Boson Peak and the FSDP, both features typical of glasses, are related to properties of the intermediate range scale.

Importantly, many attempts have been executed to correlate the structural length scale ascribed to the position of the FDSP to a dynamic length scale associated to the position of the Boson Peak (8; 70; 71; 72; 73).

In particular, Elliot in his investigations shows correlations between the position of the FSDP Q_1 and the wavevector Ω, corresponding to the maximum frequency of the boson peak ω_m (8).

He assumes that the frequency ω_m of the Boson Peak in Raman spectra is determined by a characteristic length scale of the amorphous solid, the diameter of the density-fluctuation domains 2L. If the dispersion relation $q \approx \frac{\omega}{\bar{v}}$ for propagating phonons in the Debye approximation is supposed valid, then

$$\omega_m \approx \frac{\bar{v}}{2L} \tag{23}$$

with $\bar{v}$ is the average sound velocity.

The length scale is defined by $L \approx \alpha D$, where α is a coefficient between 3 and 4 and D is equal to the nearest neighbor cation-cation distance. The FSDP position Q_1 is approximately given by the relation

$$Q_1 \approx \frac{3\pi}{2D} \tag{24}$$

Thus, combining Equation (23) and (24), we obtain finally:

$$Q_1 \approx 3\pi\alpha \frac{\omega_m}{\bar{v}} . \qquad (25)$$

Therefore, by plotting the experimental data of Q_1 as a function of the wavevector $\Omega \approx \frac{\omega_m}{\bar{v}}$, a correspondence has to be found.

In *Figure 9*, a plot of Q_1 as a function of Ω is shown for a variety of amorphous solids.

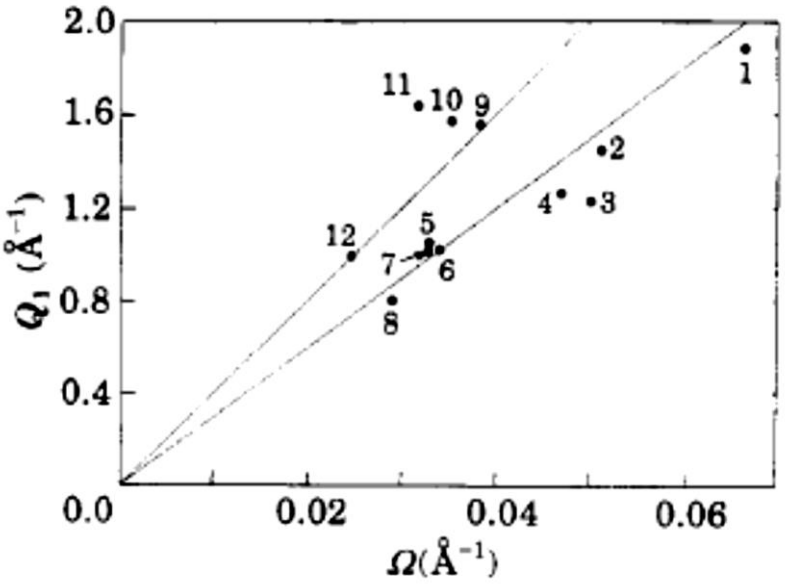

Figure 9. Plot of experimental values for the FSDP position Q_1 as a function of normalized Boson Peak frequency Ω for 1)Ge; 2)Se; 3)As_2Se_3; 4)As_2S_3; 5)$GeSe_2$; 6)$SiSe_2$; 7)$GeSe_2$; 8)AgI-AgO-B_2O_3; 9)SiO_2; 10)BeF_2; 11)B_2O_3; 12) PMMA. The straight lines are theoretical predictions of the model with gradients of 30 and 40 **(74)**.

The experimental data show a very well accordance with the lines having the predicted gradient $3\pi\alpha \approx 30 \div 40$, confirming the existence of a correlation between these two characteristic features of amorphous systems.

Another meaningful study of Sokolov has shown a strong correlation between the position of the Boson peak in Raman spectrum and the half-width of the FSDP ΔQ_1 for different glasses (75).

Indeed, if the position of a peak in the diffraction pattern is associated to some repetitive characteristic distances between structural units, then a correlation length will generate a broadening of the peak itself. To evaluate the correlation length, D, a simple expression $D \approx \frac{2\pi}{\Delta Q}$ is used. A good correlation has been observed between the correlation length D and the dynamic correlation length obtained from the Boson peak frequency

$$L = v_t / 2\pi c \omega_{BP} \qquad (26).$$

Furthermore, Greaves and co-workers, in investigating the low-frequency vibrational properties of zeolites crystals and on their compounds at different stages of amorphization, ascribed the excess of low energy modes compared to the Debye model (the Boson peak) found in high resolution inelastic neutron scattering measurements to the coupling of oscillations between connected rings of many sizes (76). These rings build up different structural units (α-cage, β-cage, D6R), whose frequencies of the fundamental normal modes (indicated by arrows in Figure 10) are found, to a first approximation, as $\frac{v_t}{L}$ and $\frac{v_l}{L}$, where v_t and v_l are the transverse and longitudinal sound velocities in zeolites and L is the circumference of the ring.

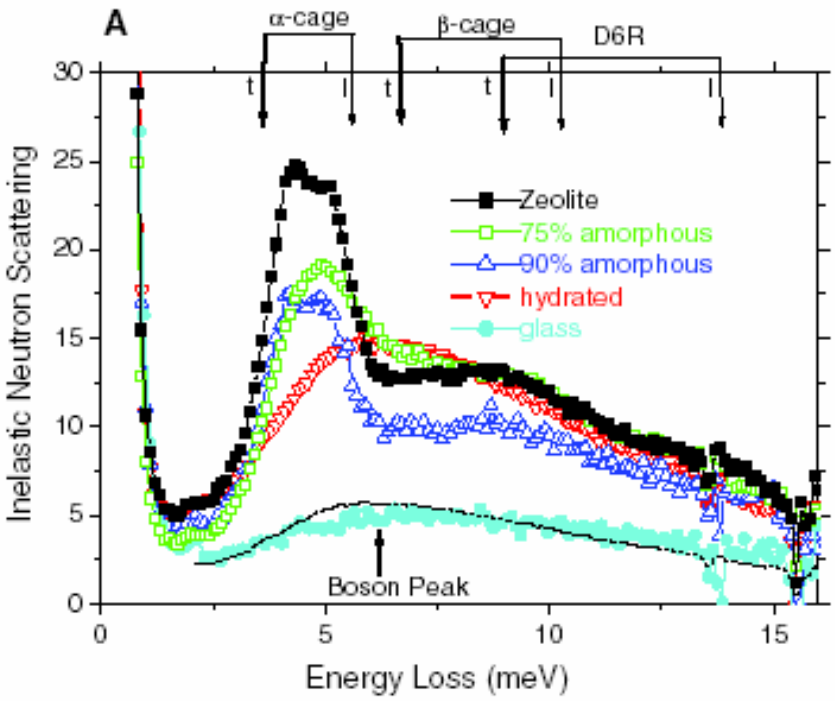

Figure 10. High resolution inelastic neutron scattering profiles at 20 K for anhydrous and hydrated zeolite crystals and their anhydrous compounds at different stages of amorphization. The bands at 4,5 and 9 meV of anhydrous zeolite are present even in the pressure-induced 90% amorphous material, but are absent in the hydrated zeolite, which instead exhibits the BP found in the glassy state. The arrows indicate the fundamental transverse (t) and longitudinal (l) normal mode frequencies vt/L and vl/L for the secondary building units of zeolite Y (α-cage, β-cage, D6R), where L is the circumference of the internal rings (20-fold, 12-fold, and 8-fold) and v_t and v_l are 3358 and 5181 m/s, respectively (76).

In a very recent work on Zirconium-based metallic glasses, Ahmad (77) points out a universal correlation between the boson peak and atomic pair correlation function g(r). It is found that the boson peak can be decomposed into six characteristic vibratory modes (a Debye's vibratory mode ω_1 and five Einstein's vibratory modes ω_i). Plotting the ratios $\frac{r_1}{r_i}$, between the first peak position r_1 in g(r) (*Figure* ***11*** a) and the next five well-dominant peaks positions r_i, as a function of $\frac{\omega_i}{\omega_1}$, a linear relation is noticeable (*Figure* ***11*** b). It is described by the equation:

$$\omega_i = \frac{r_1}{r_i}\omega_1 \tag{27}$$

and surprisingly reveals that the vibrational frequencies of all the oscillators are strongly correlated with the local atomic packing.

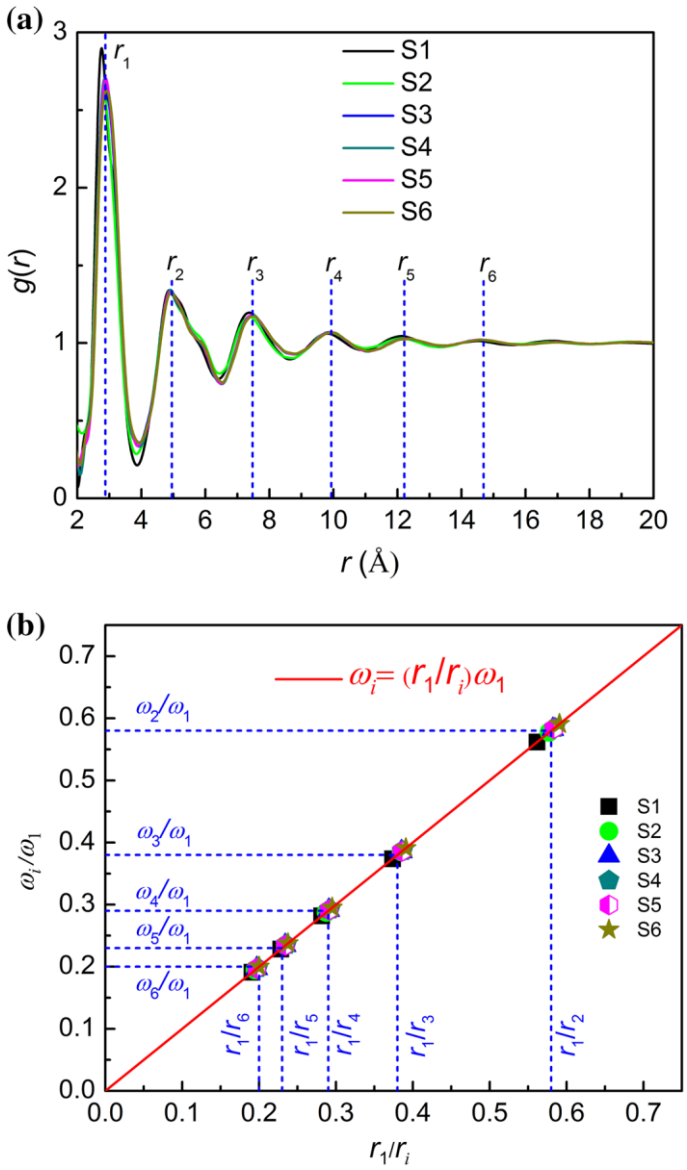

Figure 11. a) Pair correlation function data of the six studied Zr-based metallic glasses obtained from synchrotron radiation-based XRD measurements. b) Plot of $\frac{r_1}{r_i}$ *versus* $\frac{\omega_i}{\omega_1}$ (with i=2,…6). *The red solid line obeys the linear relation* $\omega_i = \frac{r_1}{r_i}\omega_1$, *which is exactly in accordance with Ioffe–Regel condition.*

The above-mentioned relation (27) is in perfect accordance with Ioffe–Regel condition (78), according to which the vibration frequency ω is proportional to 1/d, where d is the diameter of the density fluctuation domains in amorphous solids. Ahmad, therefore, assigns the origin of the boson peak in glasses to the structure of the glasses and in particular to the vibrational contributions of regions with various local density fluctuations, identified by the pair correlation function g(r).

1.3.1 Correlation of FSDP and BP in densified glasses

The truthfulness of a real correlation between structure and dynamics in glasses is often tested by analyzing the behavior of densified systems (74; 79; 15; 67).

Inamura, in his study on densified SiO_2 glass (79), shows that, in addition to the structure factor, also the low energy dynamics is strictly affected by the density. Thus, he points out a relation between structural correlations in the medium range order and low energy vibrational modes: the wavelengths associated to these modes lie indeed in the length scale of the IRO.

The Elliot's model (74), which well explains the structure-dynamics correlation in glasses, even allows the behaviour of the boson peak as a function of density to be understood. Generally, it appears that the maximum frequency ω_m of the boson peak increases with increasing density of the material.

Although some of the frequency shift can be accounted by the concomitant increases in the sound velocity $\bar{v}$ (Equation 23), nevertheless this cause by itself is not completely sufficient. Therefore is reasonable that a corresponding decrease in the correlation length L occurs.

References

1. S.R. Elliott, Nature 354, 445 (1991).

2. A. Bernasconi, et al., Journal of Materials Science 51-19, 8845 (2016).

3. D. L. Price, et al. Journal of Physics C: Solid State Physics 21.32, L1069 (1988).

4. P. S. Salmon, I. Petri, J. Phys.: Condens. Matter 15, S1509 (2003).

5. D. A. Allen, et al., J. Chem. Phys. 94, 5071–5076 (1991).

6. Q. Mei and al., Phys. Rev. B 78, 144204 (2008).

7. S. Susman, et al., Phys. Rev. B, 43, 13, 11076 (1991).

8. S. R. Elliott, Journ. of Phys. Condensed Matter 4, 7661 (1992).

9. Y. Inamura, et al., Phys. Rev. Lett. 93, 015501 (2004).

10. G. D'Angelo, C. Crupi, G. Tripodo and G. Salvato, J. Phys. Chem. B 114, 2467 (2010).

11. K. Tanaka, Philos. Mag. Lett. 57,183 (1988).

12. M. Zanatta, et al., Phys. Rev. Lett. 112, 045501 (2014).

13. M. A. Gonzalez, C. Mondelli, G. D'Angelo, C. Crupi, M. R. Johnson, J.Non-Chryst.Solid 354, 203 (2008).

14. L. Borjessonet al., Phys. Rev. B 39, 3404 (1989)].

15. C. Crupi et al., Phys. Rev. B 92, 134206 (2015).

16. J. Zaug, et al., Nat.Mat.7, 11, 890 (2008).

17. P. H. Gaskell, Journ. Non-cryst. Sol. 351.12, 1003 (2005).

18. A.C. Wright, J. Non-Cryst. Solids, 401, 4 (2014).

19. S. C. Moss, et al., Phys. Disord. Mat. and Adler Eds., 77 (1985).

20. C. Massobrio, A. Pasquarello, R. Car, J. Am. Chem. Soc. 121, 2943 (1999),.

21. U. Hoppe, et al., J. Non-Cryst. Solids 354.29, 3400 (2008).

22. J. K. Christie, S. N. Taraskin, and S. R. Elliott, Phys. Rev. B 70, 134207 (2004).

23. P. S. Salmon et al., Nature (London) 435, 75 (2005).

24. S. R. Elliott, J. Non-Cryst. Solids 182, 40 (1995).

25. M. Nakamura, et al., Phys. Rev. B 67, 064204 (2003).

26. P.H. Gaskell, D. J. Wallis, Phys. Rev. Lett. 76, 66 (1996).

27. L. E. Busse and S. R. Nagel, Phys. Rev. Lett. 47, 1848 (1981).

28. S.R. Elliott, Phys. Rev. Lett. 67, 711 (1991).

29. S. Susman, et al., J. Non-Cryst Solids 106, 26 (1988).

30. C.M. Massobrio and A. Pasquarello, J. Chem. Phys. 114, 7976 (2001).

31. J. Swenson, et al., Phys. Rev. B 52, 9310 (1995).

32. A.C. Wright, et al., Trans. Am. Crystallogr. Assoc. 27, 239. (1991).

33. P. Y. Huang, et al., Nano Lett. 12, 1081 (2012).

34. T. Tohei, I. Tanaka et al., Phys. rev. B, 73, 064304 (2006).

35. P. Debye, Annalen der Physik, 344-14, 789 (1912).

36. J.M. Ziman, Principles of the Theory of Solids, Cambridge University press (1972).

37. P. Richet, D. de Ligny, E. F. Westrum., J. Non-Cryst. Solids, 315, 1-20 (2003).

38. R.C. Zeller, R.O. Pohl, Phys. Rev. B, 4, 2029 (1971).

39. A. Fontana, and al., Phys. Rev. Lett. 78, 1078 (1997).

40. F. Sette et al., Science 280, 1550 (1998).

41. A. I. Chumakov et al., Phys. Rev. Lett. 92, 245508 (2004).

42. A. Monaco et al., Phys. Rev. Lett. 96, 205502 (2006).

43. G. Ruocco et al., Phys. Rev. Lett. 84, 5788 (2000).

44. U. Buchenau, and al., Phys. Rev. B 46, 2798 (1992).

45. T. S. Grigera, and al., Nature London 422, 289 (2003).

46. W. Schirmacher, and al., Phys. Status Solidi C 5, 862 (2008).

47. A.P. Sokolov, et al., Phys.Rev. Lett. 71,13, 2062 (1993).

48. A. Parshin, Sov. Phys. Solid State 36, 991 (1994).

49. L. Orsingher, et al., Journ. of chem. Phys. 132, 12, 124508 (2010).

50. S. Caponi, A. Fontana, et al., Phys. Rev. B, 76, 092201 (2007).

51. G. Baldi, A. Fontana, et al., Phys. Rev. Lett. 102, 195502 (2009).

52. E. Duval, et al., Europhys. Lett. 63, 778 (2003).

53. S. Caponi, et al., Phys. Rev. Lett. 102, 027402 (2009).

54. P. Flubacher, A.J. Leadbetter, et al., J. Phys. Chem. of Solids, 12-1,53 (1959).

55. R. Shuker, R. Gammon, Phys. Rev. Lett., 25-22 (1970).

56. R. Orbach, Philos. Mag. B 65, 289 (1992).

57. U. Buchenau e al., Phys. Rev. Lett. 60, 1318 (1988).

58. P. B. Allen and J. L. Feldman, Phys. Rev. B 48, 12 581 (1993).

59. P. Benassi et al., Phys. Rev. Lett. 77, 3835 (1996).

60. S. R. Elliot, Phys. Amorph. Mater., Longman, NY (1990).

61. Y. G. Vainer et al., Phys. Rev. Lett. 97, 185501 (2006).

62. A. Il'in, et al, Sov. Phys. JEPT 65, 165 (1987).

63. W. Schirmacher, G. Diezemann, C. Ganter, Phys. Rev. Lett. 81, 136 (1998).

64. W. Schirmacher, G. Diezemann, C. Ganter, Phys. B Condensed Matter 263, 160 (1999).

65. G. Roucco, F. Sette, J. Phhys. Condens. Matter, 13 – 41, 9141 (2001).

66. T. Scopigno, et al, J. Phys.Condens. Matter, 15-11, S1269 (2003).

67. C. Crupi, G. Carini, G. Ruello, G. D'Angelo, Phil. Mag. 96, 7, 788 (2016).

68. G. D'Angelo, et al., Phys. Rev. B 79, 014206 (2009).

69. G. Carini Jr., et al., Phys. Rev. Lett. 111, 245502 (2013).

70. L. Börjesson, et al., Phys. Rev. Lett., 70 -9, 1275 (1993).

71. E. Duval, et al., Journ. Phys.Condensed Matter 2-51, 10227 (1990).

72. S. Sugai, A. Onodera, Phys. Rev.Lett. 77-20, 4210 (1996).

73. A. Lukyanov, V. Lubchenko, Journal Chem. Phys., 147-11, 114505 (2017).

74. S. R. Elliott, Europhys. Lett. 19, 201 (1992).

75. A. P. Sokolov et al., Phys. Rev. Lett. 69, 1540 (1992).

76. G. N. Greaves et al., Science 308, 1299 (2005).

77. A. S. Ahmad, et al. J. Low Temp. Phys., 186, 1-2, 172 (2017).

78. A. F. Ioffe, A. B. Begel, Prog. Semicond. 4, 237 (1960).

79. Y. Inamura, et al., Physica B 241-243, 903 (1998).

Chapter 2

THE EFFECT OF PRESSURE ON VIBRATIONS, SPECIFIC HEAT AND STRUCTURE OF DISORDERED SYSTEMS

As already pointed out in the previous chapter, glasses exhibit an excess of low energy vibrational states and an intermediate-range order in their structure.

Until now, no satisfying and complete explanation or a comprehensive theoretical model for all the observed anomalies has been proposed, thus both the IRO and the Boson peak remain a subject of discussions.

Recently, some effective insights have been achieved by studying the changes of vibrational, thermal and structural properties following the in situ-densification or pressurization of glasses.

Many studies have been performed in samples with the same stoichiometry but different densities in order to determine if any phase transition, associated to the BP changes, could take place.

Indeed, in a phase change, the topology of solids can profoundly be modified, because of the variations of coordination numbers and the consequent formation of atomic aggregates. As disordered solids are metastable and non-ergodic systems, the activation energy barriers between different metastable amorphous phases are lower than the energy required to undergo a transition to a stable state. The structural transition can be identified by using suitable experimental techniques of vibrational dynamics (i.e. Raman spectroscopy, inelastic neutron scattering) or structural analysis (i.e. neutron elastic diffraction).

In this chapter, we discuss about the influence of the densification on the Boson Peak and the First sharp diffraction Peak of glasses.

2.1 Pressure dependence of the FSDP

The evolution of FSDP with pressure is commonly investigated by performing X-ray and neutron diffraction measurements (1; 2; 3).

Many experimental results show that the increase of the density of glasses induces a shift in the position of the FSDP towards higher Q values and a decrease of its intensity (4), unlike the other peak in S(Q). This behavior is noticeable in many glasses, such as chalcogenide (5) and silica (6; 7).

The pressure dependence of the FSDP intensity $(\partial I/\partial p)_T$ can be expressed by the equation:

$$\left(\frac{\partial I}{\partial p}\right)_T = \left(\frac{\rho}{B}\right)\left(\frac{\partial I}{\partial \rho}\right)_T \quad (1)$$

where B is the bulk modulus.

The rapid decrease of the FSDP intensity with increasing pressure is attributed to the negative value of the factor $(\partial I/\partial \rho)_T$ (8).

A neutron scattering study by Inamura (9) on v-SiO_2 has allowed to observe the detailed evolution of the intermediate range structure as a function of densification. It showed that the tetrahedral structure of silica glasses over the short range is scarcely affected by the density increase. On the other hand, the FSDP is strongly influenced by the densification, exhibiting some modifications in the IRO domain. The densification determines the filling of the open glassy network, generating a strong reduction of the voids size.

This interpretation is supported by MD calculations of Rino and co-workers. They suggest that the major structural changes revealed in the S(Q), caused by the applied hydrostatic pressure, are attributable to the distortion of the tetrahedral packing, which rearranges, shrinking the volume of the inter-tetrahedral rings (10). Moreover, if the density is increased above a critical value, a modification of the coordination number occurs, marking the transition from fourfold to six-fold coordinated structure. These results are in agreement with Elliot's void model.

In other studies of computer simulations by Iyetomi on densified chalcogenides $GeSe_2$ (8), the shift in position of the FSDP to higher values of Q with increasing pressure has been also explained on the basis of the model proposed by Elliot (4): the FSDP is interpreted as a pre-peak in the concentration-concentration partial structure factor due to the chemical short-range ordering of interstitial voids around cation-centred clusters in the glassy structure. On the basis of these outcomes, the void structure can be considered the analogous of the inner space of the six-fold ring, becoming responsible for the intermediate range structure.

A recent study analyzed and compared the medium-range structure of a series of densified glassy systems (GeO_2, SiO_2, $GeSe_2$, Li_2O-$2SiO_2$, LDA, HDA) (11), concluding that the IRO arises from the periodicity of boundaries of nanovoids homogeneously distributed in the network. Furthermore, the changes in the FSDP intensity and position with the densification were found to reflect the variations in the distribution of void

sizes and shapes. In this approach, the Q position of the FSDP (Q_{FSDP}) provides a direct indication of the void diameter d as

$$Q_{FSDP} = 2\pi/d \quad (2)$$

2.2 Pressure dependence of the BP

The previous paragraph was focused on the influence of the densification effects on the structure of vitreous systems. In this section, the changes of the vibrational dynamics generated in glasses by changes of the density will be described.

The evolution of BP as a function of pressure or densification have been experimentally investigated by performing measurements of specific heat (12), Raman (13; 14), and inelastic neutron scattering (15). All these techniques have shown that the increase of the density induces a shift of the BP towards higher frequencies and a simultaneous decrease of its intensity (13; 16; 17), as it is possible to observe in Figure 7 of Chapter 1.

Furthermore, in both theoretical and experimental studies the BP intensity changes are closely related to its frequency shift (18).

Despite the consistency of the experimental results, there is still no general interpretation that sheds light on the nature (acoustic, optical, localized or delocalized) of these low energy modes. Several plausible explanations have been proposed to explain the cause of the BP modifications.

The most commonly used assumption considers the glass as an elastic medium, that supports a constant contribution of excess energy modes, and justifies the observed pressure-induced variations of the boson peak as due to the evolution of the elastic medium with density (19; 20; 21). This method

provided discordant outcomes. It properly describes the transformations of the vibrational density of states VDOS with pressure in some systems, such as silicate glasses, where, in the absence of local structural transformations, the Debye level and the glass-specific excess of vibrational states above it have the same dependence on density (21). Conversely, it does not fully account the changes with density of other systems like germania glass (22) or polymeric materials (23).

Deschamps, instead, associates the low frequency anomalies in silica to the peculiar structures existing in the amorphous phase (13).

Another approach attributes the decrease of the Boson peak intensity with the densification to the void space reduction within the three-dimensional network, which induces the suppression of the excess modes (24).

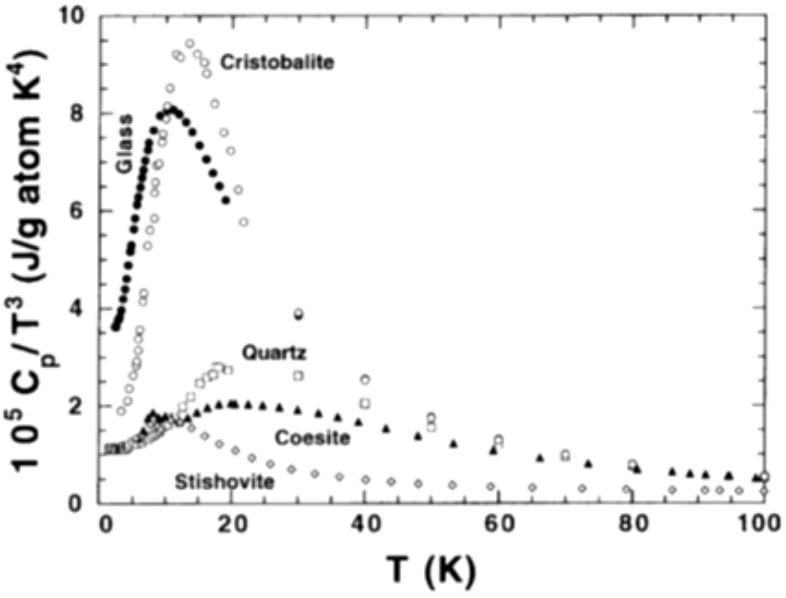

Figure 1. The Boson peak of SiO_2 glass and polymorphs, revealed by deviations of the heat capacities from Debye's T^3 law.

In Figure 1, the specific heat plotted as C_p/T^3 is showed for both SiO_2 glass and some crystalline polymorphs. This plot reveals the deviation of the specific heat from Debye's T^3 law: the excess C_p strongly increases when the density decreases, becoming greater for the less dense polymorph cristobalite than for SiO_2 glass; conversely, no Boson peak is observed for the dense tetragonal SiO_2 (stishovite).

Moreover, a comparison between the thermal and vibrational properties of ambient silica glass (ρ= 2200 Kg/m^3) and α-quartz (ρ= 2650 Kg/m^3) **(25)** is shown in Figure 2: the density of vibrational states vDOS in the glass is softer than in crystal (Figure 2 a); the reduced glassy vDOS ($g(\omega)/\omega^2$) exhibits a peak in the frequency region where the crystal has a flat trend (Figure 2 b) and the glassy specific heat shows an excess over that of the crystal (Figure 2 c). These anomalies are usually attributed to disorder.

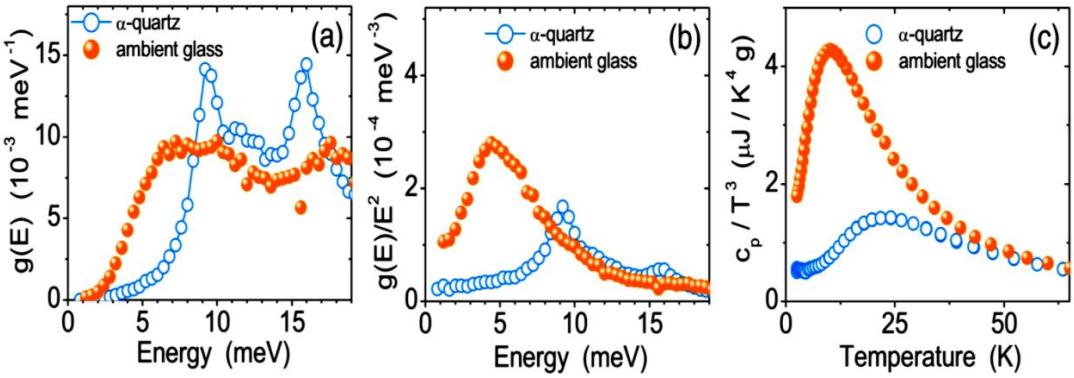

Figure 2. Comparison between a) the density of vibrational states, b) the reduced density of vibrational states and c) the specific heat of a low-density silica glass (ρ= 2200 Kg/m^3) and a high density crystal of α-quartz (ρ= 2650 Kg/m^3). The solid and open circles refers to the NRAIXS and IXS data, respectively (25).

A different interpretation of vibrational anomalies of glasses has been proposed by Chumakov (25), who suggested to compare glasses and crystals with the same density, in order to put in evidence the effect of disorder.

The specific heat and the vibrational density of states of ambient-pressure silica glass and α-cristobalite having similar densities (2200 and 2290 Kg/m^3 respectively) are shown in Figure 3. The two samples show a strictly similar behavior of the DOS, except for the smearing out observed in the glass (Figure 3 a); the peaks of reduced DOS are located at almost the same energies (Figure 3 b) and the specific heats are almost identical (Figure 3 c)).

Consequently, Chumakov associated the observed anomalies to the differences in the density rather than to disorder.

Moreover, since the peak in the reduced DOS of the crystal is generated by an acoustic van Hove singularity, it has been proposed that also the Boson peak of silica has the same origin.

In this perspective, the above-mentioned hypothesis should be correct for all vitreous systems, because glasses are always less dense than the crystalline counterparts. The same behavior of glassy SiO_2 and its crystalline polymorphs has been observed in zeolites (26).

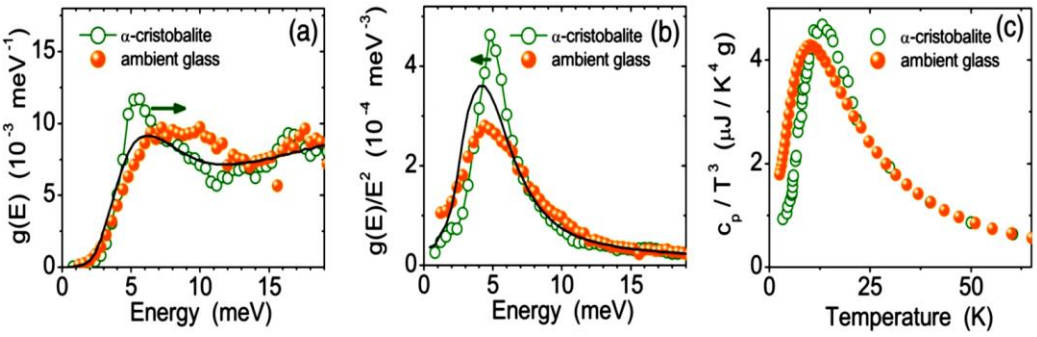

Figure 3. Comparison of a) the density of vibrational states, b) the reduced DOS and c) the specific heat of ambient silica glass (ρ= 2200 Kg/m^3) and α-cristobalite (ρ= 2290 Kg/m^3). The solid and open circles refers to the NRAIXS and IXS data respectively. The arrows emphasize the shift of the peaks in glasses, relative to humps in crystal. The solid lines represents theoretical curves evaluated by considering the finite size of Brillouin zone **(25)**.

References

1. S. Susman et al., Phys. Rev. B, 43, 13, 11076 (1991).

2. Q. Mei, et al., Phys.Rev. B 74, 1- 014203 (2006).

3. J. Zaug, et al., Nat.Mat.7, 11, 890 (2008).

4. S. R. Elliott, Journ. of Phys. Condensed Matter 4, 7661 (1992).

5. K. Tanaka, Philos. Mag. Lett. 57,183 (1988).

6. C.J. Benmore et al., Phys. Rev. B, 81, 5, 054105 (2010).

7. Y. Inamura et al., Phys. Rev. Lett. 93, 015501 (2004).

8. H. Iyetomi, et al., Phys Rev. B 43, 1726 (1991).

9. Y. Inamura, et al., Physica B, 284,1157 (2000).

10. J. P. Rino, I. Ebbsjo, R. K. Kalia, et al. Phys. Rev. B 47, 3053 (1993).

11. C. Crupi, et al., Phys. Rev. B 92, 134206 (2015).

12. J.D. Boyer, et al., J. Non-Cryst. Solids 55, 413 (1983).

13. T. Deschamps et al., Journ. of Non-Cryst. Solids, 355-48, 2422 (2009).

14. S.Sugai, A.Onodera, Phys. Rev. Lett. 77, 4210 (1996).

15. Y. Inamura, et al., J. Non-Cryst. Solids 293, 389 (2001).

16. L. Hong, et al., Phys. Rev. B, 78,134201 (2008).

17. M. Zanatta, et al.,Phys. Rev. Lett. 112, 045501 (2014).

18. T.S. Grigera, V. Martin-Mayor, G. Parisi, P. Verrocchio, Nature, 422, 289 (2003).

19. M. Zanatta, Diss. University of Trento (2011).

20. G. Baldi, A. Fontana, et al., Phys. Rev. Lett., 102, 195502 (2009).

21. A. Monaco, A. I. Chumakov, et al., Phys. Rev. Lett., 97,135501 (2006).

22. L. Orsingher, et al., J. Chem. Phys., 132, 124508 (2010).

23. L. Hong, et al., Phys. Rev. B, 78,134201 (2008).

24. Y. Inamura, and al., J. Non-Cryst. Sol., 293, 389 (2001).

25. A. I. Chumakov, et al. Phys. Rev. Lett., 112-2, 025502 (2014).

26. G.N. Greaves et al., Science, 308, 5726-1299 (2005).

Chapter 3

SAMPLE DETAILS

3.1 Structure of borate glasses

B_2O_3 is an archetypal network glass-forming material, widely used as industrial material. For example, it is a component of Pyrex, a boroaluminosilicate that has widespread laboratory and household use.

Despite the numerous studies about the structure of vitreous B_2O_3, the exact nature of its atomic arrangement has remained a matter of some disputes.

Indeed, while B and O atoms are known to be respectively in threefold and twofold coordination, it is not clear exactly what configuration of the basic molecular unit is involved in the atomic network.

The most accredited hypothesis considers the structure of B_2O_3 glasses made of the symmetrical planar B_3O_6 boroxol rings (Figure 1), the superstructural units formed by three BO_3 planar triangle (Figure 2) (1), which are corner-linked by sharing common O atoms.

This assumption can be deduced from the observation of an extremely intense, narrow and highly polarized peak in Raman spectra at 808 cm^{-1} (2). Indeed, the position of this band is un-shifted also with a $^{10}B \rightarrow ^{11}B$ isotopic substitution (2), implying that it is associated with modes which involve little or no motion of the boron atoms. Moreover, further Raman studies, in which the $^{16}O \rightarrow ^{18}O$ substitution was executed in addition to boron isotopic substitution, let to conclude that the sharp 808 cm^{-1} line is generated by the localized breathing mode of the oxygen atoms in boroxol ring (3). The sharpness of the line is associated with a localized motion to a single ring and to a restricted distribution of angles in the rings.

A further signature of the structure is the broad 470 cm^{-1} line, that is also un-shifted after boron isotopic substitution, and is related to in-phase motion of the bridging oxygens (Figure 3). Its breadth is ascribed to an extended motion and to a large distribution of bridging oxygen B-O-B angles outside the ring.

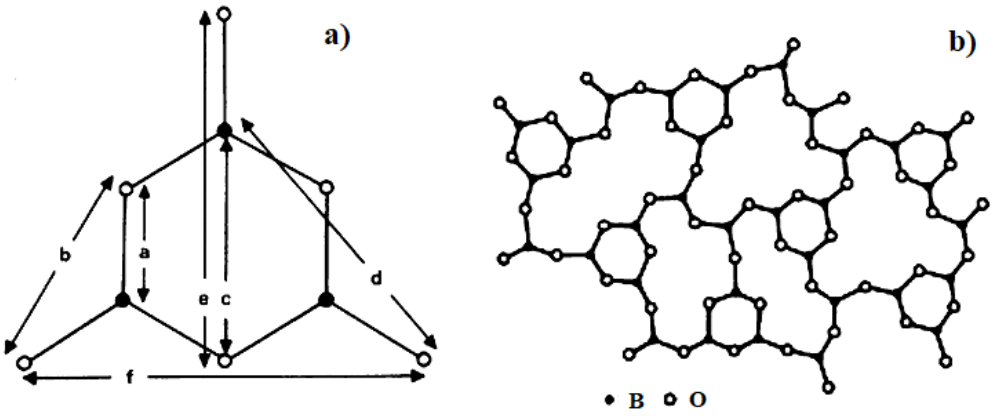

Figure 1. a) B_3O_6 boroxol ring with its characteristic interatomic separations (a=1.37 Å; b=2.37 Å; c=2.74 Å; d=3.62 Å; e=4.11 Å and f=4.75 Å) (4) *and b) symbolic model of glassy B_2O_3, where some boroxol rings are formed.*

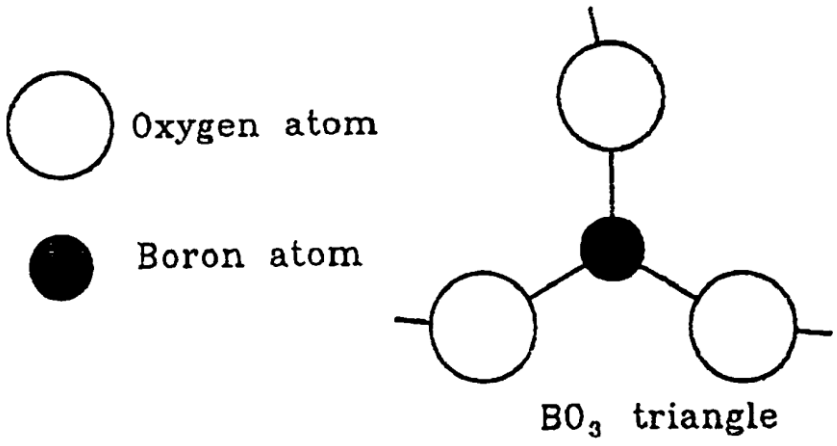

Figure 2. The BO_3 triangle basic structural unit used to describe the v-B2O3 network.

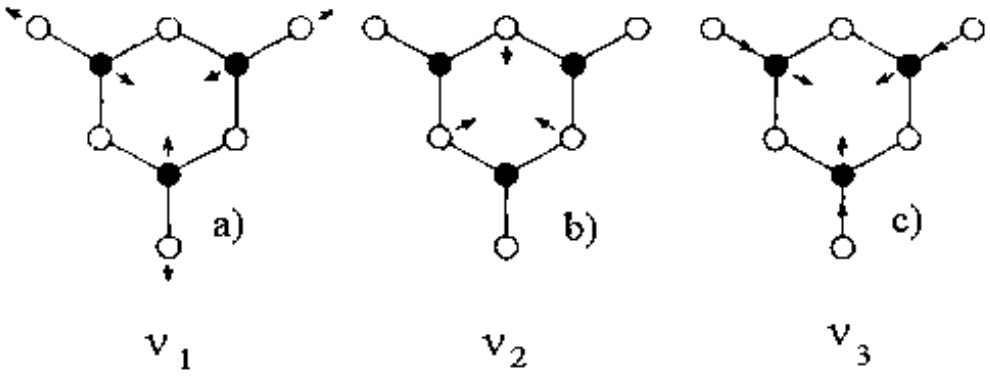

Figure 3. Three symmetrical vibrations of the boroxol ring: a) symmetric B-O stretching; b) trigonal deformation of the ring; c) ring breathing (B-O atoms in phase) **(5)**.

3.2 Structure of alkaline borate glasses

We term alkaline borate glasses with $(M_2O)_x$ $(B_2O_3)_{1-x}$, where x represents the molar fraction and M^+ is an alkaline ion.

The addition of alkali oxide to B_2O_3 determines substantial changes in the structure. According to the structural model proposed by Krogh-Moe (6), the network of alkaline glasses is built up by various structural units (boroxol, tetraborate, diborate groups), that also appear similar in the corresponding crystalline compounds.

Raman spectroscopic studies on alkali borate glasses reveal the possibility of two competitive chemical processes promoted by the dispersion of alkali ions in the glassy structure.

The first process, occurring at low concentrations of M_2O, leads to the transformation of threefold-coordinated borons into fourfold-coordinated ones, with the positive alkali ion M^+ adjacent to the negative BO_4^- units in order to preserve the local charge neutrality (Figure 4 a). Conversely, the second process leads the formation of a non-bridging oxygen O^- (NBO) adjacent to the positive alkali ion (Figure 4 b).

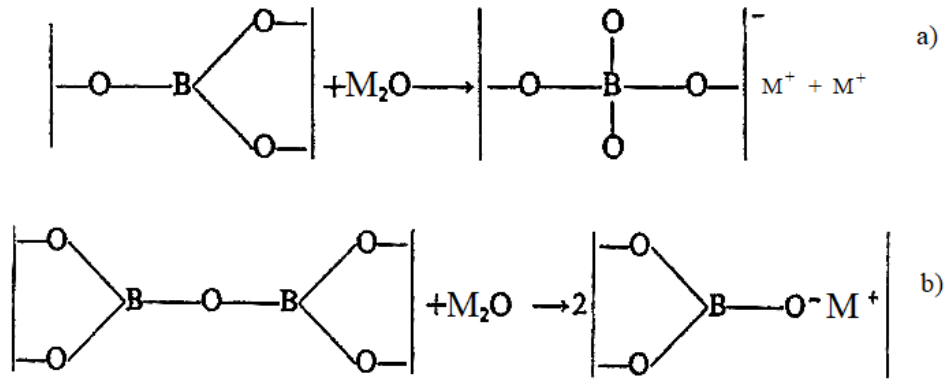

Figure 4. Two chemical processes by means the alkali ions can be dispersed in the glassy structure: a) boron in fourfold coordination, with the positive alkali ion M^+ adjacent to the negative BO_4^- units; b) non-bridging oxygen O^- adjacent to the positive alkali ion.

Nuclear magnetic resonance (NMR) (7), Raman (5; 8; 9), and infrared (10) experiments show differences in the fraction N_4 of 4-coordinated borons for the different alkali borate systems (Figure 5). The dependence of N_4 on the specific alkali ion presumably arises from a competition between the two processes.

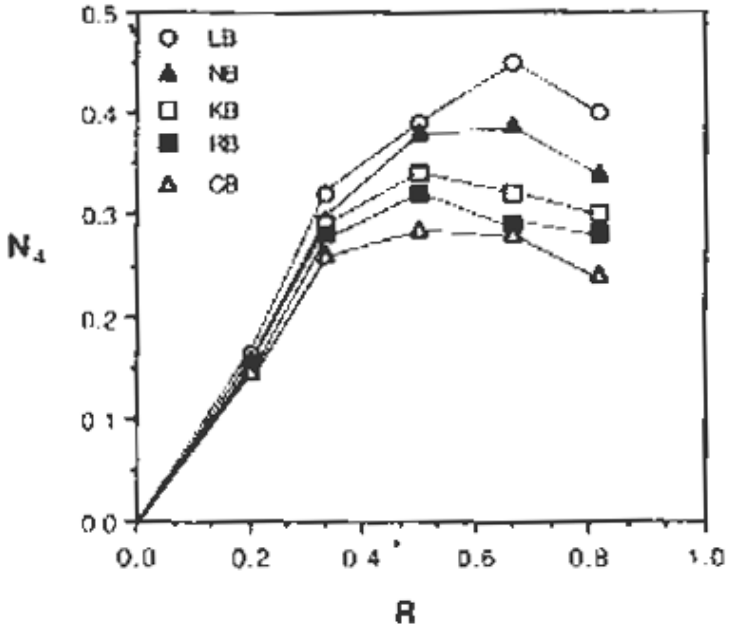

Figure 5. *: N_4 as a function of R (R=x/1-x) for alkali borate glasses, being LB, NB, KB, RB, CB the lithium, sodium, potassium, rubidium, cesium borate, respectively* **(7)**.

It is expected that the negative Coulomb potential energy of the $BO\text{-}M^+$ configuration decreases in magnitude as the alkali ion size increases.

However, the separation between the ionic charge M^+ and the O^- should be less than the separation of the M^+ from the effective center of the distributed negative charge on the BO_4^-, and the deeper potential well for the $O^-\text{-}M^+$ configuration would favor the formation of the NBOs.

By indicating with N_3 and N_4 the fraction of three-coordinated and four-coordinated borons, respectively, it shall be verified that $N_3+N_4=1$.

Therefore, the formation of NBO, which indicates the increase in the number of N_3, implies a simultaneous decrease of N_4.

In Raman spectra, the evidence for such a process is provided by the appearance of a band around 775 cm^{-1} and by the simultaneous decrease in the intensity of the 808 cm^{-1} band, which suggested a gradual conversion of the borate structure into rings containing units with four bridging oxygen (9).

The shift of the maximum position to lower R-values (with R=x/1-x), as the alkali ion size increases, indicates a more favorable formation of NBO compared with BO_4 units (Figure 5).

In particular, the borate units expected to exist in alkali borate glasses (11) (Figure 6) at different compositional ranges are:

- 0-20% mol of M_2O: boroxol, tetraborate, loose BO_3 triangles and loose BO_4 tetrahedra;
- 20-35% mol of M_2O: tetraborate, diborate, loose BO_3 triangles and "loose" BO_4 tetrahedra;
- 35-50% mol of M_2O: diborate, metaborate, pyroborate, orthoborate and "loose" BO_3 triangles.

Furthermore, in the range $0<x<0.3$, the average size of borate groups increases with the increasing size of the alkali ions: triborate groups containing one six-member ring are dominant in the lithium borate glasses, while tetraborate groups that contain three linked six-member rings are dominant in the caesium borate glass (12).

Many structural differences of alkali borate have been pointed out also by neutron diffraction measurements (13). The boron-oxygen network of glasses with different cation modifiers is very similar on the short-range order, involving nearest neighbor and next nearest neighbor distances. The change of boron atoms coordination from 3 to 4 is evident from the splitting of the first B-O distances with increasing modifier content. However, the most

significant differences between different modified glasses are observed in the intermediate range, involving the relative arrangement of the various molecular borate groups. The cations coordinate to oxygen and form bridges between neighbouring B-O chain segments: change of the coordination numbers and cation-oxygen interatomic distances produce different number densities as well as intermediate correlations.

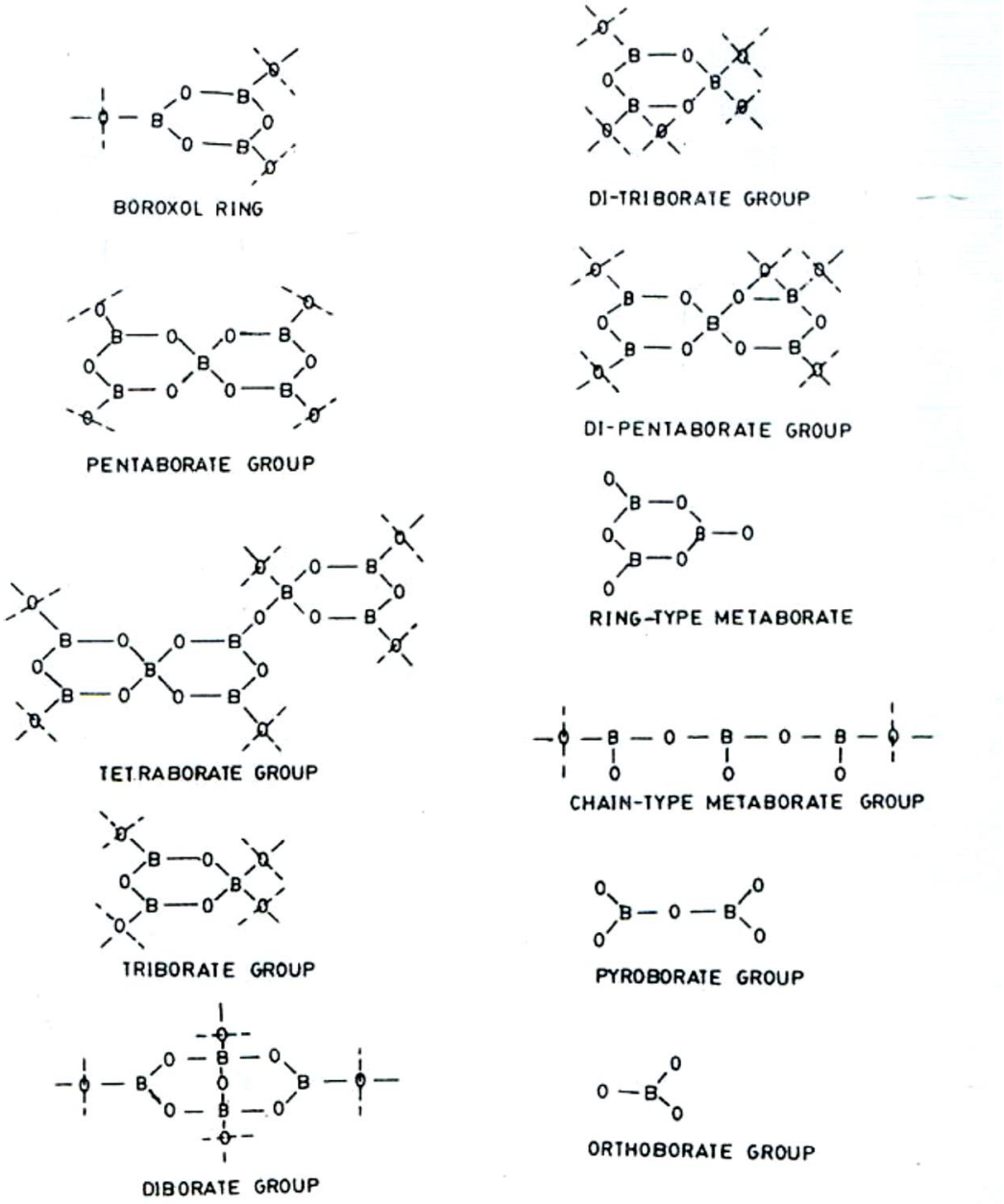

Figure 6. The *structural groups present in several alkaline borate glasses* **(11)**

3.3 Structure of α-quartz

Being the second most abundant mineral in the earth's crust (about 12% of its volume), the quartz (SiO_2) is stable under a broad range of conditions including pressure, temperature, fluids presence, deformations.

Its abundance is reflected in the presence in many rocks and in a very large variety of crystal structures.

A great interest in this material arises also from its technological applications. Importantly, it is used in the field of optic fibers technology.

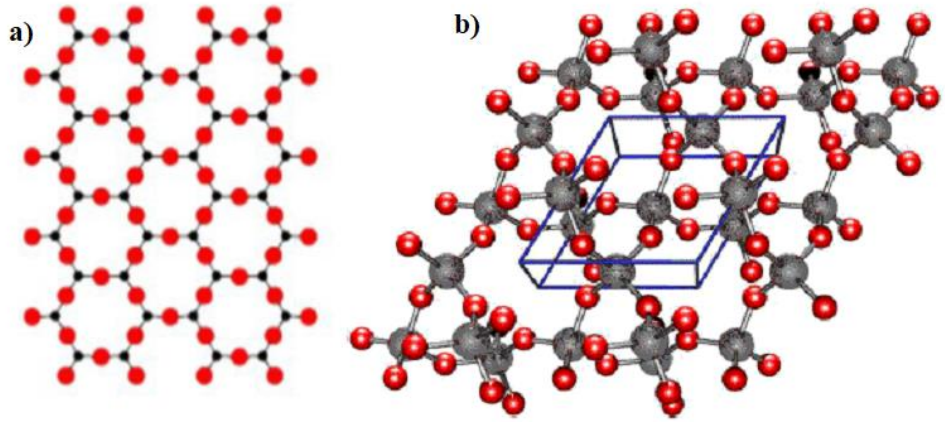

Figure 7. a) Bidimensional and b) tridimenional structure of crystalline α-quartz. Red dots are oxygen atoms while black dots refer to silicon ones **(14)**.

The α-quartz has a trigonal structure characterized by silicon-oxygen tetrahedra (14), which share four vertices to form right or left spirals (*Figure 7*). Particularly, in a crystal these are all right-handed or all left-handed.

Its habitus consists of a hexagonal prism having, in the corners, the faces of two rhombohedra arranged to simulate a hexagonal bipyramid (15) (*Figure 8*).

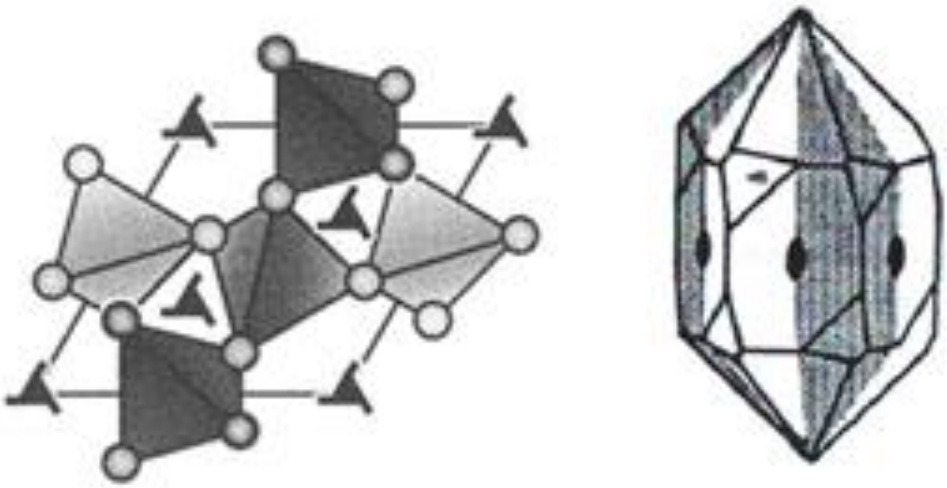

Figure 8. Trigonal structure and habitus of α-quartz. In some crystals, the right or left crystalline parts coexist to form geminates.

Two slightly different Si-O distances (1.597 and 1.617 Å) and a characteristic Si-O-Si angle equal to 144° are identified in α-quartz structure. An analysis of different silicates shows that this angle generally varies in the 125-160 ° range.

Modest differences exist between α and β forms of quartz: just a small relative rotation of the tetrahedrons, which does not change the connection way between the units. Therefore, the conversion to α → β does not require the breaking of Si-O-Si bonds, but only a small distortion of the structure and it is therefore an easy and reversible process.

3.4 Samples preparation

3.4.1 Alkaline borate glasses

Alkaline borate glasses $(M_2O)_x$ $(B_2O_3)_{1-x}$, where M= Li^+, Na^+, K^+, Cs^+, with different molar fractions x, have been used for neutron diffraction measurements.

The glasses have been prepared from laboratory reagents with 99.99% of purity grades of the specific alkaline nitrate and boron oxide with a stated ^{11}B enrichment of 99% in order to minimize the influence of the high neutron absorption of the ^{10}B present in natural boron.

The appropriated amounts of powders were mixed to obtain the desired concentrations and melted in a crucible within an electric furnace by heating to 1373 K at a rate of 1 K/s in inert atmosphere. The mixture was kept at this temperature for more than 6 h and occasionally stirred to ensure homogeneity of the liquid. Then the melt was cooled spreading it on a rigid support to obtain a circular slab with a diameter of about 5 cm and a thickness of 0.2 mm. Afterwards, each glass was annealed and stabilized at about 20 K above its calorimetric glass transition temperature in a high-purity nitrogen atmosphere and then cooled to room temperature. Finally, all samples were stored in a vacuum-sealed desiccator to avoid unwanted reaction with moisture.

3.4.2 Densified borate glasses

Densified borate glasses have been investigated by means elastic and inelastic neutron scattering, Raman experiment and measurements of low temperature specific heat.

The densification was obtained with a high temperature-high pressure multianvil apparatus, schematically depicted in Figure 9 (16). The samples

were fused under pressure at 1160 °C (2-GPa glass) and at 1060 °C (4-GPa/B3 glass) for about 20 min and then quenched at those pressures.

Conversely, the sample 4-GPa/B4 glass was obtained by quenching from 1200 °C melts of ^{11}B2O3 under a pressure of 4 GPa.

Thus, the densified B_2O_3 glasses were characterized by X-ray diffraction, which revealed no sign of crystallization.

Crystalline sample (c-B_2O_3) was obtained by fusing $^{11}B_2O_3$ glasses at 1280 °C under a pressure of 4 GPa for about 15 min and then by pressure-quenching it to room temperature. The X-ray diffraction pattern of polycrystalline sample gave well-defined peaks, typical of trigonal crystalline B_2O_3 (α-B_2O_3) (17).

It is worth noting that 4-GPa/B4 sample is structurally different from that also synthesized at 4 GPa, but pressure quenched from lower temperatures (4-GPa/B3). Indeed, 4-GPa/B4 reveals variation of the chemical bonding in the network with the formation of fourfold-coordinated boron atoms which gives rise to a higher density (at room temperature, ρ=2373 kg/m^3 for 4-GPa/B4 glass and ρ=2174 kg/m^3 for 4-GPa/B3 glass).

A very suitable parameter to account for variations in the microscopic structure of a glass is the atomic packing fraction ϕ, which is defined by the ratio between the ionic volume V_{atomic} and the molar volume V_{molar}:

$$\phi = \frac{N_A V_{atomic}}{V_{molar}} \qquad (1)$$

N_A being the Avogadro number. The theoretical ionic volume is given by

$$V_{atomic} = \sum \frac{4}{3} \pi r_i^3 X_i \,, \qquad (2)$$

r_i and X_i being the radius and the fraction of the ith atom in the formula unit, respectively.

The ionic radii are taken from data by Shannon (18), accounting for the coordination of network-forming ions.

The atomic packing fraction of 4-GPa/B4 glass is ϕ=0.457, to be compared with ϕ=0.419 of 4-GPa/B3 glass.

The mass densities ρ and molecular number densities ρ_N measured at room temperature, the Debye sound velocity v_D and the elastic Debye temperature Θ_D of the investigated samples are shown in

Table ***1***.

The Debye temperature values v_D have been determined by means the longitudinal (v_L) and trasversal (v_T) sound velocities:

$$\frac{3}{v_D^{\,3}} = \frac{1}{v_L^{\,3}} + \frac{2}{v_T^{\,3}} \qquad \textbf{(3)}$$

The velocities v_L and v_T are measured on the samples at 8 K, by using the pulse-echo-overlap (PEO) method proposed by Papadakis (19) on the basis of the superposition method due to McSkimin (20).

Samples	ρ (Kg/m^3)	ρ_N (mol/Å^3)	v_L (m/s)	V_T (m/s)	v_D (m/s)	Θ_D (K)
v-B2O3	1826	0.07898	3242	1830	2035	260.3
2GPa	2082	0.09006	3737	2141	2378	317.7
4GPa/B3	2174	0.09404	5287	3021	3357	454.9
4GPa/B4	2373	0.10265	6393	3653	4059	576
c-B2O3	2550	0.11030	8344	4069	4571	

Table 1. Mass densities ρ and molecular number density ρ_N measured at room temperature, longitudinal v_L, transversal v_T and Debye sound velocity v_D, elastic Debye temperature Θ_D of B_2O_3 densified glasses.

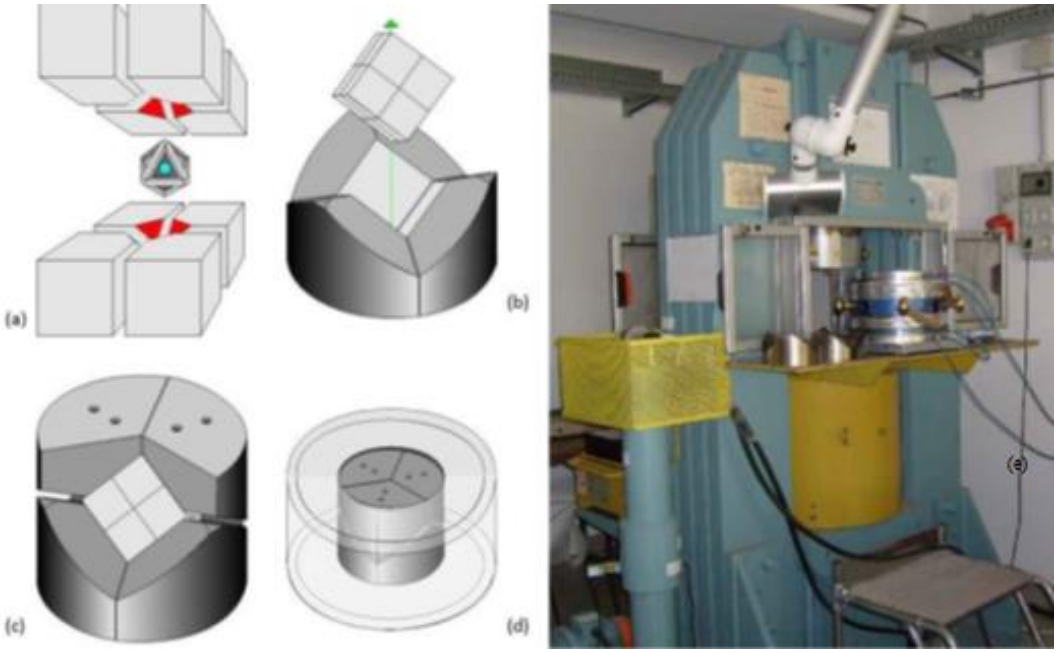

Figure 9. Schematic representation of the multi anvil apparatus. The samples are loaded into holes drilled in a ceramic MgO_2 octahedral cell. The faces of the octahedron seat against the truncated corners of a series of eight tungsten carbide anvils (a). The resulting cube is perfectly arranged in two sets of three wedges (up and down), which act upon the faces of the cubic assembly (b-c). These two sets of wedges are placed between the upper and the lower plates of a large press (d). During pressurization, the pressure medium squeezes out into the spaces between the anvils until the friction between the octahedron and the anvils balances the pressure generated inside the sample assembly. This set-up ensures that the pressure linearly applied by the press can be efficiently converted into a hydrostatic compression of the sample. The high temperatures are obtained by using an internal resistance furnace (graphite or $LaCrO_3$). Temperature measurements have been performed by an iron-constantan thermocouple. e) picture of the multi-anvil apparatus.

3.4.2 The α-quartz

A sample of α-quartz has been used for in situ-high pressure Raman scattering measurements. The investigated sample was a round 20 μm chip and a three-screw diamond anvil cell (DAC) has been used to apply pressure in the range 0-26 GPa. The working principle and the technical features of the DAC are widely discussed in the next chapter.

References

1. A. C. Hannon et al., J. Non-Cryst. Solids 177, 299 (1994).

2. F. L. Galeener and A. E. Geissberger, J. Phys. Paris Coll. C9, 343 (1982).

3. 6. W. M. Risen Jr., J. Non-Cryst Solids 76, 97 (1985).

4. R. J. Bell and A. Carnevale, Phil. Mag. B 43, 389 (1981).

5. Y. Iwadate, K. Igarashi, et al., J. Chem. Phys. 99 -9,6890 (1993).

6. J. Krogh-Moe, Phys. Chem. Glasses 6, 46 (1965).

7. J. Zhong and P. J. Bray, J. Non-Cryst. Solids 111, 67 (1989).

8. B. N. Meera and J. Ramakrishna, J. Non-Cryst. Solids 159, 1 (1993).

9. E. I. Kamitsos, M. A. Karakassides, G. D. Chryssikos, Phys. Chem. Glasses, 91-5, 1073 (1987).

10. E. I. Kamitsos et al., J. Non-Cryst. Solids 126, 52 (1990).

11. W. L. Konijnendik, Philips Res. Rep. Suppl. 1, 1 (1975).

12. J. Lorosch et al., J. Non-Cryst. Solids 69, 1 (1984).

13. J. Swenson, L. Boriesson, and W. S. Howells, Phys. Rev. B 52, 9310 (1995).

14. W. H. Zachariasen, J. Am. chem. Soc. 54, 3841 (1932) .

15. W.Steurer, Surface Science, 601,18-4407 (2007).

16. G. Carini Jr., G. Carini, G. D'Angelo et al., Phys. Rev. Lett. 111, 24, 245502 (2013).

17. G. E. Gurr. Et al., Acta Crystallogr. Sect. B 26, 906 (1970).

18. R.D. Shannon, Acta Crystallogr. Sect. A 32, 751 (1976).

19. E.P. Papadakis, J Acoust Soc Am, 40-4, 863, (1966).

20. H.J. McSkimin. J Acoust Soc Am, 33-1, 12 (1961).

Chapter 4

EXPERIMENTAL TECHNIQUES

4.1 Neutron scattering measurements

Neutron scattering is a very powerful tool for studying both the structural and dynamic properties of materials. The de Broglie wavelength of thermal neutrons is comparable to the interatomic distances and thus neutrons, with energies appropriate for the experiments, can be used for diffraction.

Thanks to the absence of net electrical charge, neutrons can penetrate deeply into the materials; therefore, unlike X-rays which are scattered by the electron clouds surrounding the atoms, neutrons interact with atomic nuclei and are scattered via the strong nuclear force.

Thus, the neutron scattering cross-sections are not related to the atomic number, so that also the lightest elements can be investigated and the different isotopes of a material can have vastly different scattering lengths.

The interaction between neutrons and matter is weak and the system properties are not excessively altered. Thus, it may be treated by using first-order perturbation theory of the Born approximation, which assumes the incident and scattered neutrons behave respectively like plane and spherical

waves (small perturbation regime). It simplifies the expressions for the scattering cross-sections and, importantly, theory and experiments can be compared in a relatively straightforward way.

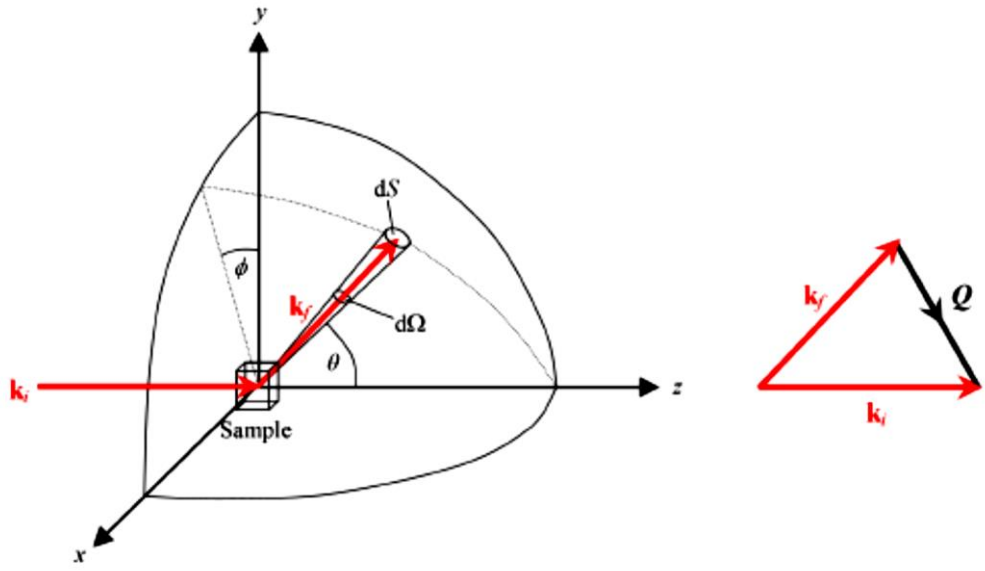

Figure 1. The geometry of a scattering experiment and the scattering triangle. The incident neutrons with wavevector $\boldsymbol{k_i}$ *are scattered by the sample in the direction* θ, ϕ *with the final wavevector* $\boldsymbol{k_f}$*. Q is the scattering vector.*

In a neutron scattering experiment, the incident probes with energy E_i and wave number k_i are scattered by the sample into an element of solid angle $d\Omega$, in direction given by $\mathbf{k_f}$ and with an energy between E_f and $E_f + dE_f$ (*Figure 1*).

If $k_i = k_f$ the process is called elastic. This condition allows to probe the structure of matter.

The scattering vector **Q** is given by

$$\mathbf{Q} = \mathbf{k_i} - \mathbf{k_f} \tag{1}$$

and the momentum transfer is $\hbar\,\mathbf{Q}$.

Conversely, if $k_i \neq k_f$, momentum is not conserved and the process is called inelastic. This condition allows to investigate the dynamic phenomena and the excitations.

The number of neutrons scattered per second in all directions divided by the incident neutron flux Φ is defined the total differential cross-section σ_{tot}.

However, only a fraction of the solid angle during an experiment will be covered by the detectors and the number of neutrons scattered per second into a small solid angle dΩ in the direction θ, ϕ, divided by the incident neutron flux Φ, will be given by the partial differential cross-section $\frac{d\sigma}{d\Omega}$.

The incident neutrons, modelled as plane waves ($\phi_i = e^{ikr}$), hit a single atom providing a weak perturbation, such that the scattered wave becomes spherically symmetric ($\phi_f = -be^{ikr}/r$), r being the radius of the scattered wave and its amplitude being the scattering length b.

The scattering length b is related to the total scattering cross-section σ_{tot} and usually determined from experiments:

$$\sigma_{tot} = \frac{\text{scattered flux}}{\text{incident flux}} = 4\pi b^2 \tag{2}$$

It depends on the atom, the isotope and the relative orientation of the nuclear and neutron magnetic moments. Therefore, even if the scattering is coming from a single element, there will not be a single scattering length in the

sample, but a distribution of lengths. It implies that the scattered neutrons will have different phases, giving rise to two terms in the total scattering cross-section:

- a coherent term arising from an average scattering length of the system, $\sigma_{\text{coh}} = 4\pi\bar{b}^2$;
- an incoherent term, coming from the variation of the scattering lengths, $\sigma_{\text{incoh}} = 4\pi\left(\overline{b^2} - \bar{b}^2\right)$.

During a powder diffraction experiment, the recorded pattern will be the sum of the coherent scattering, seen as Bragg peaks, and a non-zero incoherent background. The structural information arising from the Bragg scattering due to an array of nuclei, n, is given by the differential cross-section, defined as:

$$\frac{d\sigma}{d\Omega} = \left|\sum_n b_n \exp(iQ \cdot r_n)\right|^2 \tag{3}$$

where $r = xa + yb + zc$ gives the position of the interacting nucleus in terms of the lattice parameters.

Diffraction occurs when Bragg's law is satisfied, i.e.

$$\mathbf{Q} = 2|\mathbf{k}|\sin\theta \tag{4}$$

Thus, nuclear scattering peaks will appear when the scattering vector is equal to a reciprocal lattice vector and $\frac{d\sigma}{d\Omega}$ is defined as

$$\frac{d\sigma}{d\Omega} = N^2 \left|F(hkl)\right|^2 \tag{5}$$

where N is the number of unit cells, and the structure factor F(hkl) is given by

$$F(hkl) = \sum_n b_n \exp\left[2\pi i(hx_n + ky_n + lz_n)\right] \tag{6}$$

The intensity of the Bragg scattering will be proportional to $\left|F(hkl)\right|^2$.

4.1.1 Instruments to determine the structure: elastic scattering and the diffractometers D1 and D4

Reactor diffractometers are instruments that allow to obtain information about the structure of the samples, but not a about its dynamics. Their detectors count neutrons scattered in all the directions from a quite monochromatic incoming beam, but completely disregarding their energy distribution.

The length scales range is chosen depending on the desired information (the structure of the molecule itself, the relative arrangement of close molecules or the formation of superstructures).

The interatomic distances in the system, r, and the modulus of the scattering vector, **Q**, are related through the Fourier transforms of the structure factor S(Q) and the pair correlation function g(r):

$$g(r) = 1 + \frac{1}{2\pi^2 \rho r}\int_0^\infty QH(Q)\sin(Qr)dQ \tag{7}$$

$$H(Q) = \frac{4\pi\rho}{Q}\int_0^\infty r\left[g(r)-1\right]\sin(Qr)dr = S(Q)-1 \qquad (8)$$

Since in an elastic scattering the neutrons do not transfer any energy to the sample, the relation between Q and θ become

$$Q = 2k_0 \sin\theta_E = \frac{4\pi}{\lambda_0}\sin\theta_E \qquad (9)$$

where k_0 and λ_0 are the wave number and the wavelength of the incident neutrons, respectively. Thus, the characteristic distances that can be measured will be related to the wavelength of the incoming neutrons and to the angular range that the detectors cover.

Neutron diffraction measurements on D1b

Neutron diffraction measurements on modified borate glasses have been performed at room temperature, by means of the two-axis D1b diffractometer at the Institut Laue–Langevin in Grenoble. The incident neutron wavelength of 2.52 Å allowed us to access a Q range of 0.5–3.4 $Å^{-1}$.

An orange cryostat (300 K) and a vanadium sample holders with cylindrical geometry were used to measure the samples (*Figure 2*). Measurements on the empty container and on a vanadium slab with dimensions comparable to those of the sample were also carried out. The data were corrected for the contributions of the background scattering from the empty vanadium can, multiple scattering, absorption and were normalized to an absolute scale with the isotropic incoherent scattering of the vanadium.

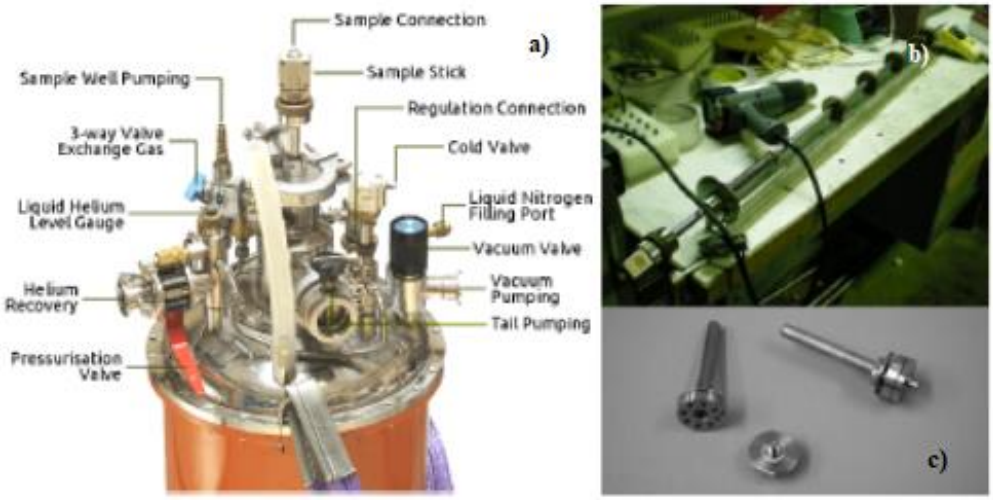

Figure 2*. a) Orange cryostat with the sample stick in place; b) warming and drying of the stick during a sample change; c) vanadium-aluminium sample holders used in D4 and D1B.*

D1B is a two-axis neutron diffractometer located at the ILL (Figure 3). The high efficiency of its position sensitive detector (PSD) and the high neutron flux make this instrument suited for real time experiments and for very small samples, since the diffraction patterns can be measured with satisfactory statistics in just a few minutes.

D1B had a multiwire position sensitive $^{3}He/Xe$ gas detector covering the angular range $2\theta_E$= 2° to 130° and had a 60% efficiency at 2.52 Å (1).

Recently, the detector has been upgraded to a microstrip $^{3}He/CF_4$ position sensitive detector with 1280 cells covering 128° of the scattering range (from $2\theta_E$ = 0.8 to 128.8), and has an increased efficiency at the same wavelength of detecting equal to 86%.

The instrument Figure 3) is located at a thermal guide, where the neutrons are thermalized in the water moderator at 300 K and have a peak at a wavelength of $\lambda = 1.2$ Å. Three monochromators, made of pyrolytic graphite cut parallel to the 002 crystallographic plane, focus on the sample and select neutrons with a wavelength of 2.52 Å.

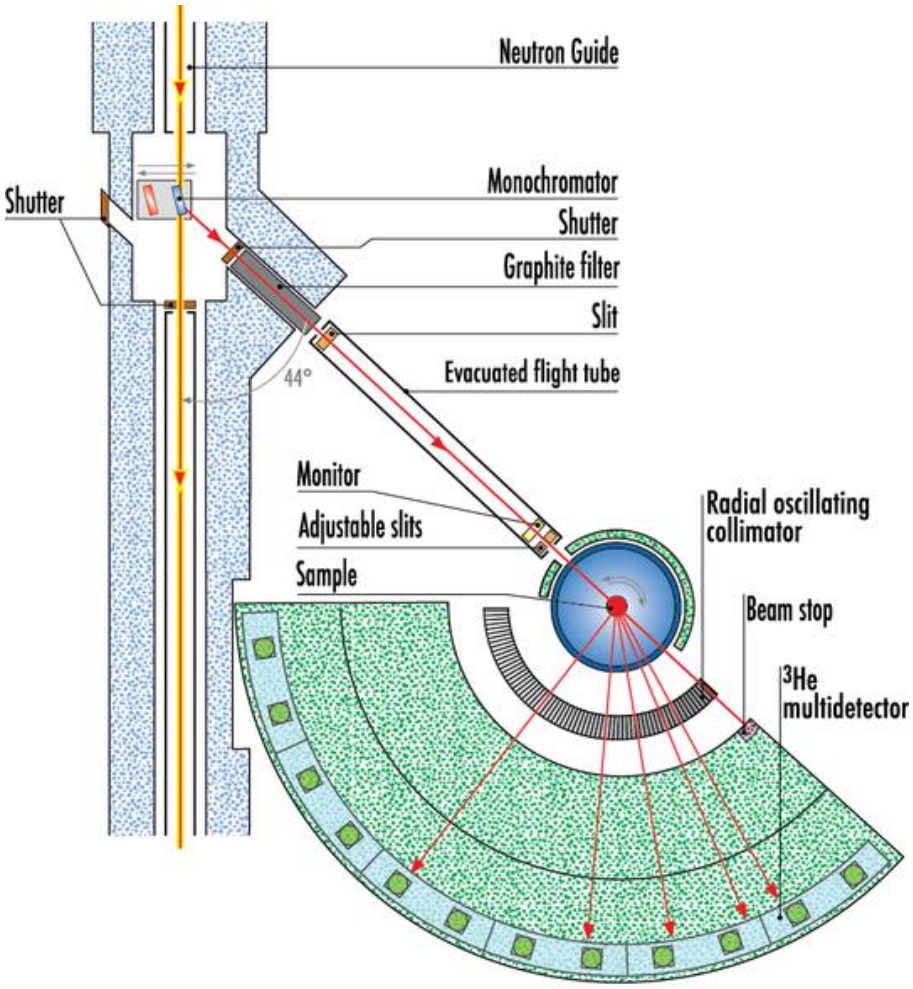

Figure 3. Scheme of the two-axis diffractometer D1B at the ILL **(2)** *(after the detector upgrade).*

Neutron diffraction measurements on D4

The neutron diffraction experiments on densified glasses have been carried out in the Institut Laue-Langevin facilities, at room temperature on the D4 diffractometer with λ=0,49744 Å (327 meV), which yielded a momentum transfer ranging up to Q_{max} =23.5 Å.

After the corrections and normalizations applied at the instrument with the program RegD4c, a diffraction pattern of the neutrons scattered by the sample and its surroundings normalized to monitor counts is obtained. Further data treatment is required to single out the sample contribution.

The computer code Correct (3) has been used to perform the background, multiple scattering and empty container attenuation corrections to the neutron diffraction data, as well as the normalization to another sample of known cross-section and volume (a vanadium rod), modified by a parameter accounting for the fullness of the sample holder.

Moreover the inelastic correction of Placzek (4) is also performed: this method consists in assuming that the static approximation is the best fit and then deriving corrections, which are reasonable for nuclei with little recoil.

D4 is a two-axis diffractometer (5), specially designed to study the short and intermediate atomic order in disordered materials (liquid, amorphous and nano-structured materials and disordered crystal). The short wavelength of the neutrons coming from the hot source and the large angular range covered by the array of microstrip detectors ($2\theta_E$=1.5° to 138°) allow to obtain good quality data up to rather high values of q. It is a significant factor when data has to be Fourier transformed to real space, because it gives a better resolution. Moreover, a large detector system provides not only a high counting rate but also a very good counting-rate stability, which combined with a very low and stable background-counting rate, can determine the local atomic structure of disordered materials with excellent accuracy.

Neutrons at D4 come from its hot source at 2600 K, giving rise a flux peak at 200 meV, which increases the flux of neutrons at smaller wavelengths

(<0.8 Å). The neutron beam goes through a monochromator that selects neutrons within a small range of wavelengths. Since the neutron energy distribution of the source is normally fixed, the more precise the wavelength, the less neutrons are available for the experiment, so an trade off must be found. The monochromator at D4 to obtain neutrons at λ~ 0.5 Å is a very large copper single crystal cut parallel to the 220 crystallographic plane. A low-efficiency detector, called monitor, is placed in the path of the beam before the sample, allowing to have a measure of the incident neutron flux needed for normalization. It, however, lets most neutrons travel through and can be used in the experiment, interacting with only 0.1 to 1 % of them (6).

Just as in D1b, an orange cryostat (T = 1.5 K to 300 K) or a furnace (T =300 K to 1100 K) are used as sample environments in the different experiments (Figure 2). A scheme of D4 diffractometer is shown in Figure 4.

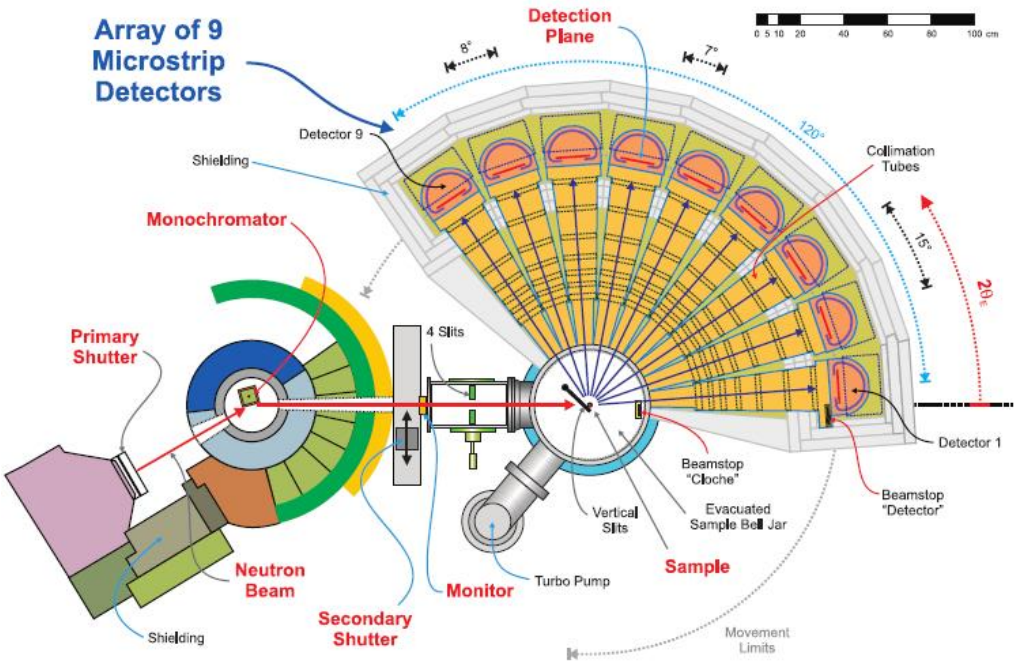

Figure 4. Scheme of D4, a liquid and amorphous materials diffractometer at the ILL **(7)**.

4.1.2 An instrument to determine the vibrational dynamics: inelastic scattering and IN4

The study of the dynamics is approached by perturbing the equilibrium of the system with an external force and studying its relaxation to the equilibrium state.

The atomic dynamics can be investigated by means of inelastic scattering techniques, which involve an energy change of neutrons, gained or lost from the sample. The measurements provides the double differential scattering cross section, $\frac{d^2\sigma}{d\Omega dE_f}$, having the dimensions of an area, with E_f the final energy of the neutron.

In a coherent inelastic scattering from a single excitation, the momentum transfer is $\hbar$Q and the energy transfer is defined as

$$\hbar\omega = E_i - E_f = \frac{\hbar^2}{2m}\left(k_i^2 - k_f^2\right) \quad \textbf{(10)}$$

Our target is the determination of the dynamic structure factor S(Q, ω), which contains the information about the system. It is proportional to the double differential cross-section via

$$\frac{d^2\sigma}{d\Omega dE_f} = \frac{k_f}{k_i} S(Q,\omega) \quad \textbf{(11)}$$

The peaks exhibited in the energy spectrum can be associated with transitions between different crystalline electric fields levels, phonon scattering or magnetic excitations.

Inelastic neutron scattering experiments on densified B_2O_3 have been carried out at room temperature on the time of flight (TOF) spectrometer IN4 at ILL Facility with neutron wavelengths of λ=2.6 Å.

The recorded TOF spectra are used to obtain the scattering function S(Q;ω) of the sample using the standard IN4 data reduction techniques in the LAMP software (8).

In order to compare the different datasets, the intensities are normalized to their monitor counts, making the data independent from the measuring time and from the time fluctuation of the incident flux.

Then, an appropriate subtraction of the background and the empty cell contributions is performed and the calibration to a full absorber, having the same dimensions of the sample plus container system (Cadmium), is also executed.

A further measurement on an elastic incoherent scatterer (vanadium) provides a tool to normalize the data, taking into account the instrumental effects and allowing to determine the instrumental resolution.

IN4 is a TOF spectrometer located at the Institute Laue-Langevin in Grenoble, France, that is used to study excitations in the thermal neutron energy range of 10 to 100 meV (9; 10).The instrument is designed to have a high flux and signal-to-noise ratio with good resolution, by using improved a focusing optics, the background suppression by the chopper system and a large area detector (*Figure **5***).

On IN4, the incoming neutron beam first passes through a shield (Al), protecting the beam tube, which is one of the main losses of flux for the instrument. After the shield, two background choppers act as a low-bandpass filter and eliminate the fast neutrons and gamma rays that give rise to noisy spectra. Thus, a large area (440 cm^2) double curvature monochromator selects a specific incident neutron energy and focus the beam giving a high incident flux at the sample position. The variable curvature of the monochromator in both the horizontal and vertical planes allows to trade intensity for resolution by using variable take-off angles and a time focusing technique. The monochromator assembly, moreover, allows for four separate

crystals, PG(002), PG(004), Cu(111) and Cu(220), to be used for a selection of incident wavelengths.

The best energy resolution is obtained at the longer wavelengths, with minimum $\Delta E_i/E_i \approx 2\%$. A Fermi chopper transforms the incident beam into a set of short pulses required for the TOF technique. Varying the speed of this chopper changes the time resolution. A scheme of IN4 diffractometer is shown in *Figure* ***5***.

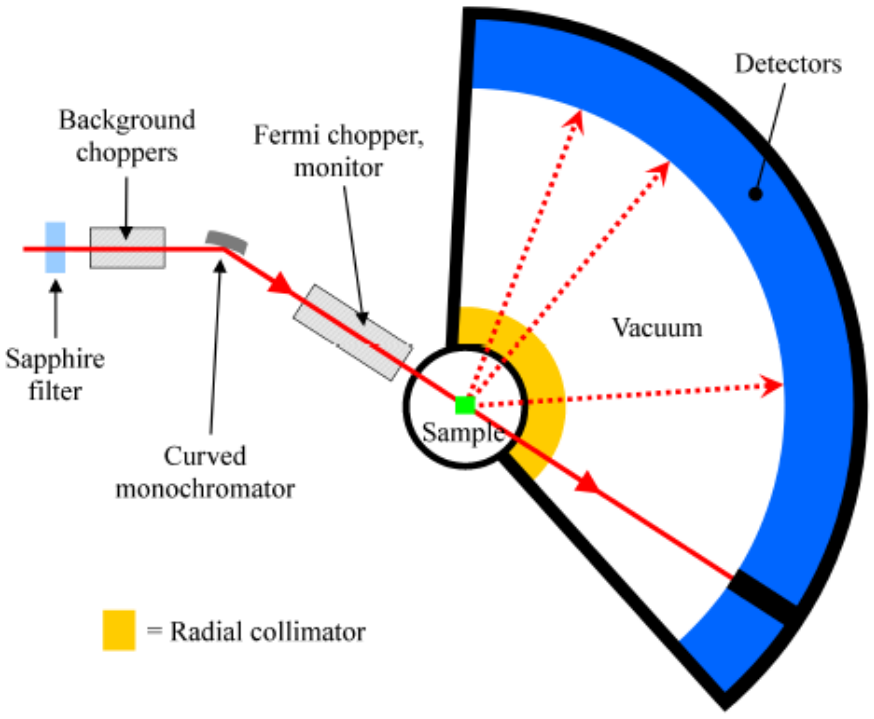

Figure 5. A diagram emphasizing the main elements of the IN4 instrument at a thermal neutron guide of ILL, France **(9)**.

4.2 Raman scattering measurements

Micro Raman scattering measurements were performed with a Jobin-Yvon Horiba LabRam-HR Evolution micro Raman Spectrometer (Figure 6), equipped with liquid nitrogen cooled charge coupled device (CCD) detector and an Olympus BX41 confocal microscope. The data were collected at room temperature by using a 532 nm laser excitation in back scattering configuration with a 1800 lines/mm grating. A 50X objective (numerical aperture 0.100) was used to image the laser spot on the sample, keeping the laser power below 100 mW in order to avoid undue heating effect. The LabRam spectrometer is also equipped with an ULF (Ultra Low Frequencies) module, which allows to analyze the low frequency region down to about 5 cm^{-1}. The accuracy of all stated spectra is within 1 cm^{-1}. To minimize the effect of surface depolarization, before each run of measurement the surfaces of the glass samples were polished.

A very low power (0,01 mW) was differently used for the measurements on the ruby pressure markers inside the DAC cell, because of their extremely high fluorescence signal.

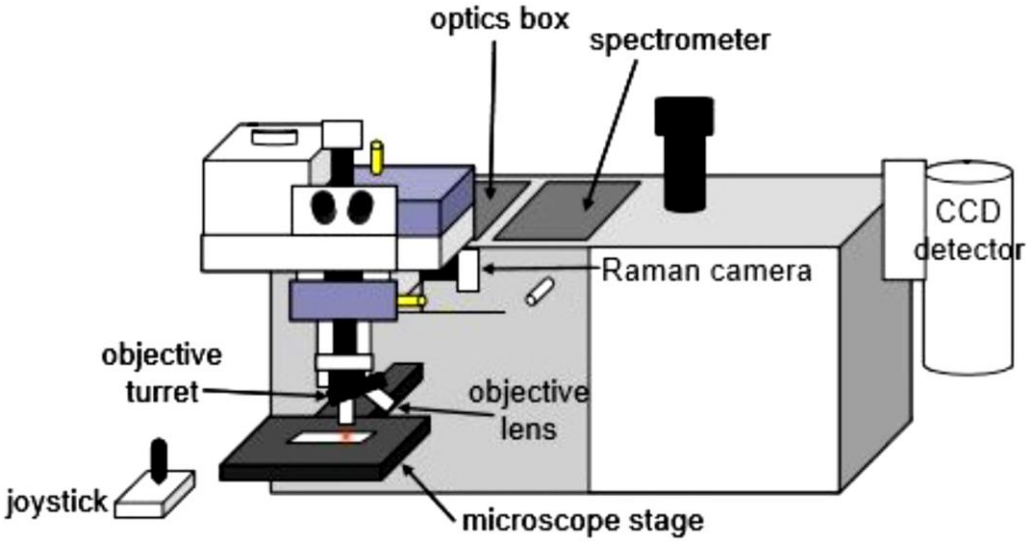

Figure 6. Jobin-Yvon Horiba LabRam-HR Evolution micro Raman Spectrometer set-up.

4.3 Low temperature specific heat measurements

The specific heat capacity was measured over the range between 1.5 and 30 K by means a home-made automated calorimeter, which operates by the thermal relaxation method in a ^{4}He cryostat (11).

Samples of about 20–30 mg were bonded to a silicon chip (bolometer), used as sample holder by vacuum grease Apiezon N to optimize the thermal contact. A SMD (surface mounting device) resistor and a constantan strain gauge were attached to the other chip surface using a thermosetting resin.

The cryostat is immersed in liquid helium. The 1.5 K heat sinks thermalize the wires before connecting them to the sample holder. In this way, parasitic heat flows from the surroundings at room temperature are avoided. The temperature of the isothermal block is regulated by a Lake Shore resistance bridge, which uses the surface mounting device SMD as thermal regulation sensor and the constantana wire as heater element. The temperatures of the whole cryostat are measured by a calibrated germanium thermometer.

Current is sent to the heater, which is used to increase the temperature of the sample from T_0 (which is the temperature of the isothermal block) to $T_0 + \Delta T$, during a time interval t. After this delay time, the current is turned off and the temperature decreases according the relation

$$T = T_0 + \Delta T e^{-t/\tau} \qquad (12)$$

where τ=C/K, C being the heat capacity of the whole system (sample + bolometer + addenda) and K the thermal conductance of the wires that connect the bolometer to the sample holder.

C is determined by fitting the measured decay by an exponential curve. The heat capacity of the sample, C_s, is computed by subtracting to C the bolometer and addenda contributions, which are measured during a different calorimetric run.

In Figure 7 a detailed schematic illustration of sample holders is displayed.

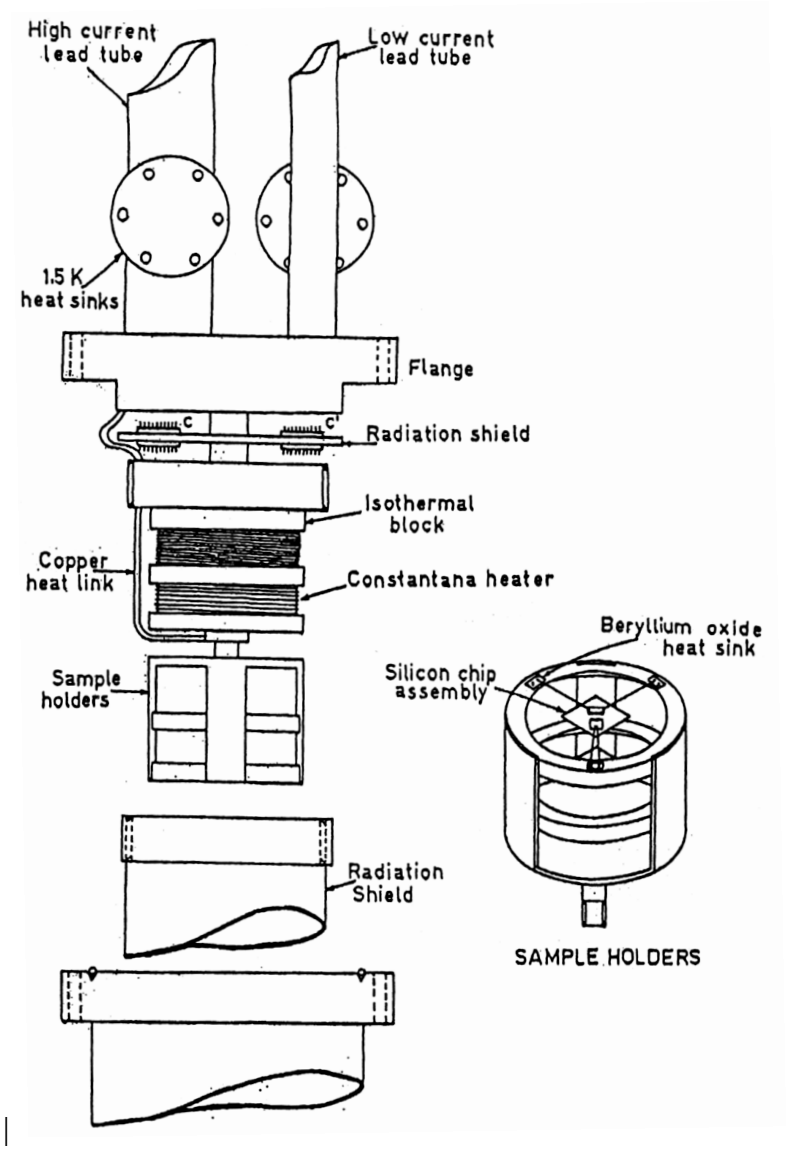

Figure 7. Cryostat and sample holder for low temperature calorimetry.

4.4 In situ-high pressure measurements: the Diamond Anvil Cell

As pointed in Chapter 2, high-pressure in-situ experiments are of paramount interest to get insight into the nature of the low energy excitations contributing to the Boson peak and the origin of the intermediate order range structure of glasses.

Thus, a consistent time period of my doctorate has been spent for designing and operating Raman experiments in which a diamond anvil cell (DAC) was used to apply high pressure (up to 30 GPa) to a sample of interest.

This task is far from being trivial, due to the intrinsic difficulties to manage these cells and to obtain good Raman signal from very small samples enclosed in a DAC.

In this thesis the results of an experiment on an α-quartz sample are shown. This investigation should be considered as a preliminary study that will pave the way for new and more specific in-situ high-pressure experiments. It is worth noting that, although the achieved results on in-situ high pressure Raman experiments at present are not so many, this technique has been introduced for the first time at the Laboratory of Optical spectroscopy of the University of Messina.

Therefore, in the following, a detailed description of the cell, the assembly and the experimental setup will be given.

4.4.1 An overview

The diamond anvil cell (DAC) is fast becoming the most powerful ultra-high-pressure device, helping physicists and chemists to discover new states of matter and understand the basic physics underlying ultra-high-pressure phenomena.

The DAC (*Figure 8*), indeed, is the only high-pressure device that makes possible the investigation of in-situ transformations at pressure above 1 GPa within a wide range of pressure (0 - 300 GPa) and temperature (4-7000 K).

Thanks to these valuable prerogatives the DAC has been used to recreate the condition existing in the depth of planets, to synthesize materials and phases not observable under normal ambient conditions.

Nevertheless, this technique presents big limits because of the very little sample sizes (5-50 μm), difficult to be handled and producing a low signal in the measurements.

Figure 8. Pictures of two Diamond anvil cell

The samples under high pressure, illuminated by X-rays or visible light, can be observed through the diamonds, allowing to perform measurements of X-ray diffraction, fluorescence, optical absorption, photoluminescence, Mössbauer, Raman and Brillouin scattering, positron annihilation on the system of interest (12).

Moreover, by applying externally magnetic and microwave fields it is possible execute magnetic measurements, such as cell nuclear magnetic resonance, electron paramagnetic resonance (13). High-temperature heating of the sample is also possible by attaching electrodes (up to 2000 K) or using laser-induced heating (up to 7000 K) (14) (15), as well as the cooling down to a few millikelvins (16).

4.4.2 Technical features

The basic principle of the DAC device consists in placing a metal gasket containing the sample, a pressure transmitting medium and a pressure sensor between the smallest parallel faces of two diamond anvils (culets): by pushing the opposed anvils one against the other, the compression of the sample occurs.

The uniaxial pressure supplied by the diamonds is transformed into uniform hydrostatic pressure by using a pressure-transmitting medium, which is supposed to support no shear. The typical systems used to transmit the pressure are argon, neon, nitrogen, helium, iso-n pentane, paraffin oil, silicon oil, or a mixture of methanol and ethanol (16; 17).

The pressure-transmitting medium is confined by the two diamond anvils and a metallic gasket (generally made of steel), as schematized in Figure 9. The pressure is monitored by using a reference material whose behavior

under pressure is known. Commonly the pressure standards used in the DAC cells are ruby (18; 19) or various structurally simple metals, such as copper or platinum (20). The value of the highest applicable pressure will depend on the ratio of the surface on which the force is applied and the diamond culet size. However, also the gasket material will influence the pressure.

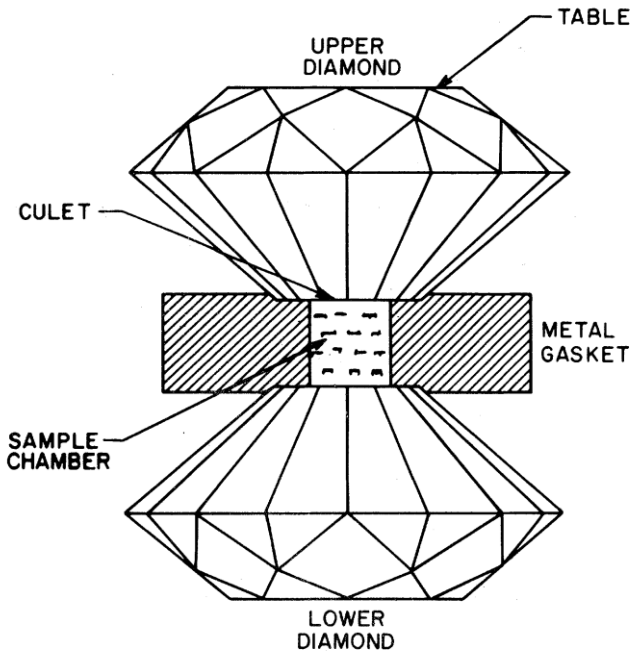

Figure 9. The scheme of a DAC cell: two opposed diamond anvils, a metal gasket for pressure transmitting medium confinement.

Typically, a DAC consists of two diamonds, fixed on support plates. If the pressure applied on a plate is greater than the plastic deformation, the diamonds will be damaged or break: therefore, materials with a high plastic deformation, such as diamond, are required (21). A perfect assembling and

alignment of the two circular sections of the cell (lower and upper) allows to get high pressures without the breaking of the anvils.

Two types of DAC cells can be generally used to perform high-pressure experiments:

- *membrane cells*. The fine calibration of force is applied by a metallic membrane, which is inflated with pressurised gas (typically helium or nitrogen) through a thin stainless steel capillary. The metallic membrane is inserted between the upper plate and a steel cylinder, which contains the two plates, and its dilation presses a diamond on the other, closing the cell. The pressure exercised by the gas on the membrane can be visualized through a pressure-measuring device, while the pressure inside the cell can be measured indirectly by the ruby fluorescence (see section 4.4.5).

- *screw cell*. Three or more screws pull the two plates together, carrying the diamond anvils with them.

4.4.3 The choice of the anvil

The diamond is the best material for the construction of high-pressure anvils, thanks to its mechanical (strength and hardness), thermal (good conductor of heat), electrical (good insulator), optical (low birefringence, low photoluminescence) properties.

Indeed, the microscopic structural arrangement of the carbon atoms covalently bound with a tetrahedral disposition makes the diamond the hardest known available substance. Moreover, the diamond is optically transparent in broad regions of the UV-IR spectrum.

According to their degree of purity and the presence of nitrogen impurities that affects the optical properties, the diamonds are classified in type-I A and

type II A. Type-I A diamonds (~2x10³ ppm of nitrogen) show a characteristic IR absorption band centered at 1200 cm^{-1} (Figure 10 a), related to the impurities; type-II A diamonds, not having impurities (~1 ppm of nitrogen), do not present the IR band at 1200 cm^{-1}, and show only the IR absorption band between 1800 and 2200 cm^{-1} (Figure 10 b) (21).

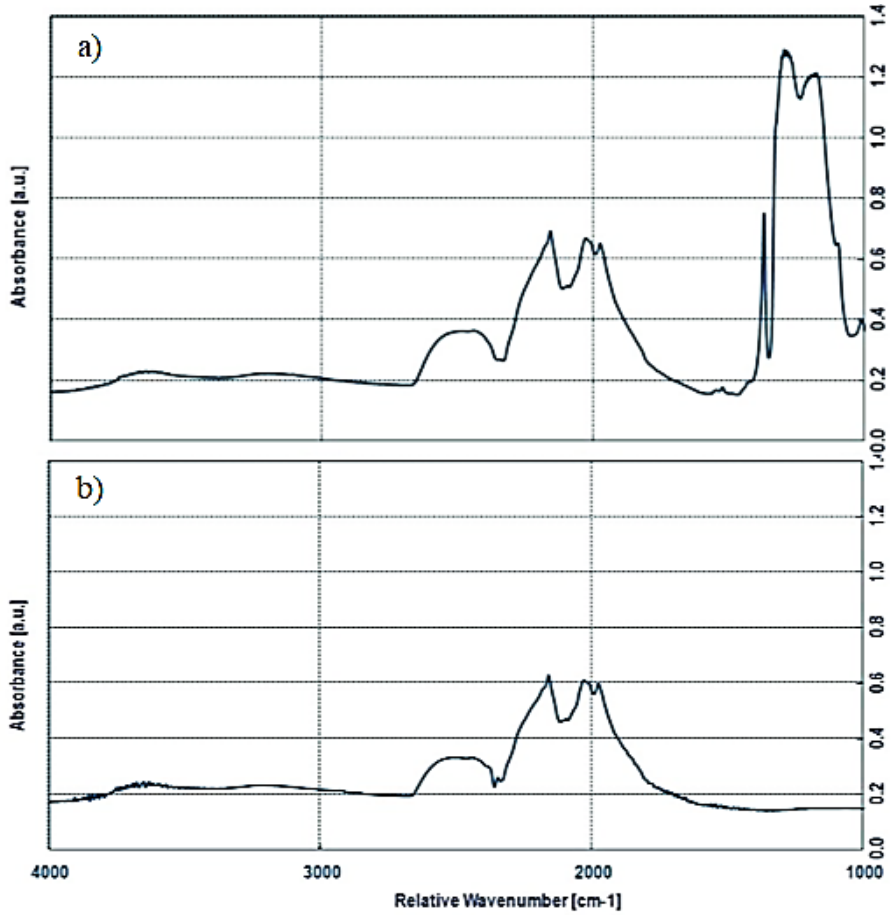

Figure 10. IR spectrum of a) type-I A and b) type-II A diamond anvil. Type-I A diamonds show an absorption band centered at 1200 cm^{-1}; type-II A diamonds show only the IR absorption between 1800 and 2200 cm^{-1}.

Great differences are also observable in Raman spectra. Despite the first order of both type-I A and type-II A diamonds show a sharp peak at 1332 cm^{-1}, their second order Raman spectra differ: type-IA diamonds have a flat fluorescence background under the two-phonon transition band between 2200-2700 cm^{-1} (*Figure **11*** a), type-II A diamonds show a fluorescence increasing with the frequency (*Figure **11*** b).

Type-IA diamonds with low fluoresce and ultra-low fluorescence are also available showing the intensity of the two-phonon Raman transition at 2564 cm^{-1} respectively 1.25 and 2 times the intensity of the background fluorescence of diamond (*Figure **12***). All diamonds to be used for anvil manufacture are generally examined under a polarizing microscope for birefringence. Diamonds with significant birefringence discontinuity (>0.0001), typical of inclusions, are rejected. In addition diamonds can be selected for ultralow birefringence (<0.00005).

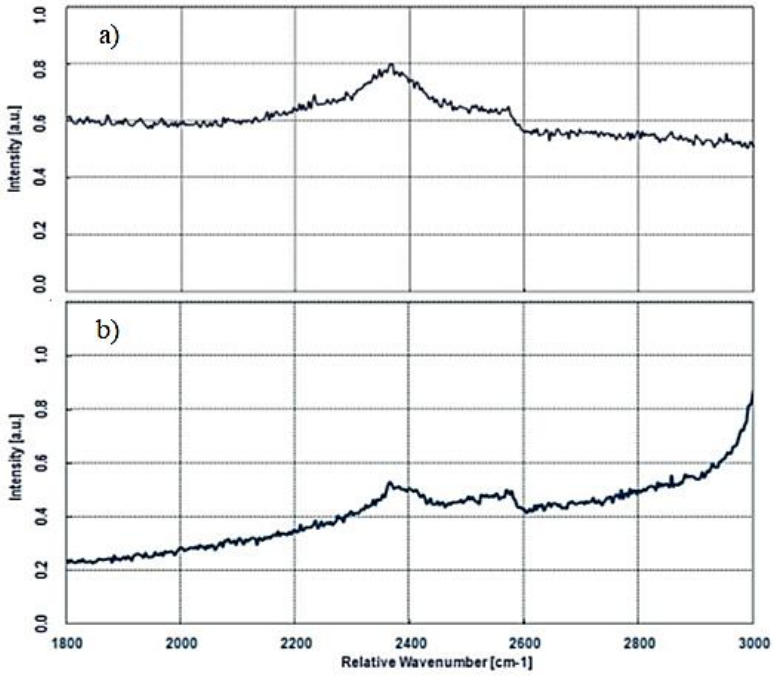

Figure 11. Second order Raman spectrum of a) type- I A without Raman low fluorescence selection and b) type- IIA diamond anvil. Both type-I A and type-II A diamonds show a sharp peak at 1332 cm^{-1}. Type-IA diamonds have a flat fluorescence-background under the two-phonon transition band between 2200 and 2700 cm^{-1}; type-II A diamonds show a fluorescence increasing with the frequency.

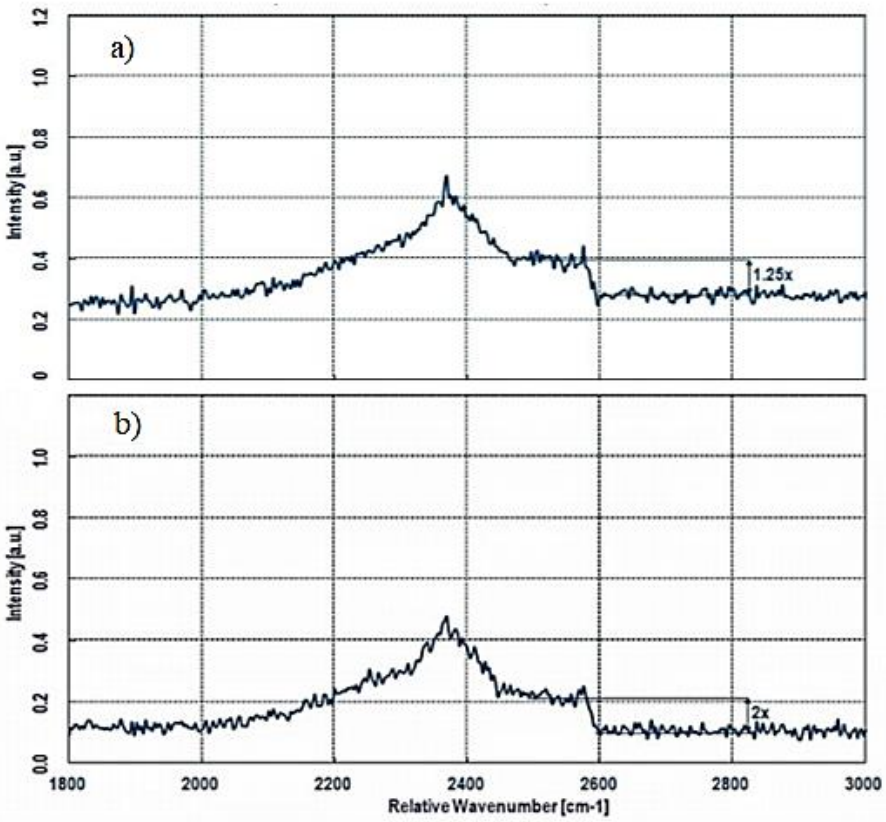

Figure 12. Second, order Raman spectrum of type-IA diamond anvil with a) Raman low fluorescence selection and b) Raman ultra-low fluorescence selection. They show the intensity of the two-phonon Raman transition at 2664 cm^{-1} respectively 1.25 and 2 times the intensity of the background fluorescence.

A further significant aspect is the choice of the diamond size for the DAC, which generally is related to the desired pressure. Standard design anvils are made from rough diamonds. Then, they are polished according to the (100)-crystal orientation for the highest strength. The dimensions of the anvil generally follow determined proportion (*Figure **13***).

X in mm	Appr Weight	
2.50	0.09	
2.75	0.12	
3.00	0.16	
3.25	0.21	
3.50	0.26	
3.75	0.32	
4.00	0.38	
4.25	0.46	
4.50	0.55	
4.75	0.64	

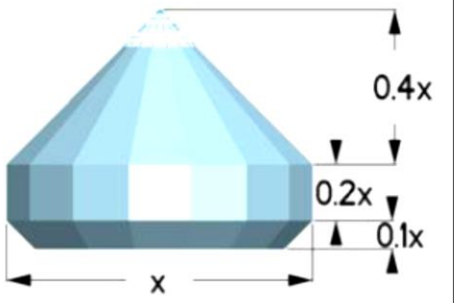

Figure 13. Standard design, dimensions and approximate weight of type -I A (100)-oriented diamonds.

The common diamond anvil has 16 facets and the diameter of the larger face of the diamond can vary between 2 and 4.5 mm, while the culet diameter can be between 50 μm and 1.2 mm: the higher the ratio between the two surfaces, the greater the magnification of the applied force to the sample and the pressure (Table 1).

Maximum pressure	Culet size
<5 GPa	> 1.00 mm
5-100 GPa	1.00 mm – 0.20 mm
> 100 GPa	< 0.20 mm, bevels up to 0.30 mm at 8°

Table 1. Maximum reachable pressures related to the culet size of the diamonds

The use of diamond for the anvil cell, however, presents some limiting factors, such as the high costs and the not negligible signals into a portion of IR and UV spectrum. Therefore, other materials, such as the sapphire, have been studied to be employed as anvil in high-pressure cells. Sapphire anvils cell (SAC) have indeed low fluorescence and high IR transmittance (*Figure **14***), but they do not allow to reach values of pressure as high as in the diamond.

Finally, thus, the choice of the anvil have to be a good compromise between the achievement of a high pressure and a low signal in region of interest for the investigation.

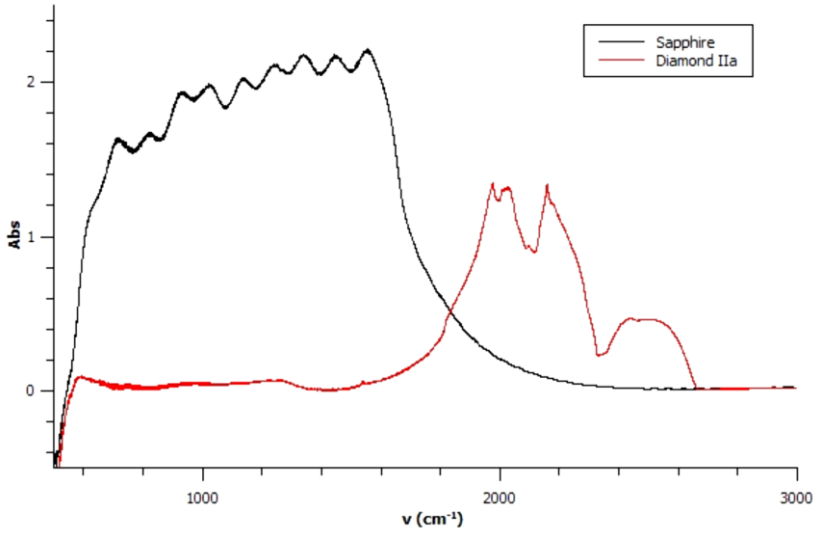

Figure 14 . Absorption spectra of a type – II A diamond (red line) and a sapphire (black). Note that there is not absorption by the sapphire at 2500 cm^{-1}.

4.4.4 Indenting, drilling and charge of sample

Before starting the in situ measurements, a series of precise and complicated steps are required: the diamonds alignment, the gasket indenting, its drilling, the sample charging and the filling with the pressure-transmitting medium.

At the beginning, the upper and lower diamonds have to be carefully aligned with each other. After having correctly fit in the plates of the cell, three symmetrically situated micrometric screws let to translate the stationary diamond mount and rule the concentricity. Moreover, the hemispherical mount can be tilted in its socket by adjusting three other screws to secure parallel alignment of the diamonds: the correct position, under white light and with a distance between the two diamonds lower than 60 μm, will bring up an optical interference fringe pattern along the optical axis (Figure 15).

Figure 15. *Optical interference fringe pattern of aligned diamonds observed with a 10X microscope*

To confine the hydrostatic medium between the two diamonds a metal thin foil, the gasket, is used. Its thickness is primarily about 100-250 μm, its shape varies according to the cell geometry and the material is generally steel or rhenium.

A pre-indenting of the gasket is carried out: the gasket is placed between the anvils and a pressure is applied to the diamonds, deforming plastically and symmetrically the gasket from both sides and generating a crater, whose imprint depends on the shape of the diamonds. The deeper the indentation, the higher the achievable maximum pressure. The initial thickness of the foil varies from 250 to 200 μm and the thickness after indenting from 150 to 100 μm.

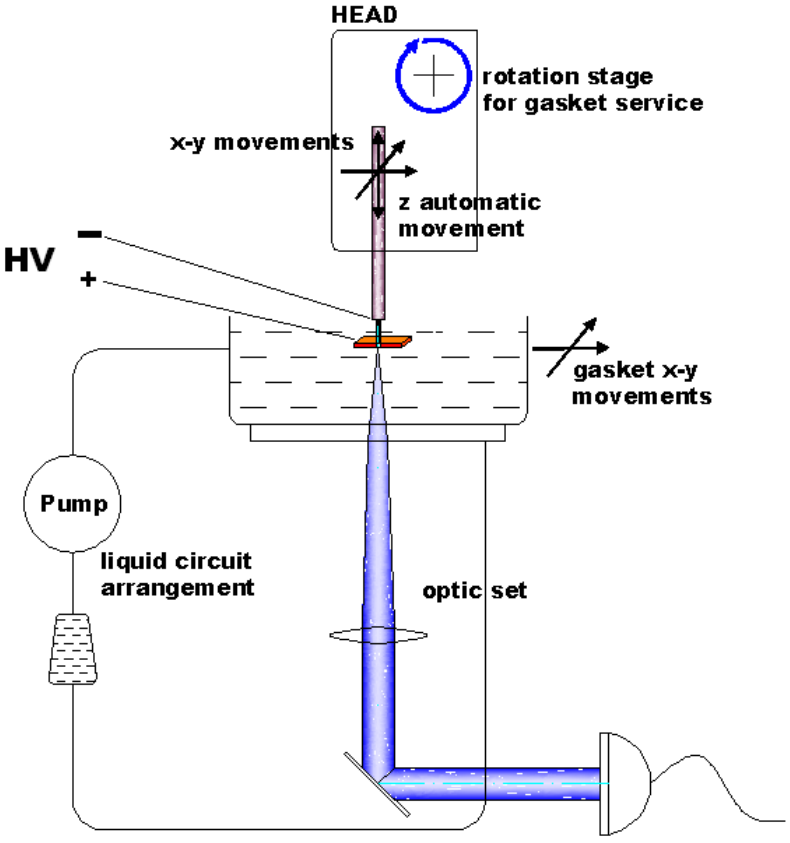

Figure 16. General scheme of a Spark Eroder. It is constituted by a power source that supplies a pulsed discharge between one tip (anode) and a gasket (the cathode), through a dielectric liquid. The whole erosion process (advance of the tip, level of

discharge, alignment of the elements) is managed by a software through the visualization on a monitor.

After the indenting, the gasket is drilled at the center of indentation (generally 200 μm in diameter hole) by an Electric Discharge Machine (EDM) or Spark Eroder (Scheme in *Figure 16*).

This device removes material from the workpiece (gasket) by a series of rapidly recurring current discharges (sparks) between two electrodes (tip and gasket): the electrical potential is applied between gasket and tip, separated by a dielectric liquid, and the discharge crosses the conductors producing heat, so that the material from the gasket evaporates explosively.

It is fundamental to have a flat tip, with a sharp circular edge in order to have a homogeneous discharge and obtain a circular hole.

The gasket is seated on the lower diamond flat in the same orientation as it had when taking the indentation. Then, the sample and a ruby chip are placed in the hole.

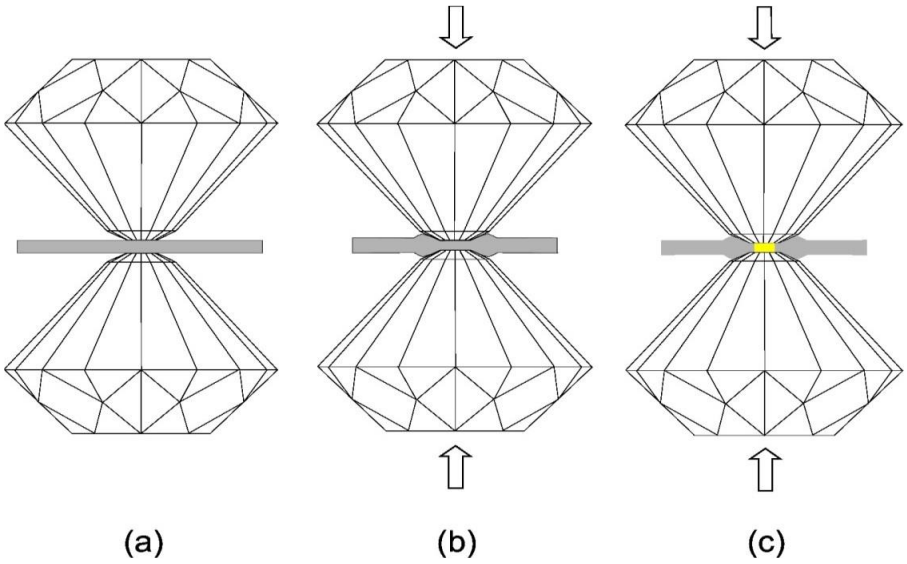

Figure 17. The procedure for indenting: a) the metal foil (gasket) is placed between the two diamonds; b) it is deformed by applying a pressure by means the diamond anvil; c) The sample region (yellow zone) is realized by drilling the gasket in its center.

The problem of the sample charging in a DAC cell is also of considerable importance because of its reduced dimension: the sample available space is given by the gasket thickness (typically 200 μm or less) and the central hole diameter (typically 30-50% culet size); therefore the sample size cannot exceed a diameter of 20-30 μm needing a thin needle for the charge.

This process is followed by filling the hole with the fluid and sealing by bringing the upper anvil on the gasket.

The gasket, in addition to providing the containment for the pressure medium, acts as a supporting ring, preventing the failure of the anvils due to a concentration of stresses at the edge of the anvil faces.

4.4.5 The pressure monitoring inside the cell: the ruby fluorescence

The force on the cell is produced through a metal membrane pressed by a gas (for membrane cell), or by using a dynamometric key (for screw cell).

However, the pressure on the sample cannot be faithfully deduced from the membrane gas pressure or from the torque applied through the key, since several intrinsic factors affect the pressure.

The most used way for correctly measuring the pressure inside the cell is the method of ruby fluorescence, in which the pressure is determined by the wavelength of a specific ruby emission line.

Indeed, using well-established freezing points of several liquids and some solid-solid transitions as fixed points, it was observed that the lines position shifts almost linearly with hydrostatic pressure in a wide range, and that the line broaden if the pressure on the ruby is non-hydrostatic (18).

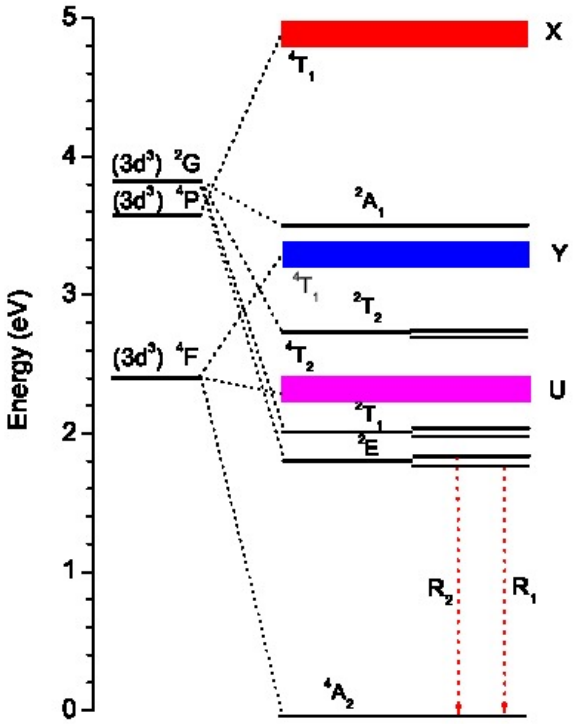

Figure 18. Cr3+ energy levels in ruby. R1 and R2 lines correspond to the transitions $^4Ag\ (t_{2g}^3) \leftarrow {}^2E(t_{2g}^3)$.

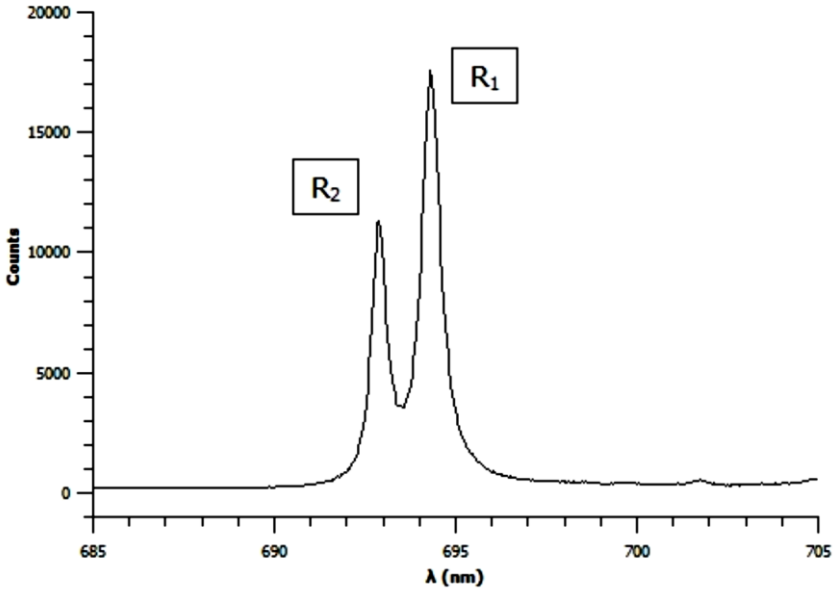

Figure 19. Ruby emission spectrum, at 300 K and ambient pressure, consists of two lines with wavelength 694.25 nm (R1) and 692.86 nm (R2).

Ruby is an aluminum oxide (Al_2O_3), doped with Cr^{3+} ions and it has a crystalline structure similar to corundum. The two fluorescence transitions ^4Ag (t_{2g}^3) $\leftarrow ^2E(t_{2g}^3)$ between the Cr^{3+} energy levels (Figure 18), well described by crystalline field theory, determine in the ruby emission spectrum, at 300 K and ambient pressure, two intense lines R_1 and R_2 (*Figure 19*), respectively with wavelength 694.25 nm and 692.86 nm (22). The R lines energy is quite sensitive to the concentration of Cr^{3+}, the temperature and the pressure.

Particularly, R_1 exhibits a positive shift above room temperature with temperature (23):

$$R_1(T) = 14\,423 + 4.49 \times 10^{-2}\,T - 4.81 \times 10^{-4}\,T^2 + 3.71 \times 10^{-7}\,T^3 \quad (13)$$

Conversely, by increasing the pressure, the R lines shift at higher wavelengths. The line trend with pressure is well described by the Mao-Bell equation (24) :

$$\boldsymbol{P\,(GPa) = \frac{A}{B}\left[\left(\frac{\lambda}{\lambda_0}\right)^{B} - 1\right]} \quad (14)$$

where P is expressed in GPa, A is a parameter equal to 1904 GPa, λ_0 is the wavelength of the ruby fluorescence line R_1 at pressure and room temperature, expressed in nm; the B parameter is related to the conditions of the measurements. According to the shock-wave primary calibrations, B is equal to 5 under non-hydrostatic conditions, 7.665 for quasi-hydrostatic conditions and 7.715 under hydrostatic conditions (24; 25). A plot of the relative ruby line R_1 shift against pressure is shown in *Figure 20*.

The tiny chip of ruby, used in DAC cell as pressure sensors, have typical dimensions of 5-10 μm and its fluorescence lines are quite intense.

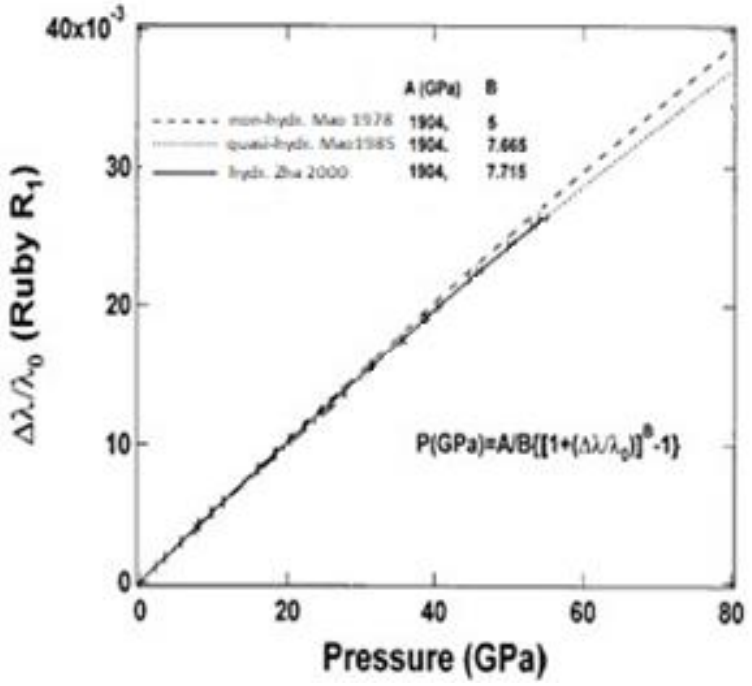

Figure 20. *Relative shifts $\Delta\lambda/\lambda_0$ of ruby fluorescence line R_1 with pressure (in Giga Pascal) for non- hydrostatic (dashed line), quasi – hydrostatic (dotted line), hydrostatic (solid line) liquid condition.*

4.4.6 Pressure-transmitting media

High-pressure experiments are aimed to be carried out under hydrostatic conditions: indeed, being hydrostatic pressure a thermodynamic parameter, the results obtained under such conditions are intrinsic material properties comparable with theory.

The transmitting media are supposed to support no shear. Unfortunately, the melting line of fluids increases under pressure and the solidification inevitably occurs; then, non-hydrostatic effects, such as inhomogeneous

pressure distribution (pressure gradient) and uniaxial (deviatoric) stress, appear, strongly influencing the physical state of the samples (26; 27).

This leads to a decrease in the quality and accuracy of the data and often to the appearance of anomalies. The hydrostatic limits of the media used for transmitting pressure can be empirically determined by considering the ruby R_1 line broadening $\Delta\Gamma$. However the most sensitive and reliable criterion for measuring the pressure homogeneity across the chamber consists in determine the standard deviation σ of the pressures P_i, related to N ruby chips distributed over the area of the gasket aperture (28):

$$\sigma = \sqrt{\frac{1}{\mathrm{N}}\sum_{i=1}^{N}\left(P_i - \overline{P}\right)^2}$$

where $\overline{P}$ is the average pressure, given by $\overline{P} = \frac{1}{\mathrm{N}}\sum_{i=1}^{N} P_i$.

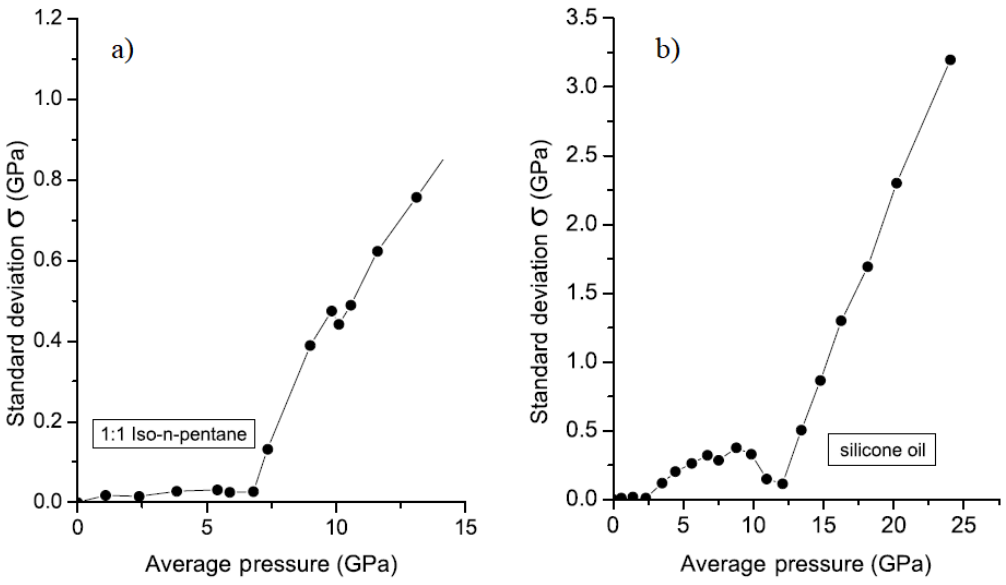

Figure 21. Pressure dependence of the standard deviation σ for a) 1 : 1 iso-n-pentane and b) silicon oil.

For purely hydrostatic pressures it shall be verified that $\sigma = 0$. Indeed, under this condition, after subtracting small but detectable offsets determined at the lowest pressure (P=0), all ruby spheres strictly indicate the same pressure.

When the solidification of the pressure transmitting medium is reached, σ start to deviate from zero.

Many pressure-transmitting media are used for high-pressure experiments in DAC cells (26; 27) .

The most commonly used pressure transmitting medium is 4:1 methanol-ethanol mixture, which is hydrostatic up to 10,5 GPa at room temperature; interestingly, a small addition of water to this mixture in the proportion 16:3:1 methanol-ethanol-H_2O moves the glass transition of the alcohol mixture to 14,4 GPa (29; 30). Conversely, it was found that in 1:1 and 5:1 iso-n pentane mixtures the onset of detectable pressure gradients at 300 K is easily seen at 7.4 GPa (26) (*Figure **21*** a).

In recent years, the use of silicon oils as pressure transmitting has also increased significantly.

The transmitting medium can be also in solid phase: powder grains of potassium bromide (KBr) are often selected for high-pressure infrared (IR) spectroscopy experiments in DAC because of the transparence in the mid-IR range (31; 32). Unlike gas or liquid pressure-transmitting media, the hydrostatic limit of KBr cannot be defined easily because of the uniaxial load and deviatoric stresses between the axial and radial stress components (respectively in the direction normal and parallel to the DAC culet face). KBr can be pratically considered as quasi-hydrostatic pressure-transmitting medium up to 2.14 Gpa, where the differences between the axial and the radial stress components are about 0.063 Gpa. However, above this pressure, its behavior become non-hydrostatic: indeed, the KBr phase transition from B_1 to B_2 at 2.3 GPa results in a constantly increasing deviatoric stresses with increasing pressure, which becomes 0.93 GPa at 5.63 GPa.

The highest hydrostatic limits of pressure media are evidenced by condensed gases (nitrogen, helium, neon, Argon, nitrogen), the use of which requires special filling techniques (33).

In nitrogen the first pressure gradients (±0.02 GPa) appear slightly beyond 10 GPa; then, the gradient rapidly increases and reaches 0.6–0.8 GPa at an average pressure of 20 GPa, i.e. 3–4%.

Among the rare gases, Argon has the advantage that it is relatively easy to load and inexpensive. However, it has a low solidification pressure (1.4 GPa at 300 K) and it shows the first signs of non-hydrostaticity at 2 GPa reaching a standard deviation 0.1 GPa at 10 GPa (1%); then it seems to increase more rapidly above ∼20 GPa.

In Neon the onset of detectable pressure gradients at 300 K is seen at 15 GPa, where the standard deviation starts to increase under pressure to reach a value lower than 0,5 GPa at 50 GPa, i.e. less than 1 %.

Helium is unquestionably the best available pressure-transmitting medium, even in its solid state, i.e. above 12.1 GPa at 300 K. Its standard deviation remains flat up to ∼23 GPa, but even beyond the values of pressure gradients remain very small: at 40 GPa the standard deviation of pressure detected by the different ruby spheres is lower than 0,15 GPa, i.e. 0.4%.

A comparison between the solidified gases in the 0–10 GPa range are shown in *Figure 22*.

It is possible to observe that, in the 0–10 GPa range, nitrogen can compete with neon, despite its lower solidification pressure. Therefore, up to 10 GPa nitrogen could be a very suitable alternative to neon, which is costly and more difficult to load.

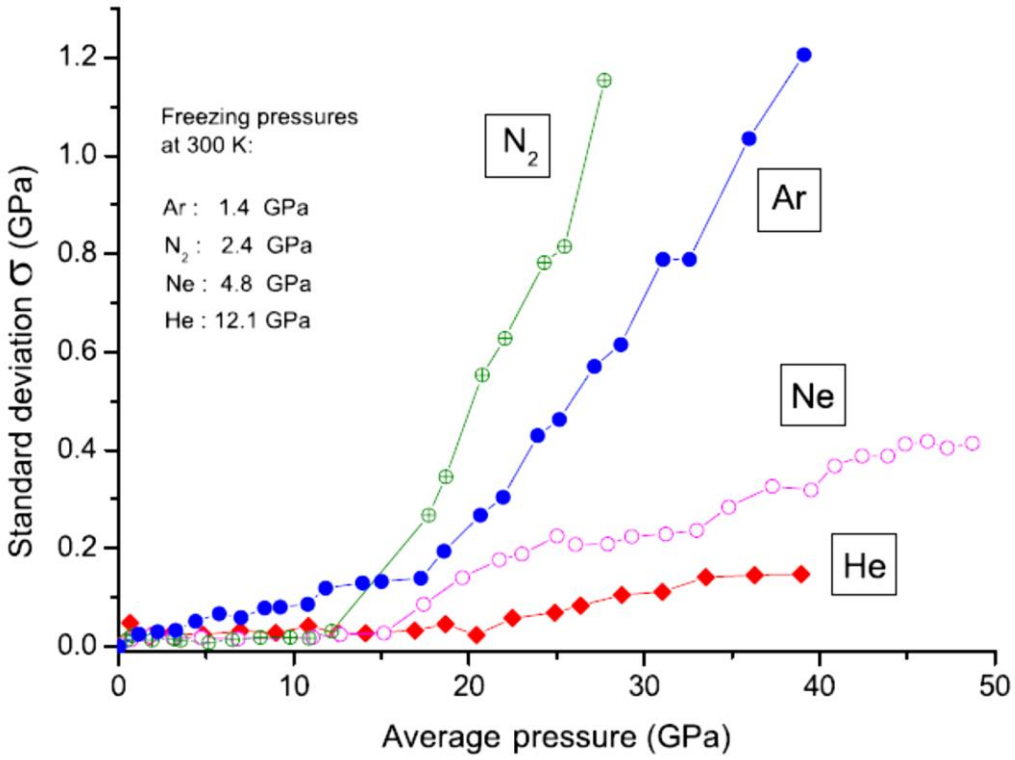

Figure 22. Comparison of pressure dependences of the standard deviation σ of N_2, Ar, Ne and He. The inset gives their freezing pressures at 300K **(17)**.

4.4.7 Experimental details of DAC measurements

In the experiments, a three-screw diamond anvil cell (DAC) has been used to apply pressure. The cell was equipped with type-IA diamond anvils (~$2x10^3$ ppm of nitrogen), characterized by16-sided, Ultra Low Raman Fluorescence and (100)-orientation.

Moreover, the anvil has a 3.25 mm diameter, a 0.50 mm culet and bevels up to 0.70 mm at 8°.

A 200 μm thick stainless steel disk, pre-indented to 100±10 μm, has been used as a gasket material. Gasket drilling has been performed by using the

automatic Spark Eroder SEA 303 equipped with tungsten electrodes, which generated a 200 μm diameter cavity acting as a sample chamber. The pressure-transmitting medium was extremely low fluorescence oil Cargille type HF.

The frequency change of the R1 fluorescence line was obtained from the spectra of two different ruby grains with 15 and 20 μm diameters.

The pressure on the cell was produced by tightening three screws through a dynamometric key, ranging between 0 and 120 N·cm and having a 1 N·cm sensibility.

The uncertainty on pressure determination increases with pressure, as observable in the line R enlargement, due to the loss of liquid hydrostaticity. The B parameter used in Mao-Bell Equation for the pressure calculation is 7.665 (quasi-hydrostatic conditions).

The investigated sample is a 20 μm grain of α-quartz.

References

1. C.H. Lee, M.K. Moon, et al., Instruments and Methods in Physics Research A, 2003.

2. H. E. Fischer, A. C. Barnes, P. S. Salmon, Rep. Prog. Phys., 69, 233 (2006).

3. M. A. Howe, R. L. McGreevy, and P. Zetterstrom. Correct: A correction program for neutron diffraction data, NFL Studsvik internal report (1996).

4. G. Placzek, Phys. Rev., 86-3, 377 (1952).

5. Institut Laue-Langevin. The Yellow Book 2008 - Guide to Neutron Research Facilities. Institut Laue-Langevin, Grenoble (France), 2008.

6. P. K. Willendrup, et al., Component Manual for the Neutron Ray-Tracing Package McStas, Roskilde (Denmark), 2011.

7. H. E. Fischer, G. J. Cuello, et al. Appl. Phys. A: Mater. Sci. Process., 74 (Part 1 Suppl. S), S160, (2002).

8. D. Richard, M. Ferrand, and G. J. Kearley, "Lamp," http://www.ill.eu/instrumentssupport/.

9. G. Cicognani, ed., Guide to the Neutron Research Facilities at the ILL, The Yellow Book (2008).

10. G. Cicognani, H. Mutka, and F. Sacchetti, Physica B 276, 83 (2000).

11. G. Carini, G. D'Angelo, S. Interdonato, G. Salvato and G. Tripodo, Atti Acc. Peloritana 72, 329 (1994).

12. I. Kantor et al., Rev. Sci. Instr. 83, 12, 125102 (2012).

13. S. E. Bromberg, I. Y. Chan, Rev. Sci. Instrum. 63 – 7, 3670 (1992).

14. N. V. Chandra Shekar, et al., J. Mater. Sci. Technol., 19, 518 (2003).

15. N. Subramanian, et al., Curr. Sci., 91, 175 (2006).

16. A. Jayaraman, Rev. Sci. Instrum., 57- 6, 1013 (1986).

17. S. Klotz, J. C. Chervin et al., J. Phys. D Appl. Phys., 42 (2009).

18. R. A. Forman, G. J. Piermarini et al., Science,176, 4032 - 284 (1972).

19. K. Syassen, high pressure res. 28, 75 (2008).

20. R. Kinslow, A. J. Ray, Academic Press (1970).

21. R. Bini, V. Schettino, HP-mat., World Scientific Book (2013).

22. J. C. Chervin, and al., High Press. Res., 21, 305-20 (2001).

23. D. D. Ragan, and al., Jour. Appl. Phys. 72,12, 5539 (1992).

24. H. K. Mao, P. M Bell, J. Shaner, D. J. Steinberg, Appl. Phys. 49, 3276 (1978).

25. C. S. Zha, H. K. Mao, R. J. Hemley, Proceedings of the National Academy of Sciences, 97-25, 13494 (2000).

26. S. Klotz, J.C. Chervin, P. Munsch, G. Le Marchand, J. Phys. D- Appl. Phys. 42 (2009).

27. N. Tateiwa, Y. Haga, Rev. Sci. Instrum., 80, 12 – 123901 (2009).

28. G. J. Piermarini, S. Block, J. D. Barnett, Jour. Appl. Phys., 44, 12 – 5377 (1973).

29. A. Jayaraman, Rev. Mod. Phys. 55, 1-65 (1983).

30. I. Fujishiro, G.J. Piermarini, S.Block, R. G. Munro, Proc. 8th AIRAPT Conf. (Uppsala 1982) vol II, 608 (1982).

31. J. Zhao, N. L. Ross, J. Phys.: Condens. Matter, 27, 18 - 185402 (2015).

32. T. Deschamps et al., J. Non-Cryst.Solids 355, 2422 (2012).

33. D. H. Liebenberg, Phys. Lett. A 73, 1 -74 (1979).

Chapter 5

RESULTS AND DISCUSSIONS

The study discussed in this thesis proposes to clarify unsolved questions about the anomalous behaviour of structure and dynamics in glass systems. In particular, its main goal is understand the nature of the low frequency modes contributing to the Boson Peak and the origin of the structural features contributing to the First sharp diffraction peak, and verify if a correlation between the specific structure of glasses in the mesoscopic length scale and their vibrational dynamics does exist.

In order to get a deep insight into these relevant issues, several experimental investigations have been performed including:

- *neutron diffraction measurements*
- *Raman scattering measurements*
- *inelastic neutron scattering measurements*
- *low temperature specific heat measurements*

Alkaline borate glasses $(M_2O)_x(B_2O_3)_{1-x}$, with M=Li, Na, K, Cs ions, permanently densified B_2O_3 glasses and an α-quartz have been investigated.

We chose these samples as model systems because their macroscopic physical and chemical properties have been studied for a long time and are widely known.

Most importantly, the composition of alkaline borate glasses can be changed in a wide range, whereas the vitreous B_2O_3 can be easily hydrostatically pressurized. These features made them interesting systems for the scopes of the present study.

5.1. Origin of Medium range order in alkaline borate glasses

In this section, the issue of the origin of the FSDP in glasses will be examined by studying the compositional dependence of the low-Q features of S(Q) in a series of alkaline borate glasses, here chosen as model of network-modifying glasses.

As widely depicted in Chapter 3, the structure of boron oxide consists of a network of planar BO_3 triangles, three out of four being grouped together to form planar B_3O_6 boroxol rings or rings of larger sizes (1). The addition of an alkali oxide determines the change of the boron coordination number from three to four, favoring the conversion of some BO_3 basic units into negatively charged BO_4^- tetrahedra and the consequent partial transformation of boroxol rings into larger superstructural units, containing at least one tetrahedra. The alkalis enter the network as singly charged

cations, occupying interstitial voids and they are loosely connected to BO_4^- or to non-bridging oxygens in order to preserve electric neutrality of the network.

The inclusion of a metallic oxide produces voids with different size and gives rise to a progressive expansion of the network. Because of its stronger bond ionicity, the size of the first coordination sphere of the Li ion with respect to oxygen is smaller than that of other alkali ions. In fact, a coordination number of 4 is found for Li, 5 for Na, 6 for K, and 7 for Cs.

As a consequence, it is foreseen that the sizes of the borate sites hosting the metallic cations differ significantly: ever larger voids should form if alkaline ions of increasing radius are included in the borate skeleton.

An indirect indication about the variation of the interstitial void size, occurring by changing the cations, can be obtained by the evaluation of the number density of boron atoms $N_{at} = 2(1-x)\frac{\rho N_A}{P_M}$, where ρ is the mass density, P_M the molar mass and N_A the Avogadro's constant.

N_{at} is shown in Figure 1 as a function of x for the investigated alkaline borate glasses.

It is possible to observe that, except for the lithium glasses, by increasing the alkali content, the atomic density decreases, indicating a progressive expansion of the network and a decreasing packing.

Moreover, at a fixed concentration the number density decreases by going from lithium to cesium showing a greater efficiency in expanding the network for modifiers having a larger ionic radius.

These data are confirmed by experimental thermal expansion measurements, shown in Figure 2 for glasses with x = 0.14, that give evidence for a dilatation coefficient that increases with the ionic radius over an extended temperature range.

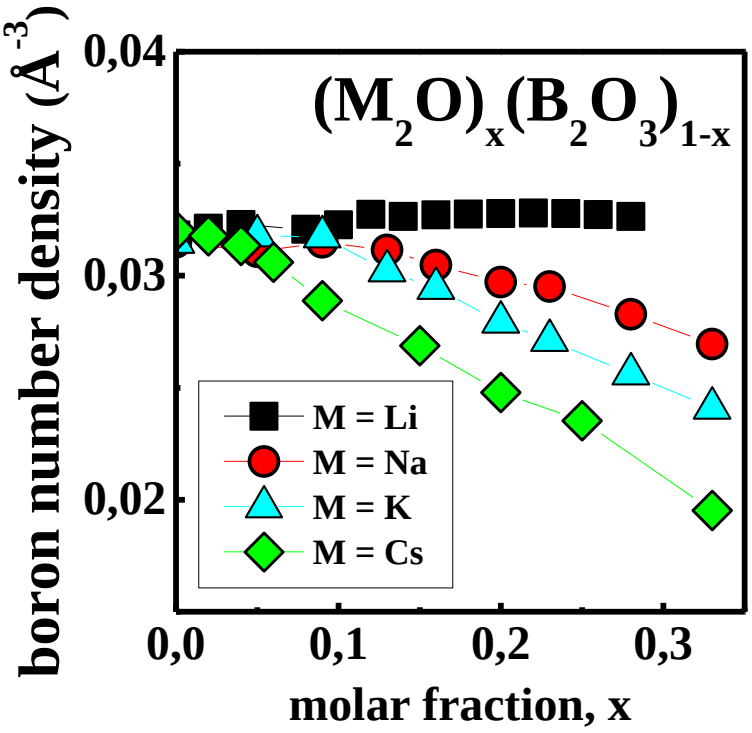

Figure 1. Boron number density as a function of molar fraction x for $(M_2O)_x(B_2O_3)_{1-x}$.

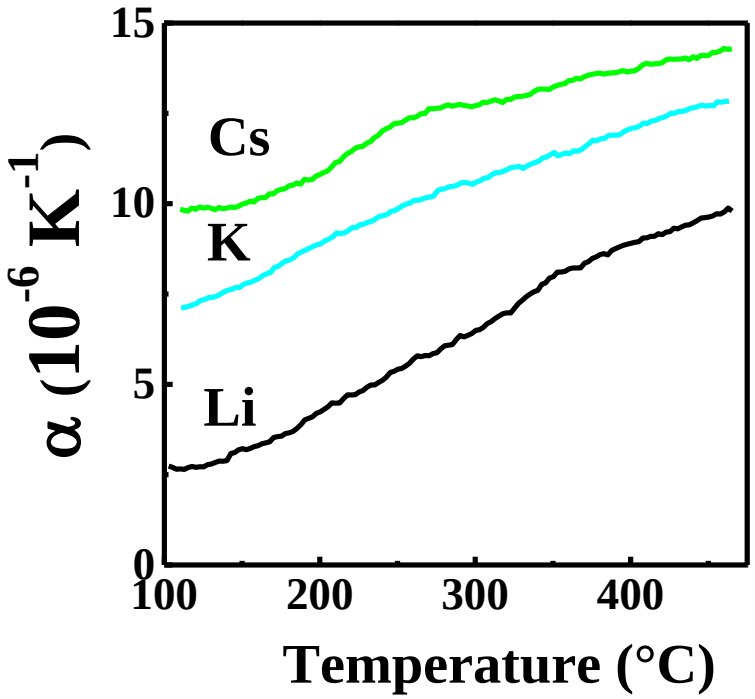

Figure 2. Temperature dependence of the linear expansion coefficient of $(M_2O)_{0.14}(B_2O_3)_{0.86}$.

In order to estimate the size of interstitial void hosting the alkaline cations M, a model is proposed in which the voids hosting the alkaline cations have been represented as spheres, whose planar projections are cyclic regular polygons, having side length s (B-O distance) and 2n vertices, where n is the coordination number of M (4 for Li, 5 for Na, 6 for K and 7 for Cs). Therefore the radius of circumcircle of such polygons can be evaluated as

$$R_{theo} = \frac{s}{2\sin\frac{\pi}{n}} \qquad \textbf{(1)}$$

It's important to note that, whatever is the structural units on which the borate skeleton is built on (triangles BO_3, tetrahedra BO_4 or other superstructural units), the contour of the planar projections of a void is always an n-membered ring formed by a sequence of B-O segments.

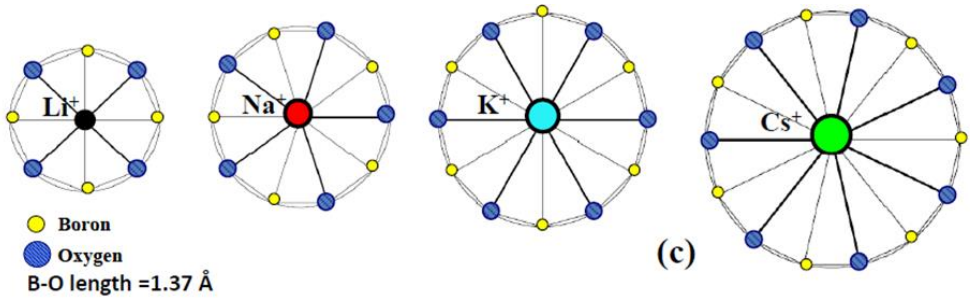

Figure 3. *Polygons schematically representing the two-dimensional (2D) section of spherical voids hosting M cations . The B-O average bond length was fixed at 1.37* Å **(2)**. *This description provides only an approximate sketch of the real shape of the structural voids in glasses that is rather irregular and asymmetric.*

Figure 3 shows the polygons representing the 2D section of the voids hosting the different M cations. The estimated void diameters range from 4 to 6 Å , going from Li to Cs, thus indicating the formation of structures in the intermediate scale whose fingerprints in the diffraction spectra are localized below Q = 2 $Å^{-1}$.

In order to explore the MRO region of the alkaline borate glasses, two sets of neutron diffraction experiments have been performed, that separately probe the influence of the size and of the concentration of the metallic cations:

- in the first set of measurements the network composition was kept constant, while the size of the modifier was changed.

- in the second set of measurements, the network composition was changed, while the size of the modifier was kept constant.

Although the total structure factor S(Q) looks similar for all samples at high Q values, the low Q range (Q < 2.5 $Å^{-1}$) strongly depends on the type and content of alkaline cation incorporated into the glassy network.

The neutron diffraction patterns of $(M_2O)_x(B_2O_3)_{1-x}$ glasses at fixed concentration x = 0.14 are shown in Figure 4.

The presence of two peaks P_{k1} and P_{k2}, respectively below and above the position of the first peak in the diffraction pattern of pure B_2O_3 glass (2) (Q=1.61 $Å^{-1}$), is observed in all the investigated samples, except for lithium glasses. It is in agreement with previous neutron diffraction results on germanate glasses which showed the appearance of a pre-peak in the static structure factor after the addition of the rubidium oxide (3).

The P_{k1} and P_{k2} position and intensity appear strongly affected by the size of the metallic cation. Particularly, the position of P_{k1} decreases linearly with increasing the size of the metallic cation (Figure 5).

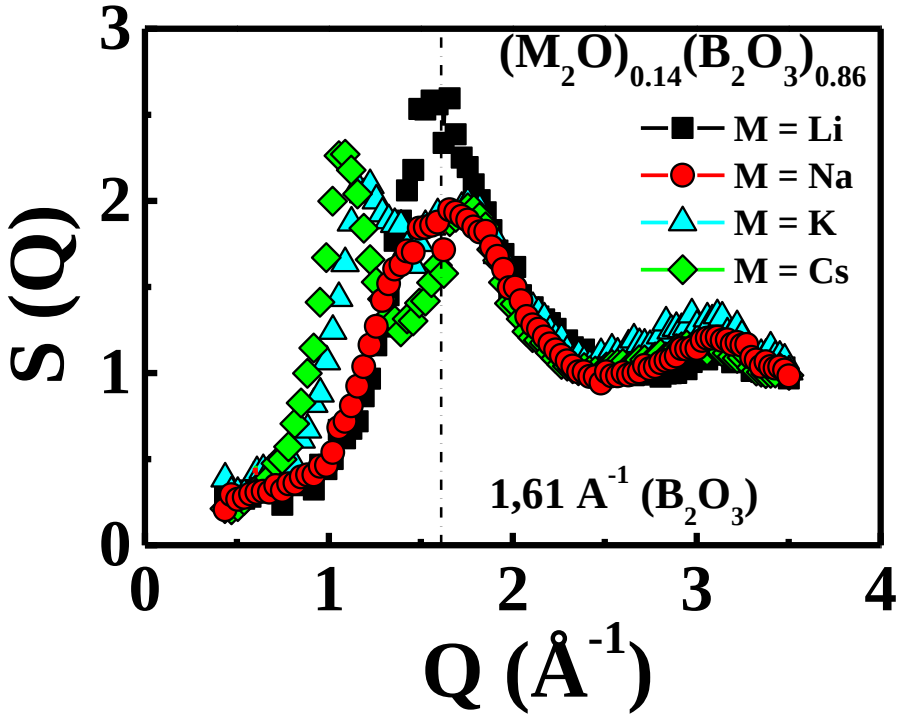

Figure 4. Structure Factor S(q) for $(M_2O)_x(B_2O_3)_{1-x}$ glasses with a different M cation at fixed x=0.14 obtained by TOF Neutron Diffraction Measurements on D1B diffractometer at ILL in Grenoble with λ=2.52Å

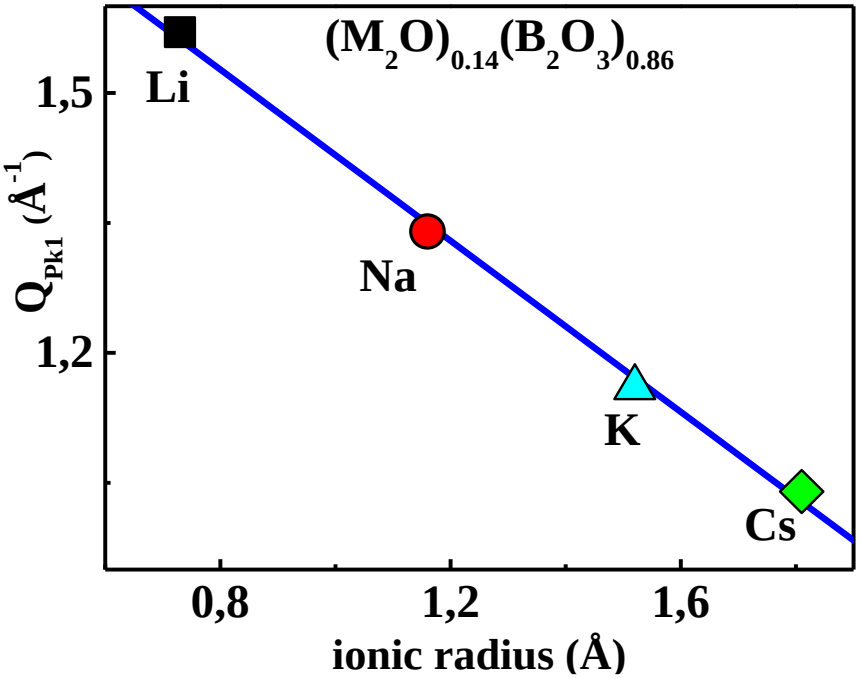

Figure 5. Experimental P_{k1} positions as a function of ionic radius.

Further interesting details about P_{k1} are revealed by the data shown in Figures 6, 7 and 8, where the S(Q) of lithium, sodium and caesium borate glasses at different compositions are compared.

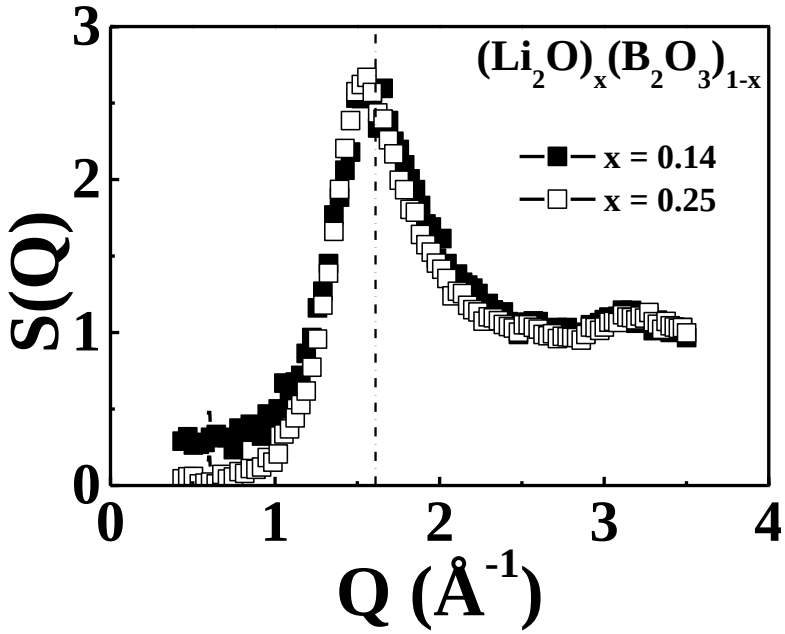

Figure 6. Structure Factor S(Q) at different x in$(Li_2O)_x(B_2O_3)_{1-x}$. The vertical dashed line indicates the position of the FSDP ($Q=1.61$ Å^{-1}) in B_2O_3 glass **(2)**.

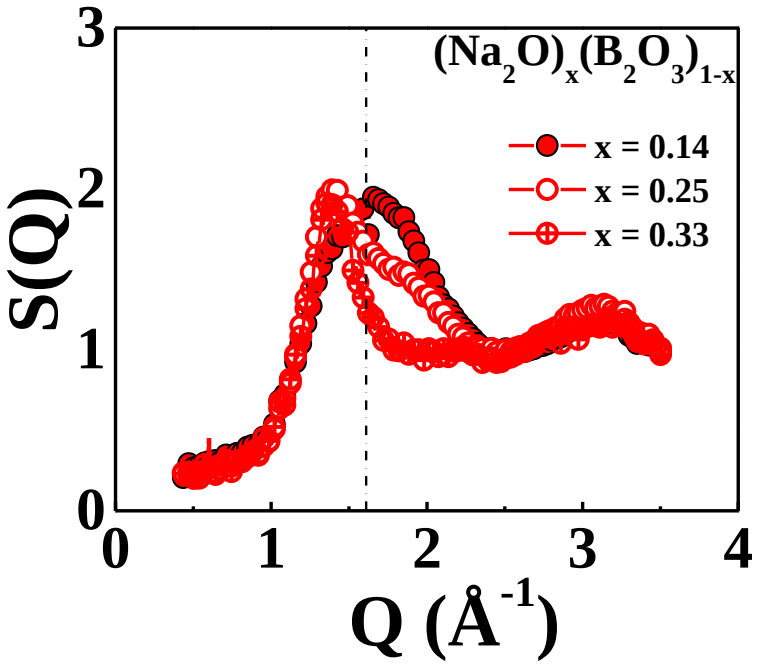

Figure 7. Structure Factor S(Q) at different x in$(Na_2O)_x(B_2O_3)_{1-x}$.

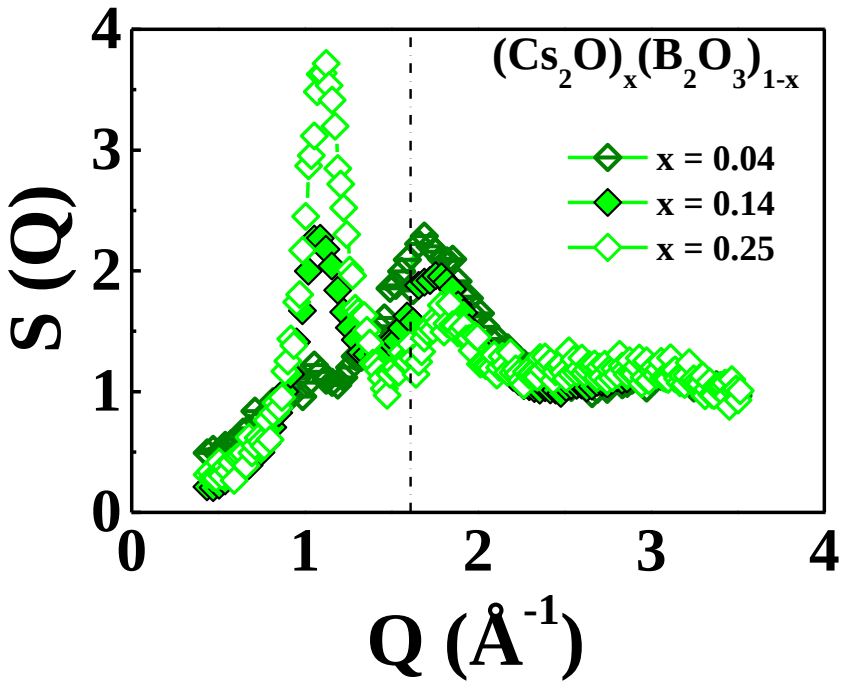

Figure 8. Structure Factor S(Q) at different x in $(Cs_2O)_x(B_2O_3)_{1-x}$.

On the basis of experimental evidences, the P_{k2} is ascribed to the correlations arising from structural voids resulting from the arrangements of BO_3 or B_3O_6 units present in the boron matrix. Conversely, the P_{k1} is attributed to the correlations arising from rings of wider size originating from the structural modifications following the introduction of the alkaline oxide.

This description supplies a simple understanding of the observed behavior: by increasing the concentration of sodium or caesium oxide, the P_{k1} intensity increases owing to a higher number of voids of great dimension that are formed; whereas the P_{k2} intensity decreases as a consequence of the reduction of voids present in the cation-free borate skeleton (Figures 7 and 8). Conversely, the single peak observed in lithium glasses (Figure 6), keeps his feature almost unchanged, even for high concentrations of Li_2O. Therefore, in analogy with the previous observations, the size of the voids

formed by the inclusion of lithium oxide keeps similar to that of voids present in the cation-free borate region, in agreement with the invariance of the number density (*Figure 1*).

The variations in the position and number of the low-Q features in the structure factor data demonstrate that the presence of alkali metallic cations changes dramatically the medium-range order, while it does not influence the short-range order.

In order to analyze in detail the revealed peaks, the diffraction curves were fitted with three Gaussian functions, which yielded the peaks' position, width and area. The results of fits for lithium, sodium and caesium glasses with x = 0.25 are plotted in Figures 9, 10 and 11, respectively, while the fitting parameters Q_i and A_i, indicating the position and the area of each peak, are reported in Table 1.

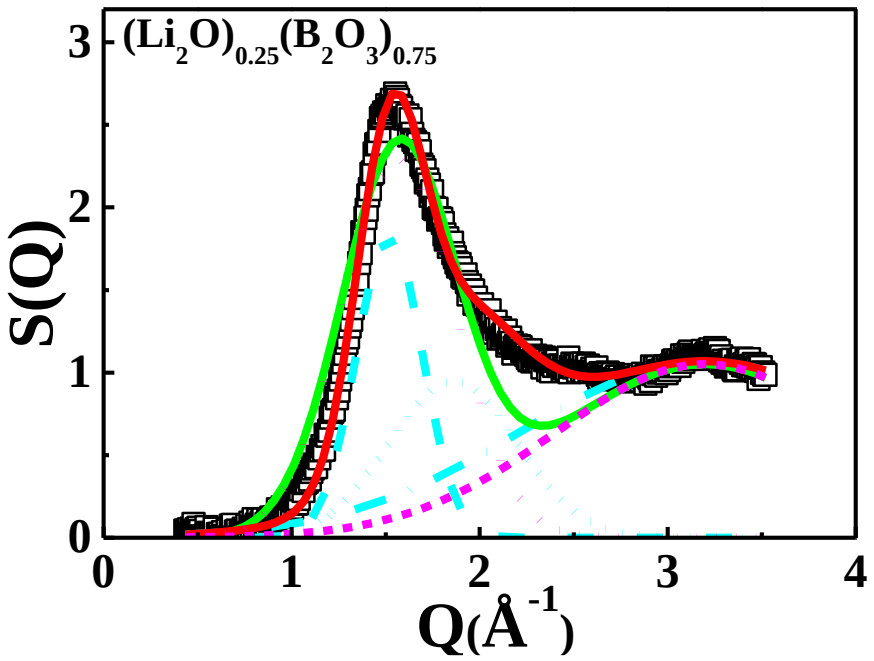

Figure 9. Structure factors of $(Li_2O)_{0.25}$ $(B_2O_3)_{0.75}$ glasses with three-Gaussian fits (red line). A two-Gaussian fit is also shown for comparison (green solid line).

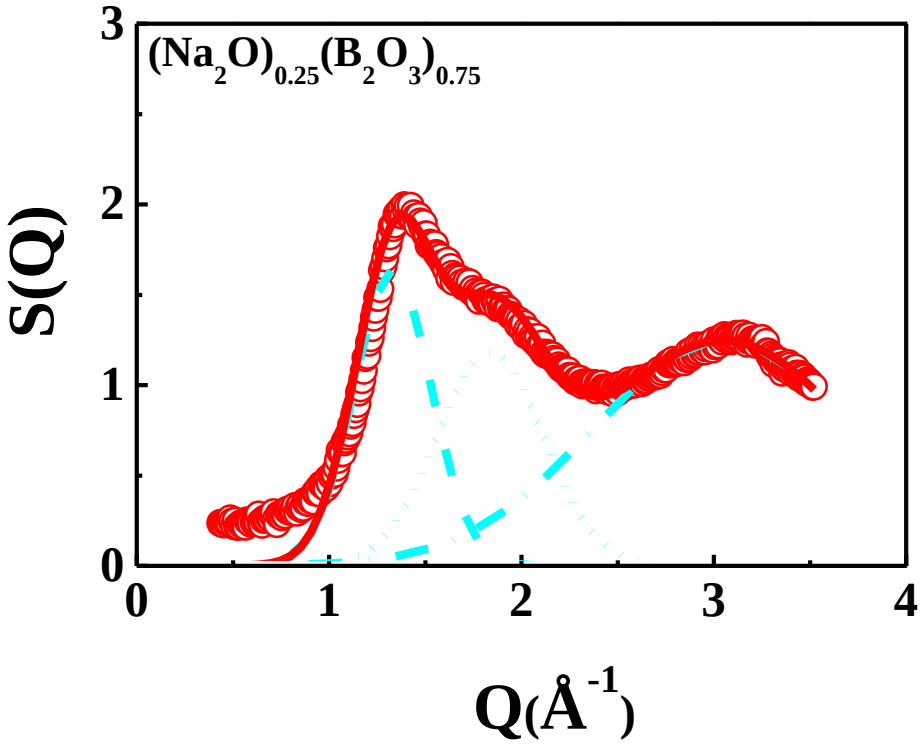

Figure 10. Structure factors of $(Na_2O)_{0.25}$ $(B_2O_3)_{0.75}$ glasses with three-Gaussian fits (red line).

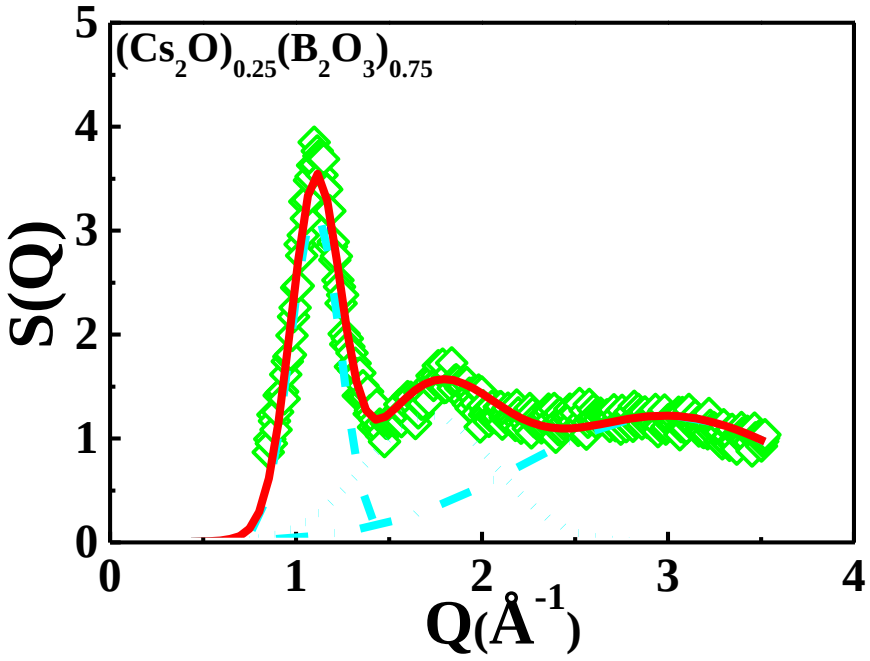

Figure 11. Structure factors of $(Cs_2O)_{0.25}$ $(B_2O_3)_{0.75}$ glasses with three-Gaussian fits (red line).

SAMPLE		Q_1 ($Å^{-1}$)	A_1	Q_2 ($Å^{-1}$)	A_2	Q_3 ($Å^{-1}$)	A_3
$(Li_2O)_x(B_2O_3)_{1-x}$	x=0.14	1.57	0.45	1.62	1.19	3.02	2.75
	x=0.25	1.52	0.81	1.86	0.81	3.20	2.60
$(Na_2O)_x(B_2O_3)_{1-x}$	x=0.14	1.33	0.47	1.67	1.04	3.10	2.71
	x=0.25	1.33	0.82	1.84	0.82	3.05	2.11
	x=0.33	1.35	0.95	1.99	0.55	3.19	2.12
$(K_2O)_x(B_2O_3)_{1-x}$	x=0.14	1.16	0.60	1.68	1.45	3.05	2.44
$(Cs_2O)_x(B_2O_3)_{1-x}$	x=0.04	0.95	0.25	1.66	1.87	3.03	1.95
	x=0.14	1.05	0.68	1.71	1.36	3.05	2.11
	x=0.25	1.10	1.06	1.72	1.07	2.99	2.38

Table1. Fit parameters for all the investigated alkaline borate glasses.

Interestingly also in lithium samples two Gaussian profiles, with very close Qi, were necessary to reproduce the apparently single peak observed in the S(Q) below Q = 2 $Å^{-1}$ (*Figure 9*).

Concerning the peak located at Q > 2.5 $Å^{-1}$, for all the investigated alkaline borate glasses, no relevant changes for the position Q_3 and the area A_3 are observed. This result confirms that, on this length scale, the structure of these systems is based on the same structural units and is not influenced by the presence of the specific metallic cation neither by its concentration.

We ascribe the values of the repetitive characteristic distance L_1 ($L_1 = 2\pi/Q_1$, associated to P_{k1}) to the diameter 2r of the voids hosting the M^+ cations and the length L_2 ($L_2 = 2\pi/Q_2$, associated to P_{k2}) to the diameter of the empty voids in the borate skeleton. Note that the values of the repetitive characteristic distance L_i closely correspond to the diameter $2R_{theo}$ of the voids hosting the M^+ cations (Table 1). The Q_1 and Q_2 values, together with the circular perimeter ($=2\pi^2/Q_i$) of the rings, at x = 0.14, are plotted as a function of the ionic radius of M^+ in Figure 12 and Figure 13, respectively.

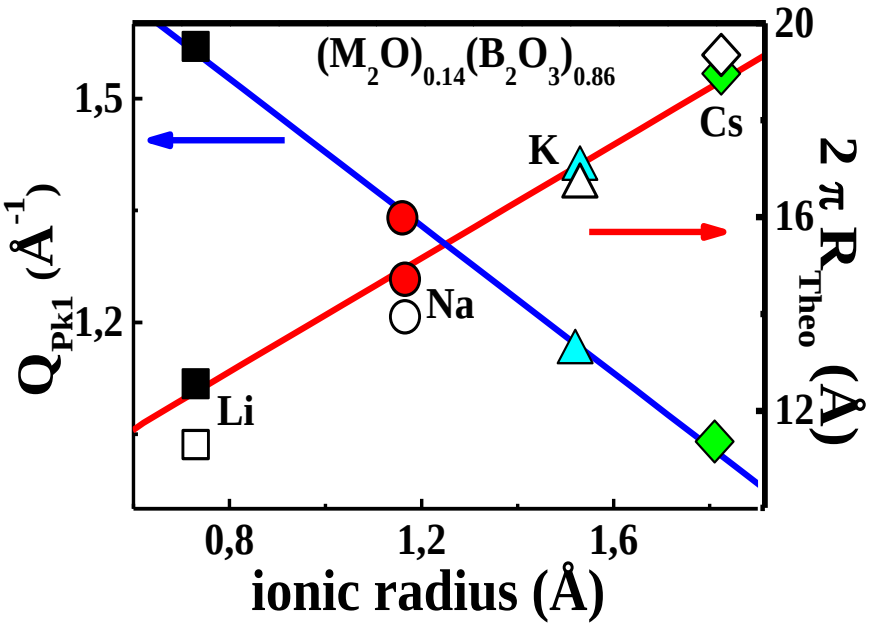

Figure 12. *The Q-position of P_{k1} and experimental (full symbols) and theoretical (empty symbols) void length vs ionic radius* at x=0.14.

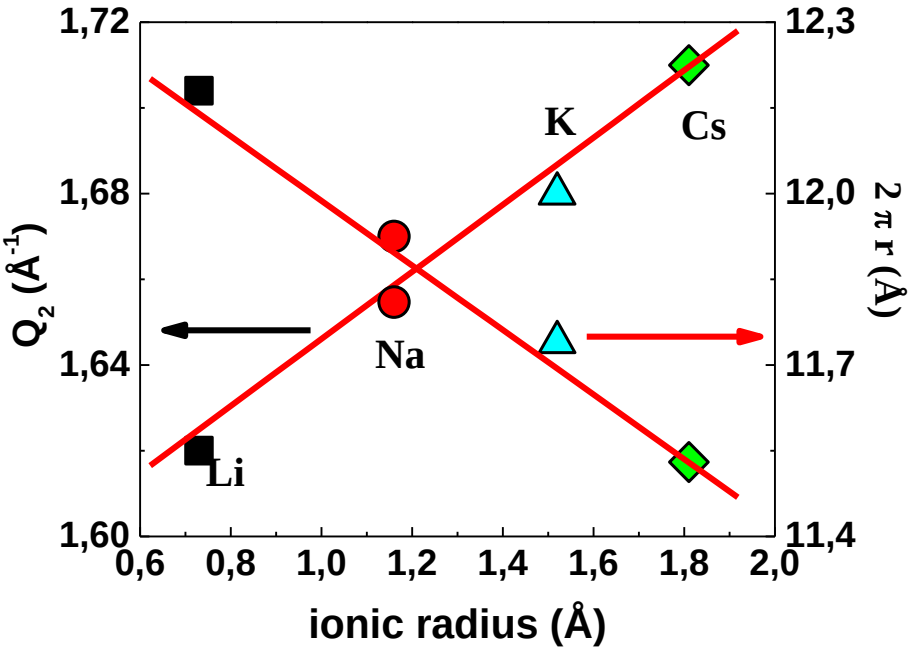

Figure 13. The Q-position of P_{k2} and experimental void length vs ionic radius at x=0.14.

Increasing the ionic radius from lithium to caesium, Q_1 linearly decreases, giving evidence for rings of increasing size, while an opposite behavior has been found for the position of the second peak, Q_2.

As a matter of fact, the network modifying ions (NMI) alter their local environment as a function of their ionic radius and the minimum size of the void hosting the alkaline cation increases by going from lithium to caesium borate glasses as a consequence of the decreasing bond field strength between the metallic cations and the surrounding network.

At the same time, the enlargement of filled voids could produce the shrinkage of empty voids according to the increase of Q_2 value. This effect would become more evident with the increase of the NMI content as a consequence of a greater number of filled voids, in agreement with *Figure 14*, where Q_2 as a function of the molar fraction is reported.

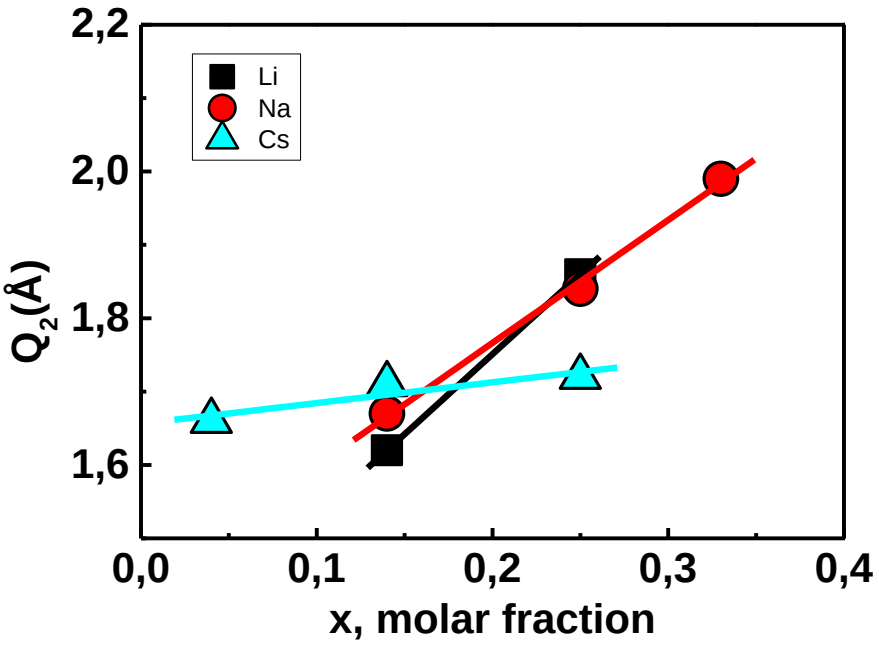

Figure 14. The Q_2 position as a function of the metal oxide molar fraction. The lines are just guides for the eyes.

Furthermore, at low concentrations up to x = 0.14, an increase of the P_{k2} position by going from lithium to caesium system is observed.

This finding would suggest that the corresponding decrease of empty void size is more evident for alkaline ions with increasing ionic radius since they need more space to be incorporated into the borate network. Conversely, at concentration higher than x = 0.14, an inversion in the Q_2 trend as a function of the alkaline ionic radius is revealed.

This experimental evidence could be explained considering that at this higher concentrations NBOs are created in the borate network and that the formation of these non-bridging atoms is favoured as the alkali ion size increases (4). This process contrasts to the formation of BO_4^- and, thus, a decreasing number of superstructural units are created by going from lithium to caesium borate glasses. These structural units occupy large volumes plausibly obtained at the expense of the unfilled voids whose size, thus, is expected to decrease with the alkaline ionic radius.

Furthermore, assuming that the area under P_{k1} and P_{k2} is proportional to the amount of nanovoids in the borate network, we have calculated the fraction of filled N_{Pk1} and empty N_{Pk2} voids according to

$$N_{PK1} = \frac{A_{PK1}}{A_{PK1} + A_{PK2}} \tag{2}$$

$$N_{PK2} = \frac{A_{PK2}}{A_{PK1} + A_{PK2}} \tag{3}$$

where A_{Pk1} and A_{Pk2} are the area of Pk_1 and Pk_2 respectively.

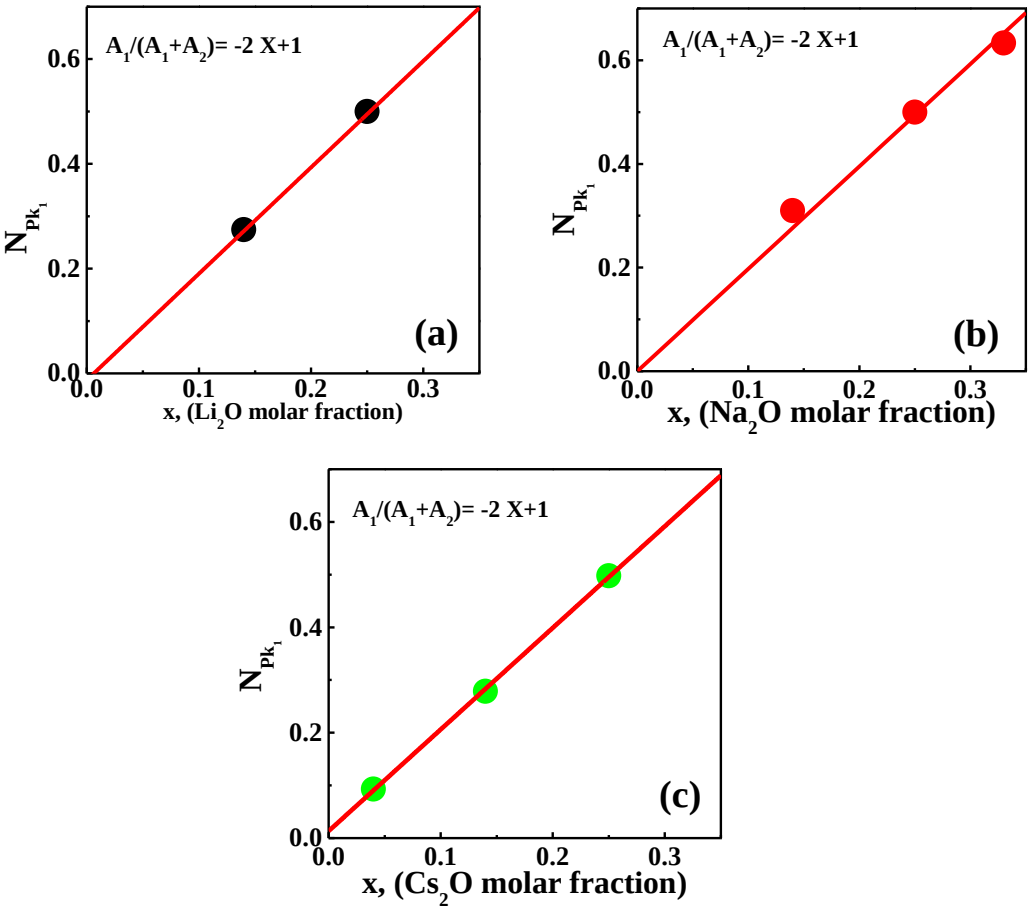

Figure 15. The fraction of larger rings NPk1 as a function of x: a) M = Li, b) M = Na, c) M = Cs.

Very importantly, a plot of $N_{Pk1,}$ as a function of the cation molar fraction, x, yields a straight line of gradient 2 (Figure 15), while a plot of N_{Pk2} vs the cation molar fraction shows a trend described by a (1−2x) dependence on x (*Figure 16*). Both these two evidences indicate that two larger voids instead of two smaller ones are formed as a consequence of the addition of a single molecule of alkaline oxide, as predicted by structural considerations.

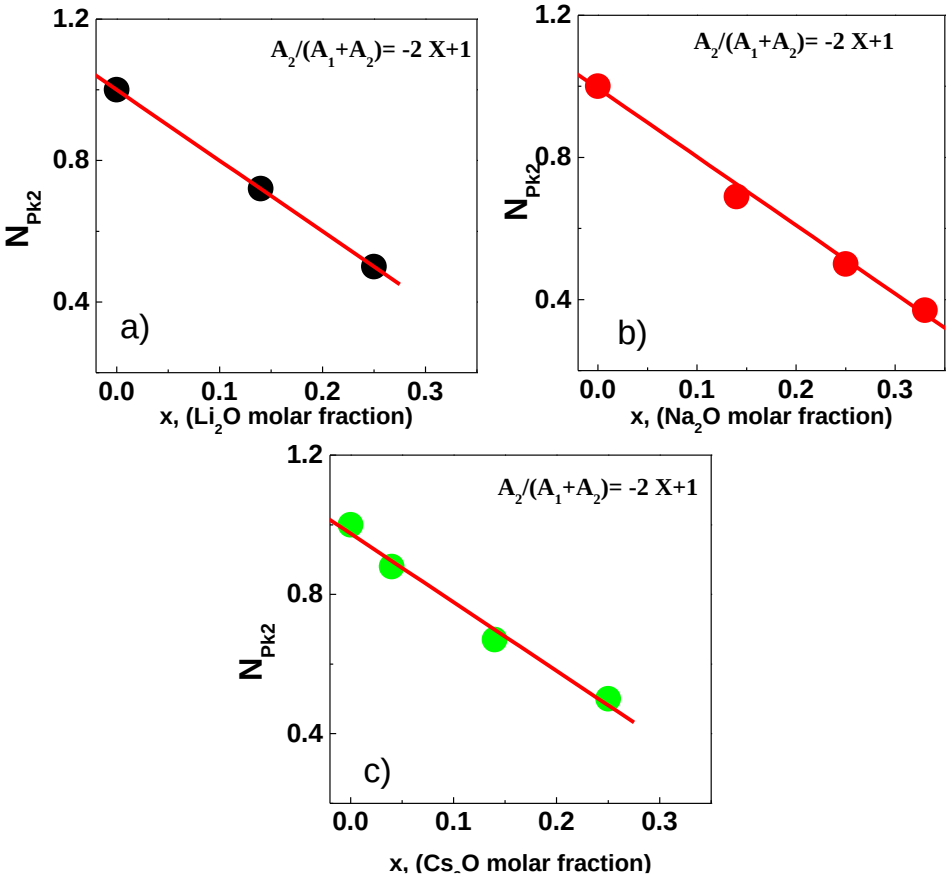

Figure 16. The fraction of smaller rings N_{Pk2} as a function of x: a) M = Li, (b) M = Na, c) M = Cs.

In the following, some remarks on the width of the FSDP in glasses are presented. According to literature (5; 6), this width is believed to reflect a characteristic correlation distance on the medium-range length scale. In this regard, a different interpretation has come out from a recent study (7), where the diffraction patterns of glassy, thermal-treated and crystalline caesium borate samples have been compared, showing that the pre-peak and the FSDP revealed for the glass can be considered as the broadened envelopes of the corresponding peaks of crystalline phase.

According to these experimental evidences and in agreement with the here proposed void-based origin of the FSDP, it can be hypothesized that, whereas the crystal exhibits symmetric voids of a specific size, causing the appearance of distinct sharp peaks, the glass is characterized by a distribution of void sizes. In glasses, these voids have asymmetric shapes and their mean size corresponds to the Q-position at the maximum of the single broadened peak in the S(Q).

Note that, in glasses, the voids have an asymmetric shape due to the structural arrest taking place during glass formation.

This process would attenuate the higher structural order related to the most intense peak in the diffraction pattern of the corresponding crystal, keeping and exalting other possible structural orders.

All of these considerations can be further extended to other glasses, where basic structural units building the glassy network form n-membered rings. We remark that these rings in the here considered framework represent the planar section of voids.

In *Figure **17***, we report the experimental S(Q) of SiO_2 (6), GeO_2 (8), lithium and potassium borate glasses together with the diffraction patterns of related crystalline systems obtained from the Inorganic Crystal Structure Database.

It is important to note that, in comparing glasses and crystals, just one crystalline phase has been considered, but, as previously observed for caesium borate glasses (7), it cannot be excluded that the diffraction patterns of the glassy systems can show similarities to more crystalline phases.

Clearly, in Figure 17, it can observed that the amorphous nature of glasses leads to the disappearance or the smearing of some Bragg peaks from the diffraction pattern and the appearance of diffuse scattering haloes.

Indeed, in the same Q region where these glasses show the presence of the FSDP (and of a pre-peak in the case of modified borate glasses), crystals show well-defined features. This comparison would suggest that the FSDP width, far from being related to a structural correlation length, could be

instead the result of the overlapping of several broadened peaks: the position and width of each peak being related to the size and to the irregular shape of a void, respectively.

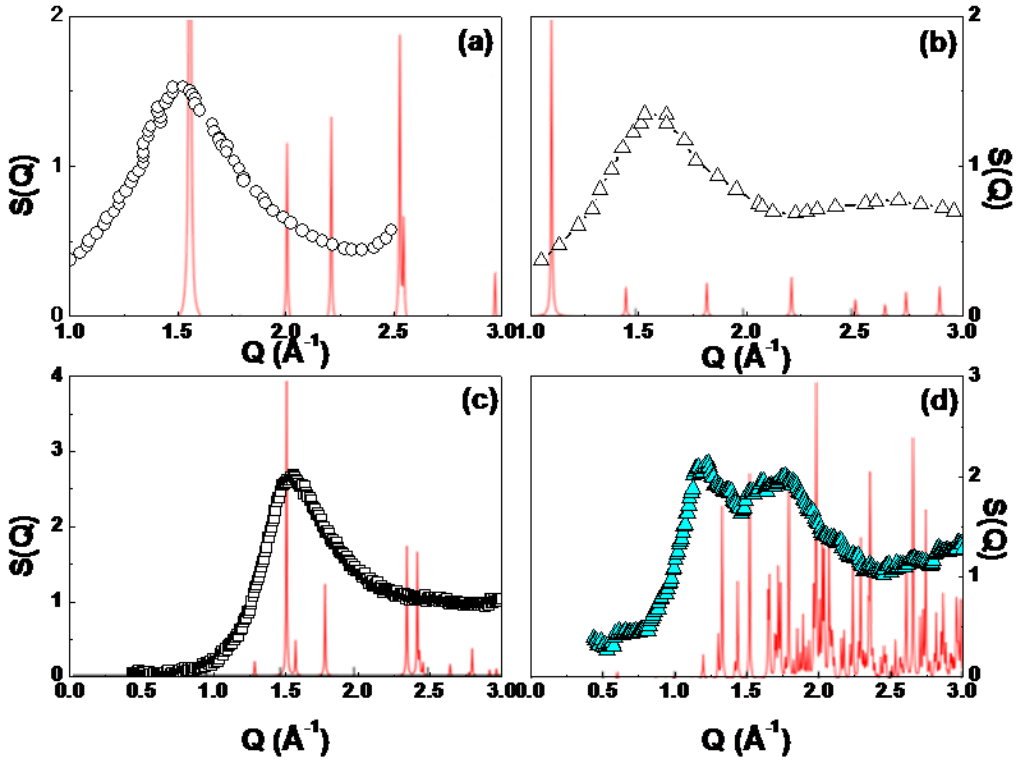

Figure 17. Diffraction patterns of: a) SiO_2 glass (circles) and α-cristobalite (solid line); b) GeO_2 glass (triangles) and rutile (solid line); c) $(Li_2O)_{0.25}(B_2O_3)_{0.75}$ glass (squares) and $Li_2B_4O_7$ crystal (solid line); d) $(K_2O)_{0.14}(B_2O_3)_{0.86}$ glass (triangles) and KB_3O_5 crystal (solid line).

Finally, it can be argued that the actual explanation of the origin of the FSDP can provide a general rationale for all the anomalous behaviors observed for this peak in glasses: temperature, pressure and compositional dependence.

Indeed, the anomalous temperature dependence of the FSDP can be ascribed to stronger correlations between the network forming ions (NFI) and oxygen atoms delimiting the voids. Temperature favours the relaxation of strained bonding in the n-membered rings, leading to a more regular (spherical) shape of voids. This describes the natural tendency of a glass towards the typical ordering of the crystalline state. In particular, in modified glasses, it can be predicted that relaxations are more substantial within large stuffed voids compared with those of small unoccupied voids. Stuffed voids in fact yield strain on the network to provide a favorable environment for the NMIs (more constrained hosting voids). With increasing temperature, this environment is strongly altered because the voids are expanded and the cations become highly mobile. As a consequence, the alkali bonding constraints are relieved, leading to relaxed B–O–B bond angles and reinforced O–O and B–O correlations within the boundaries and thus to a sharper increase of the intensity of the related FSDP (7).

5.2 Estimation of void radius in tetrahedral glasses

In this section, in order to verify the validity of the structural model here proposed, we applied it to a series of tetrahedral glasses: SiO_2, GeO_2, $GeSe_2$. For these systems the theoretical void radius R_{theo} has been estimated by calculating the radius of the incircle of a polygon having a side *l* equal to the side of the tetrahedral structural unit (*Figure 18*).

In this way, it has been taken into account the steric hindrance of the tetrahedral units overlooking a void. Note that the planar section of the void is formed by an n-membered ring with all-side vertex sharing tetrahedral. Thus, the number *n* of sides of the polygon for the considered systems has been

established by considering the information on the distribution of ring structures, available in literature: SiO_2 shows a prevailing contribution of six-folded rings (9), GeO_2 of four-folded (10) and six-folded (11) rings, $GeSe_2$ of four-folded, five-folded, and six-folded rings (12).

In details, for GeO_2 the void radius has been determined as the average value between the theoretical radii R_{theo} of the incircles of a square and of an hexagon, for $GeSe_2$, instead, the void radius has been determined as average of the three R_{theo} of the incircles of a square, a pentagon, and an hexagon.

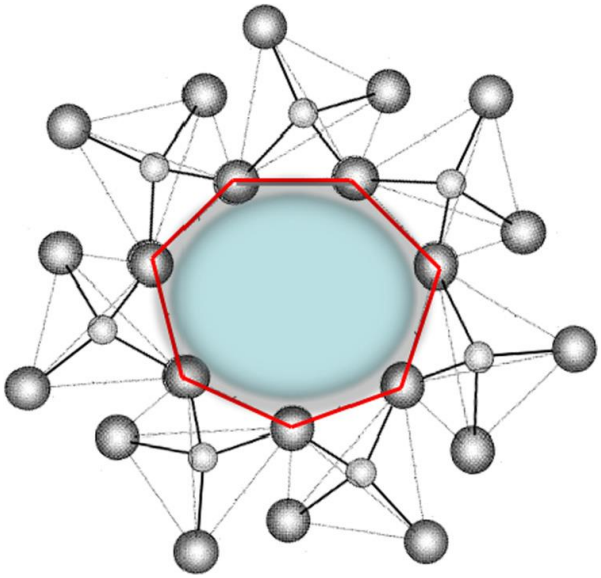

Figure 18. Model of the planar section of a void delimited by tetrahedral units. The red segments represent the polygon circumscribable to the void having the anion-anion distances as sides.

The model for the FSDP origin here described can provide also an easy explanation for the ubiquitous anomalous pressure dependence of FSDP: indeed, the observed shift to higher Q values and the decrease in intensity can be explained, respectively, as due to the decrease of the size and of the number of the interstitial voids that occur if an increasing pressure or densification is applied to glass.

The reduction of the R_{theo} in a glass subjected to external pressure or densified can be evaluated by simple geometric considerations.

Indeed, the diminuition of the molar volume ΔV, related to the increase of the density, is ascribable to a reduction of void size (this assertion is true if the application of pressures does not produce changes of the coordination number or bond length in the tetrahedral structural unit). Thus, by considering the same number of voids in normal and densified systems, ΔV can be calculated by the following expression:

$$\Delta V = V_n - V_d = \frac{M_\omega(\rho_d - \rho_n)}{\rho_d \rho_n} = V_n^{voids} - V_d^{voids} = \frac{4}{3}\pi(R_n^3 - R_d^3)N_{voids} \quad (4)$$

where M_w is the molecular weight, V and ρ are the volume and the density, V_{voids} is the empty volume among the structural units distributed as a number N_{voids} of spherical voids of radius R and the subscripts *n* and *d* refer to the normal and densified glass, respectively.

The number of voids can be quantified in the normal system by calculating V_{voids} and dividing this value to the volume of a single void, $4\pi R^3/3$, where $R=\pi/Q_{FSDP}$.

Furthermore, considering that the network of a mole of tetrahedral glass is based on a number $N_A/3$ (where N_A is the Avogadro constant) of tetrahedral structural units of mass M and side *l*, each one having a volume $V = \frac{\sqrt{2}}{12} l^3$, we calculated V_{voids} as the difference of the total volume of the solid V_n and the volume of tetrahedral structures: $V^{voids} = V_n - \frac{N_a}{3} V$.

Finally, the theoretical void radius R_d of densified system, will be defined as

$$R_d = \sqrt[3]{R_n^3 - \frac{3}{4\pi} \cdot \frac{M_\omega}{N_{voids}} \cdot \frac{\rho_d - \rho_n}{\rho_d \rho_n}} \quad \textbf{(5)}$$

The R_{Theo} values determined for densified glasses are reported in Figure 19 as a function of R_{exp}, inferred by the corresponding Q position of the experimental first peak appearing in the structure factor S(Q).

The theoretical radius for two different amorphous H_2O phases, the low density (LDA) and the high density (HDA), is also shown. To determine the

void radius for LDA and HDA systems, the same theoretical approach used for densified tetrahedral glasses has been applied. In particular, the liquid water has been considered as the normal not densified system, whose network is made of tetrahedral units based on four H_2O molecules, and whose FSDP is located at 2 $Å^{-1}$ (13).

The table 2 shows all the data used to determine the void radius for the analyzed systems. The very good agreement observed for this large number of systems strongly shows that the proposed approach, despite its extreme simplicity, can account for the major features of the FSDP in glasses.

SAMPLE	P (GPa)	ρ (g/cm^3)	l (Å)	Q_1 ($Å^{-1}$)	R_{exp} (Å)	R_{Theo} (Å)
$(Li_2O)_{0.14}(B_2O_3)_{0.86}$	ambient	2.0711	1.37 (d_{B-O})	1.57	2.00	1.79
$(Na_2O)_{0.14}(B_2O_3)_{0.86}$	ambient	2.122	1.37 (d_{B-O})	1.36	2.31	2.22
$(K_2O)_{0.14}(B_2O_3)_{0.86}$	ambient	2.088	1.37 (d_{B-O})	1.16	2.71	2.65
$(Cs_2O)_{0.14}(B_2O_3)_{0.86}$	ambient	2.484	1.37 (d_{B-O})	1.05	2.99	3.08
SiO_2 (14)	ambient	2.198	2.64 (d_{O-O})	1.5	2.093	2.286
	4	2.255		1.572	1.997	2.075
	6	2.406		1.63	1.926	2.030
	8	2.670		1.807	1.738	1.959
GeO_2 (15)	ambient	3.639	2.83 (d_{O-O})	1.575	1.994	1.932
	2	3.796		1.618	1.941	1.966
	3	4.041		1.719	1.827	1.924
	6	4.226		1.796	1.748	1.895
$GeSe_2$ (16)	ambient	4.262	3.89 (d_{Se-Se})	1.010	3.109	3.312
	3.9	5.384		1.102	2.849	2.865
	5.3	5.660		1.131	2.776	2.815
	9.3	6.488		1.225	2.563	2.682
Li_2O-$2SiO_2$ (17)	ambient	2.34	2.65 (d_{O-O})	1.699	1.848	-
	1	2.39		1.743	1.801	1.835
	3	2.49		1.803	1.741	1.810
	6	2.58		1.847	1.700	1.788
LDA	ambient	0.940	4.508	1.69	1.858	1.605
HDA	ambient	1.170	4.508	2.15	1.460	1.484

Table 2. Pressure (P), mass density (ρ), tetrahedral side (l), Q_1 position of the first peak in the diffraction pattern, experimental (R_{Exp}) and theoretical (R_{Theo}) void radius values.

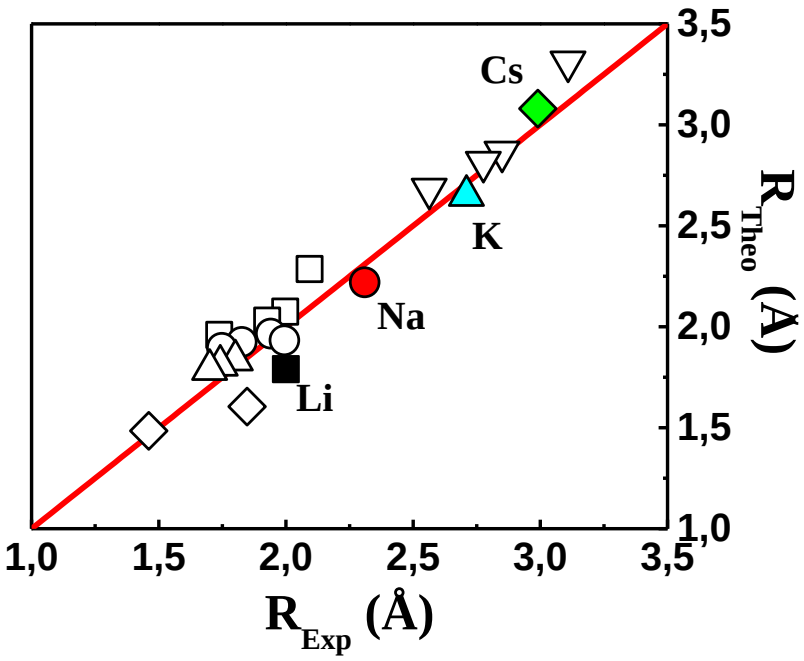

Figure 19. *R_{Theo} of densified SiO_2 (empty square* (14)*), GeO_2 (empty circle), $GeSe_2$ (empty down triangle), $(Li_2O)2(SiO_2)$ (empty up triangle), LDA and HDA (empty diamond) together with theoretical void radius (full circle) of alkaline glasses versus the experimental void radius, R_{Exp}. The solid line is a guide to the eyes.*

5.3 Pressure-induced structural transformation in B_2O_3 glasses

In order to study density-driven structural transformations in glass systems, a neutron diffraction investigation has been performed on densified B_2O_3 glasses at pressures increasing from ambient up to 4 GPa (Figure 20).

At ambient pressure, the neutron total structure factor S(q) shows an FSDP at a position $q_{FSDP}=1.58Å^{-1}$.

As the pressure is increased, a reduction in height of the FSDP and an almost linear increase of its position Q_{FSDP} are observed (Figure 21).

Appreciable differences in the structure factors S(q) of the different systems are noticeable. However, the diffractograms of 4GPa/B4 sample and the less dense 4-GPa/B3 glass show strong similarities.

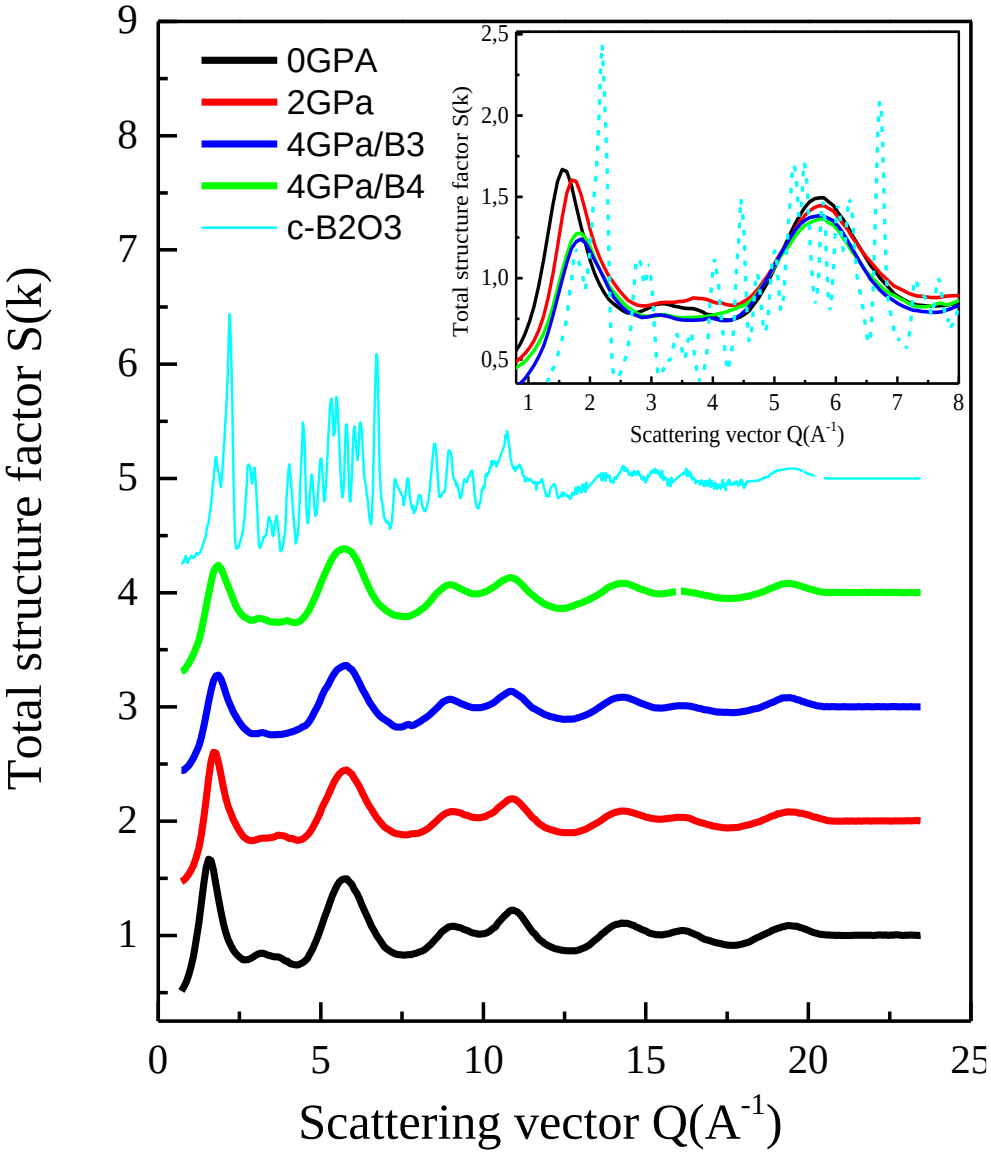

Figure 20. The neutron total structure factor S(q) of densified B_2O_3 glasses, as measured using the D4 diffractometer. The spectra are normalized to the high Q-peak, which is supposed the same for all the systems.The high-pressure data sets have been shifted vertically for clarity of presentation. In the inset, a zoom of low Q-region is shown.

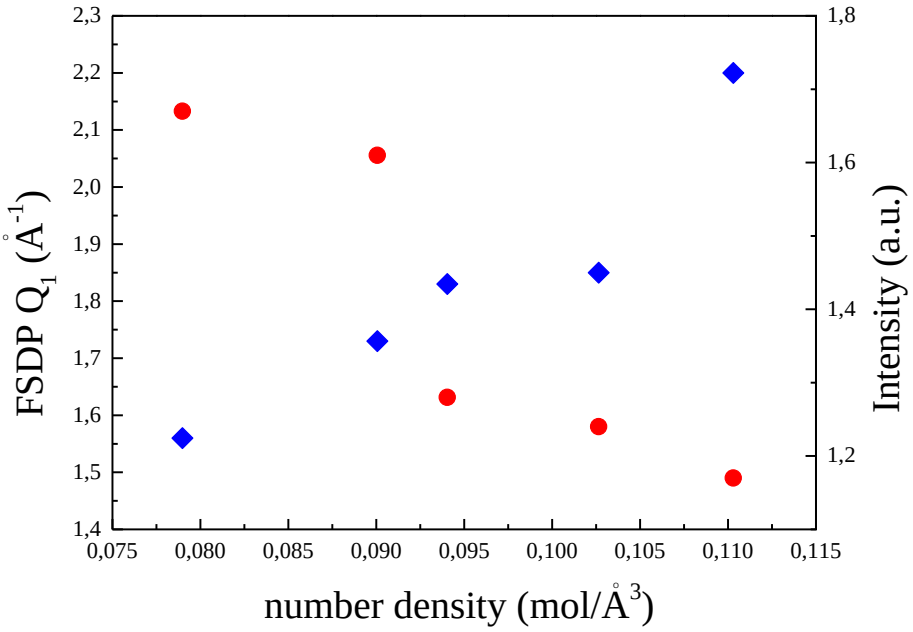

Figure 21. The position (blue diamonds) and the amplitude (red circles) of the FSDP as a function of the number density.

The corresponding real-space information which accounts for the local density fluctuations are included in the total pair-distribution function g(r), which has been obtained by performing the Fourier transform relation from S(q) (Figure 22):

$$g(r) = 1 + \frac{1}{2\pi^2 \rho r} \int_0^\infty [S(q) - 1] M(q) q \sin(qr) dq \qquad \textbf{(6)}$$

where ρ is the atomic number density of the glass and M(q) is the Lorch modification function (18), defined by $M(q) = \frac{\sin(q\pi / q_{max})}{q\pi / q_{max}}$ for $0 \leq q \leq q_{max}$ and M(q)=0 for $q > q_{max}$. The Lorch function is introduced in order to reduce the severity of the Fourier transform artifacts and take into account that a

diffractometer can measure only over a finite q-range up to the maximum value q_{max}.

Furthermore, since the pair distribution function is proportional to the probability of finding an atom at a certain distance from a reference element, it has been imposed to go to zero for distances smaller than the hard core of atoms.

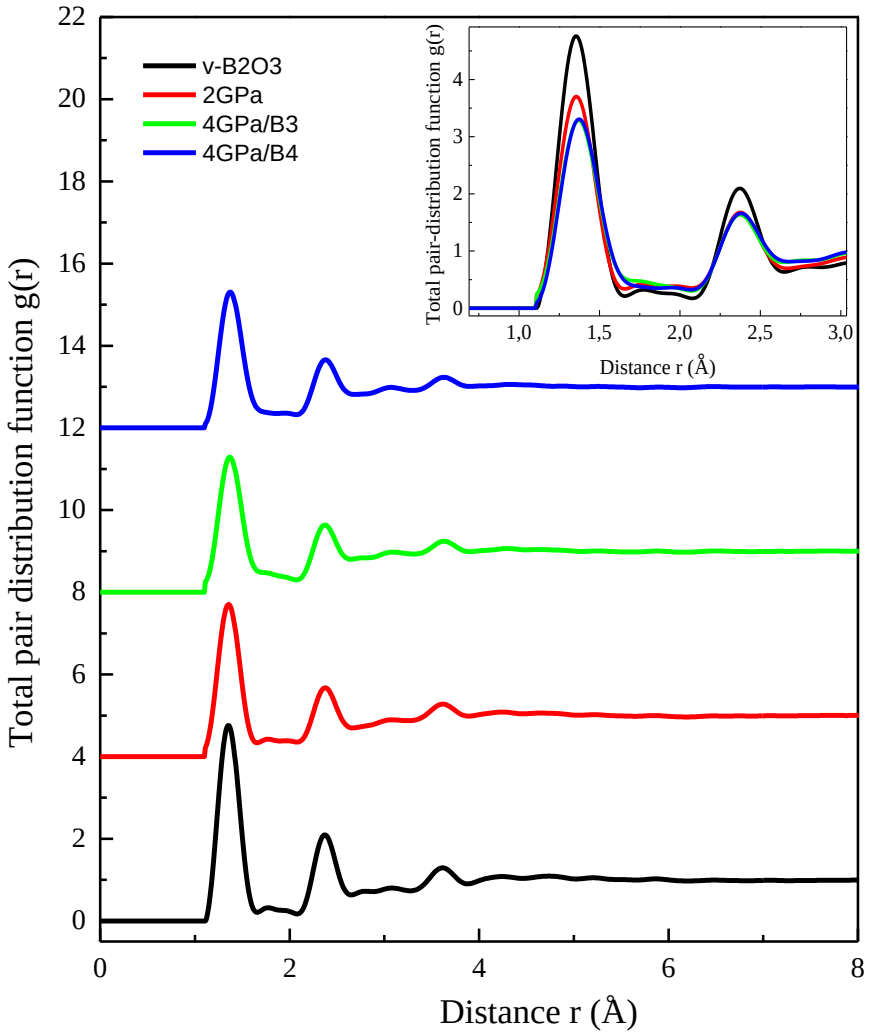

Figure 22. Neutron total pair-distribution function g(r) for B_2O_3 glass, obtained as Fourier transforms of the measured S(k) function shown in Figure 20. At r-values smaller than the distance of closest approach between two atoms the limiting values of $g(r \rightarrow 0)$ is imposed going to 0. The high-pressure data sets have been shifted vertically for clarity of presentation. In the inset, a zoom of low r-region is shown.

Hence, the radial distribution functions (RDF) have been calculated by the following equation:

$$RDF = 4\pi r^2 \rho g(r) \quad (7)$$

that allows us to get information about the average number of elements in a spherical shell with radius r and differential thickness dr (Figure 23).

Since the RDF is the radial number density of the sample at a certain distance of the reference molecule, not normalized to the area of the spherical shell, we can see that more molecules will be found as the distance to the reference particle increases.

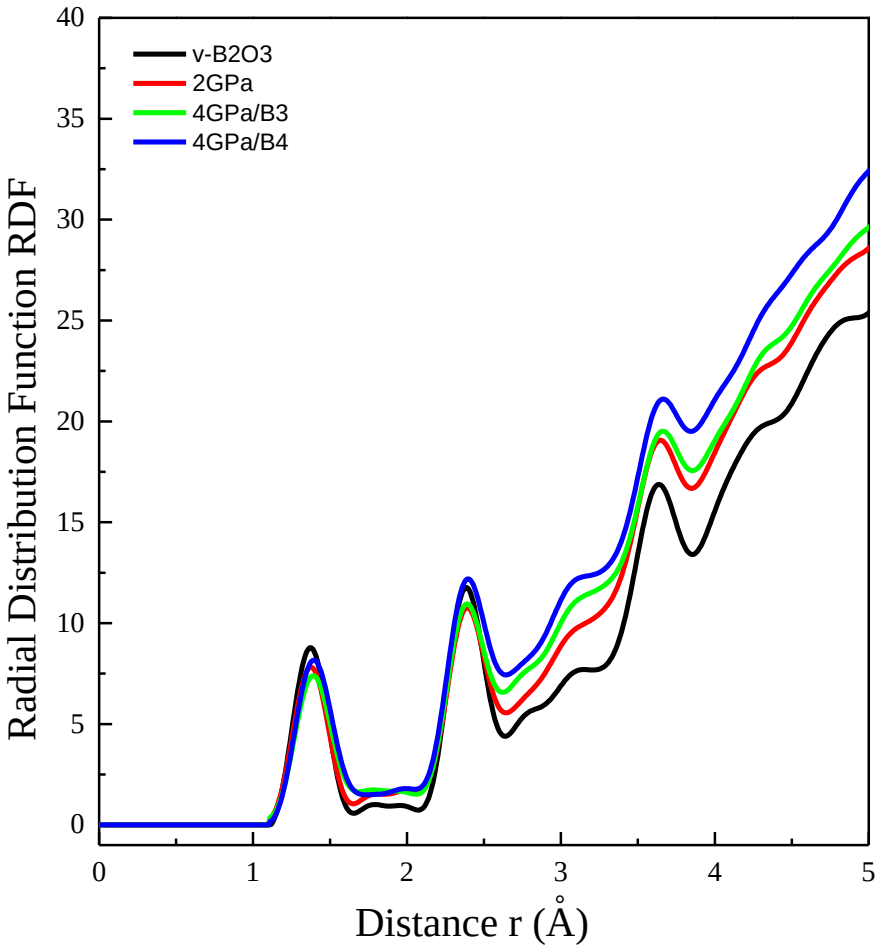

Figure 23. Radial distribution function for densified B_2O_3 glasses.

The integration of the radial distribution function will directly yield the mean coordination number $\bar{n}_{\alpha}^{\beta}$ of a certain shell:

$$\bar{n}_{\alpha}^{\beta} = 4\pi\rho\int_{r_i}^{r_j} dr r^2 g(r) = \int_{r_i}^{r_j} dr RDF \tag{8}$$

i.e. the average number of β atoms contained in a volume defined by two concentric spheres of radii r_i and r_j, centered on an α atom.

Some r-space values related to the measured functions are listed in Table 3.

Sample	ρ (Kg/m^3)	ρ_N (mol/Å^3)	R_1 (Å)	R_2 (Å)	R_3 (Å)	R_4 (Å)	R_2/R_1	n_B^o Step
v-B2O3	1826	0.07898	1.36	2.37	2.78	3.62	1.74	2.9
2GPa	2082	0.09006	1.36	2.37	2.77	3.62	1.74	3.0
4GPa/B3	2174	0.09404	1.37	2.37	2.77	3.63	1.73	3.0
4GPa/B4	2373	0.10265	1.37	2.38	2.77	3.63	1.74	3.3

Table 3. R-space parameters derived from the g(r) and the RDF of B_2O_3 glasses: the B-O bond distance R_1 as taken from the position of the first peak in g(r), the positions R_2, R_3, and R_4 of the second, third, and fourth peaks in g(r), the ratio R_2/R_1 and the mean B-O coordination number $\bar{n}_B^O$. The mass and numeric number density of the samples are also listed.

The first peak in g(r), located at R_1~1.36 Å, is associated with nearest-neighbor B-O correlations (19). By integrating over this peak up to the first minimum, the related mean B-O coordination numbers ($\bar{n}_B^O$) is found be around 3.

The increase in pressure up to 4 GPa does not provoke, within the experimental error, any considerable r-shift of the nearest-neighbor bond distance $R_{1;}$ however, the value of its coordination number $\bar{n}_B^O$ increases in the sample 4GPa/B4, consistently with the presumed formation of borons in fourfold coordination.

The second peak in g(r) is localized at R_2~2.37 and preserves its positions for all the investigated pressure conditions. It can be attributed both to the O-O distances within BO_3 units and the B-B distances between corner–linked triangles (19).

By considering the structure consisting of planar boroxol rings formed from the linkage of three regular equilateral BO_3 triangles (*Figure 24*), the O-O and B-B distance are supposed equal, so that $r_{OO}/r_{BO}=r_{BB}/r_{BO=}\sqrt{3}$ =1.73 (20).

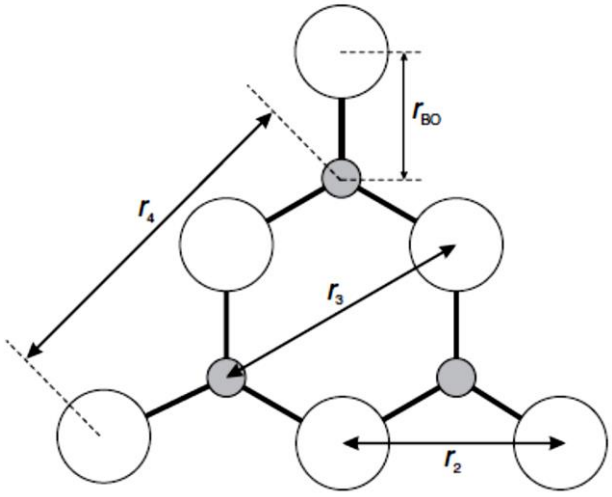

Figure 24. Scheme of a planar B_3O_6 boroxol ring showing several of its characteristic interatomic separation. The B and O atoms are indicated by the small grey and large open circles, respectively.

The ratio values r_2/r_1, measured in this study are therefore in perfect accordance with the expected ones.

The third and fourth peaks in g(r) have contributions from boron to second-neighbor oxygen distances (20). In particular, r_3 is assigned to BO distance when both atoms lie within the same ring and r_4 corresponds to BO distance if the B atom has its second-neighbor oxygen atom outside of its ring.

The experimental findings well confirm the predictable value, $r_3/r_1=2$ and $r_4/r_1=\sqrt{7}$.

With increasing the pressure, the third peak is broadened and its intensity decreases. Since a large contribution for this peak probably comes from boroxol rings (19), then the intensity reduction is consistent with the Raman scattering experiments which show that the boroxol ring breathing modes at 808 cm^{-1} (see section 5.4) are progressively suppressed by the pressure.

The occurrence of not conspicuous changes in the g(r) implies that the short-range structure of BO_3 units is preserved. Conversely, they reorganize on an intermediate length scale as indicated by changes in the FSDP.

5.4 Effect of pressure on low energy vibrations of borate glasses: Raman spectroscopy, neutron scattering and specific-heat measurements

As widely described in Chapter 1, amorphous solids show universal characteristics in their low-frequency vibrational behavior, not found in their crystalline counterparts. At temperatures below 30 K, the reduced specific heat C_p /T^3 of these systems exhibits a sizable hump, which corresponds to an excess of low-energy vibrational states above the expected Debye level for acoustic waves model. This excess, referred to as the "boson peak", is revealed also in inelastic neutron (21) and Raman-scattering (22) measurements below 10 meV.

It has to be considered that a great number of structural parameters (including connectivity, nature of intermolecular and intramolecular bonds, and spatial dimensionality) potentially contribute to the low-energy dynamics and it is a very complicated task to separate their specific contribution and to establish how and how much they influence the BP.

Such difficulty can be overcame by investigating the vibrational dynamics of systems in which the structural modifications are controlled and limited.

For this purpose, alterations of the network structure caused by the densification offer the possibility to shed light on the nature of BP. Indeed, they lead to significant modifications of the short and medium range orders and to the reduction of the atomic mobility without altering the stoichiometry (23).

The present paragraph is focused mainly on elucidating the influence of the densification on the low-energy vibrational dynamics of borate glasses.

A combined use of inelastic neutron scattering INS, Raman and calorimetric measurements allowed us to get a detailed picture of the vibrational modes of these systems.

5.4.1 Raman measurements

The Raman spectra of borate glasses at ambient pressure (v-B_2O_3) and permanently densified at 2GPa (2GPa) and 4 GPa (4GPa/B3 and 4GPa/B4) are shown in Figure 25 a), in the frequency range 10-1000 cm^{-1}.

Firstly, to each spectrum a background has been subtracted corresponding to the value of the Raman intensity at the highest investigated frequency, i.e., the region where no molecular vibrations are revealed. Then, the spectra have been normalized by the total integrated intensity of the multicomponent band between 330 and 760 cm^{-1}, which reflects the vibrations of all the units forming the whole glassy network.

It can be observed that all spectra at high frequency exhibit a strong, sharp, and highly polarized band at 808 cm^{-1}, which arises from a localized breathing-type vibration of oxygen atoms inside the symmetric planar boroxol rings (24). It preserves its frequency after densification, indicating no variation of boron coordination; however, a progressive depression of its intensity with increasing density is observed.

In the 4GPa/B4 sample, a further band at 775 cm^{-1} appears (indicated with an arrow in the Figure 25a), which is associated to the vibrations of superstructural units containing tetrahedral BO_4 groups (the pentaborate units). Therefore, this feature is a signal of the variation in the chemical bond characterizing the network and of the rise of fourfold-coordinated boron atoms (25).

Conversely, both the frequency region between 300 and 750 cm^{-1} and the region below 200 cm^{-1} of all the investigated samples notably change with the densification.

The latter region is characterized by the presence of a broad band, the Boson Peak. By increasing the density, the magnitude of the BP maximum decreases and its frequency position changes from 26 cm^{-1} in normal B_2O_3 to about 68 cm^{-1} in 4 GPa/B4 (see values in Table 4).

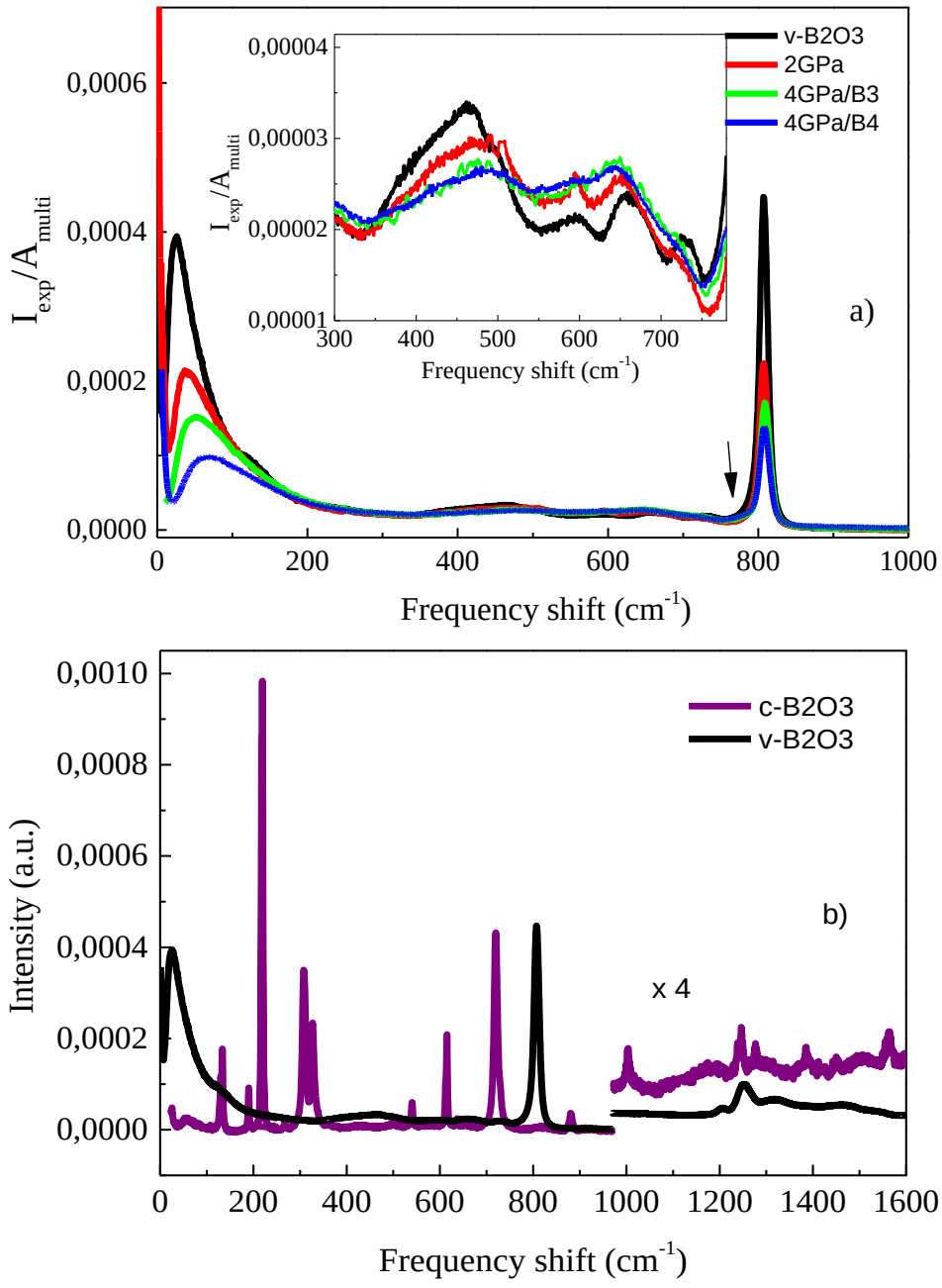

Figure 25. a) Raman intensity I_{exp} of vitreous B_2O_3 and of densified glasses, normalized by the total integrated area of the multicomponent band between 330 and 760 cm^{-1}(shown in the inset).
(b) Raman spectra of v-B2O3 (black line) and c-B2O3 (violet line). Above 970 cm^{-1}, the y scale is expanded by a factor of 4.

The intermediate frequency range above 300 cm^{-1} is better shown in the inset of Figure 25 a. It appears rich in features that change with the densification.

Because, as deduced by neutron diffraction experiments (see section 5.3), the B-O and O-O distances remain essentially unchanged upon densification, the observed changes can be attributed to the bending, breathing, twisting puckering vibrations and flexing vibration mode of B and O units in n-membered rings, similarly to the widely studied silica oxide glass.

The Raman main band at 450 cm^{-1} gradually broadens and shifts to 475 cm^{-1} with the increase of pressure. This indicates a larger mean value and a narrower distribution of B-O-B angles by compression.

The sharp peak at ~ 600 cm^{-1} can be attributed to the breathing mode of 3-membered rings of B and O. The shift to higher frequency can be believed to be caused by the slight buckling of these rings with densification.

Conversely, the clear shift to lower frequencies of the band at 650 cm^{-1} might be associated with a B-O stretching motions and would suggest a lengthening of B-O bonds with increasing densification.

The observed changes in intensities might indicate that the network to which the n-membered rings are bonded and in which they vibrate is modified during the different cold-compression process.

In Figure 25 b), the spectrum of the vitreous B_2O_3 compared to the corresponding crystalline phase (c-B_2O_3) is shown.

Unlike the glass, which is characterized by a wide distribution of bonds and torsion angles, the crystal shows a strictly limited number of them. Its structure, indeed, is built on infinite ordered chains of interconnected BO_3 triangles (26), which determine the presence of narrow peaks in the Raman spectra. Moreover, the 808 cm^{-1} band does not appear in c-B2O3, implying the absence of boroxol rings within the crystalline structure.

According to Shuker and Gammon (27), the low frequency Raman scattering I_{exp} in glasses is related to the vibrational density of states g(ω) by the following equation:

$$I_{\exp}(\omega) = \frac{C(\omega)g(\omega)[n(\omega,T)+1]}{\omega} \quad (9)$$

where $[n(\omega,T)+1]$ is the Bose-Einstein population factor for the Stokes component, C(ω) is the light-vibration coupling coefficient and ω the harmonic propagator (27)

Figure 26 shows the normalized spectra I_N for ω<200 cm^{-1}, which represent the product between the true vibrational densities of states as $g(\omega)/\omega^2$ and the coupling constant C(ω):

$$I_N(\omega) = \frac{I_{\exp}}{\omega[n(\omega,T)+1]} = C(\omega)\frac{g(\omega)}{\omega^2} \quad (10)$$

At frequencies lower than the BP position, the spectra are marked by the quasielastic light-scattering excess QS, which is associated to the coupling between the light and the thermally activated fast relaxations (28).

It exhibits a temperature dependence much stronger than the Bose factor and dominates the frequency region below about 20 cm^{-1}.

An accurate elimination of all the relaxation mechanisms which are the source for QS requires to perform Raman-scattering measurements at low temperatures, down to about 10 K (29). However, low temperature light scattering measurements of fast relaxation in v-B2O3 showed that QS affects significantly the low-frequency spectra up to about 10 cm^{-1} (30).

In the present study the fast relaxation contributions have been subtracted from all the spectra by fitting them through a Lorentzian function centred at ω=0.

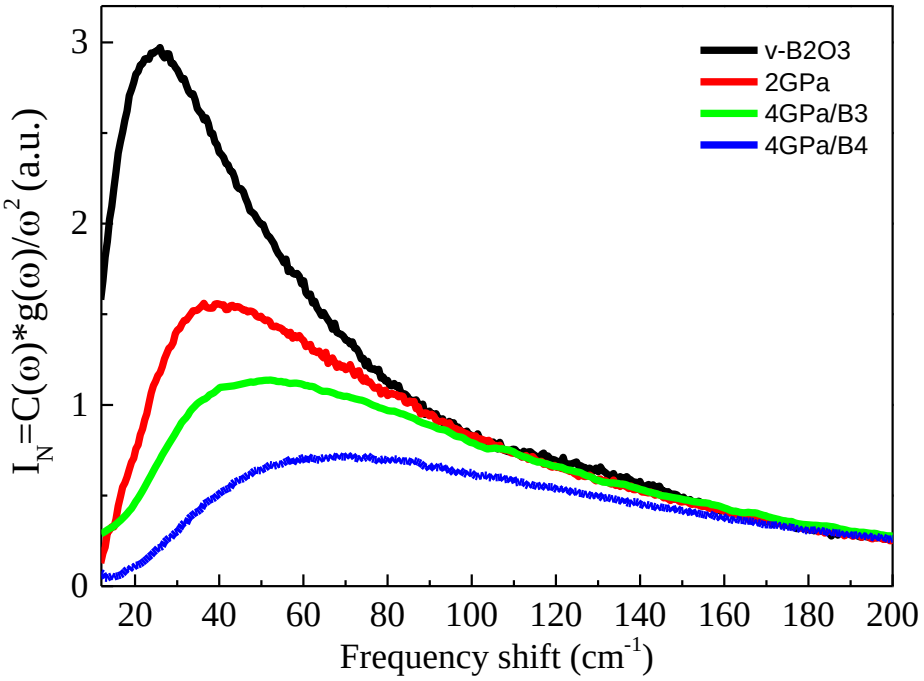

Figure 26. Normalized Raman spectra of densified borate glasses in the BP region. The fast relaxation contributions, which dominate the Raman pattern at low frequency and high temperatures, have been evaluated through a Gaussian fit and subtracted from all the spectra.

The *Figure 27* shows the normalized intensities of the BP (blue circles) and of the band at 808 cm^{-1} (green triangles) as a function of the atomic packing fraction ϕ, which is defined as

$$\Phi = \frac{N_A V_{atomic}}{V_{molar}} \qquad (11)$$

V_{molar} being the molar volume and V_{atomic} the ionic volume.

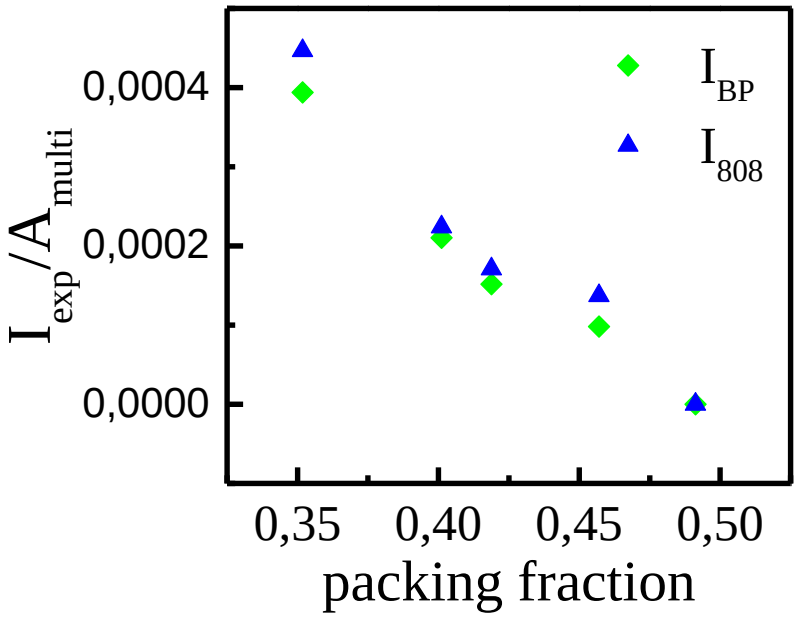

Figure 27. The normalized intensities of the BP (green diamonds) and of the band at 808 cm^{-1} (blue triangles) as a function of the atomic packing fraction φ.

The densification leads to a progressively decreasing content of boroxol rings, as inferable by the decrease of 808 cm^{-1} band, until their full disappearance in the crystal, characterized by the most efficient packing of BO_3 units.

It is worth noting that also the BP decreases its intensity with increasing density and, most importantly, both the bands show a strikingly similar linear decrease, pointing to zero in correspondence to the value of the crystal.

Reasonably thus these observations disclose a strong correlation in glasses between the boroxol ring population and the additional localized low energy vibrations of unknown units underlying the BP.

It is important to remark that, beyond the boroxol rings, some further superstructural units can characterize the network of densified glasses and determine the low energy excess vibrational contribution. These superstructural units could arise from the breaking up of boroxol rings in the melt under pressure, which originates the formation of larger puckered rings made up of connected BO_3 triangles folded on themselves. They are surely

preserved in densified glasses also contributing to the observed increase of the packing (23). Therefore, it is conceivable that these large rings can also be a source for the excess soft energy vibrations, contributing to both the BP and excess heat capacity.

Another interesting evidence is obtained by plotting the curves I_N scaled by the maximum intensity of the BP, $I_{BP,}$ as a function of the ratio ω/ω_{BP} (Figure 28). Despite the significant differences observed in Figure 25a for BP amplitudes and positions, surprisingly all the scaled curves overlap and show a nearly identical shape up to ω/ω_{BP} =5.

The invariance of I_N/I_{BP} curves, reveals that all the low energy vibrational modes underlying the BP, extended and localized, are coupled and hybridized, determining an overall spectral distribution whose spectral shape does not depend on the different packing fractions of the systems.

The small differences observed on the right side of the BP can be ascribed to residual quasi-elastic light-scattering contribution.

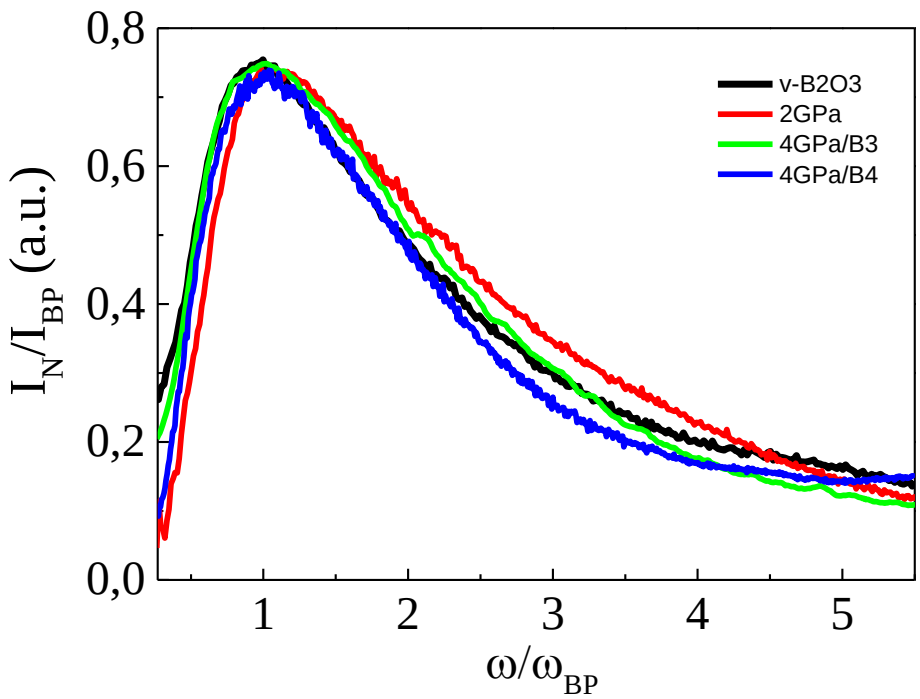

Figure 28. Normalized Raman intensity, I_N, scaled by the maximum intensity of the BP, $I_{BP,}$ as a function of the ratio ω/ω_{BP} of normal and densified B_2O_3 glasses.

5.4.2 Inelastic neutron scattering measurements

In Figure 29 the low-frequency vibrational densities of states derived by inelastic neutron scattering measurements, represented as $g(\omega)/\omega^2$, are shown. Also neutron spectra are characterized by the decrease of BP intensity and the shift of its frequency position ω_{BP} to higher values with increasing the packing of the system (Table 4).

By comparing Raman and neutron spectra, it's noticeable that the shapes of the patterns are similar. However, the frequency values obtained by Raman measurements ω'_{BP} are always higher than those obtained by inelastic neutron scattering ω_{BP}. Indeed, the neutron BP frequency, $\omega_{BP,}$ corresponds to the maxima in $g(\omega)/\omega^2$, while the Raman BP frequency, $\omega'_{BP,}$ is also related to the phonon-photon coupling coefficient $C(\omega)$, which is not constant but rather a monotonically increases with ω.

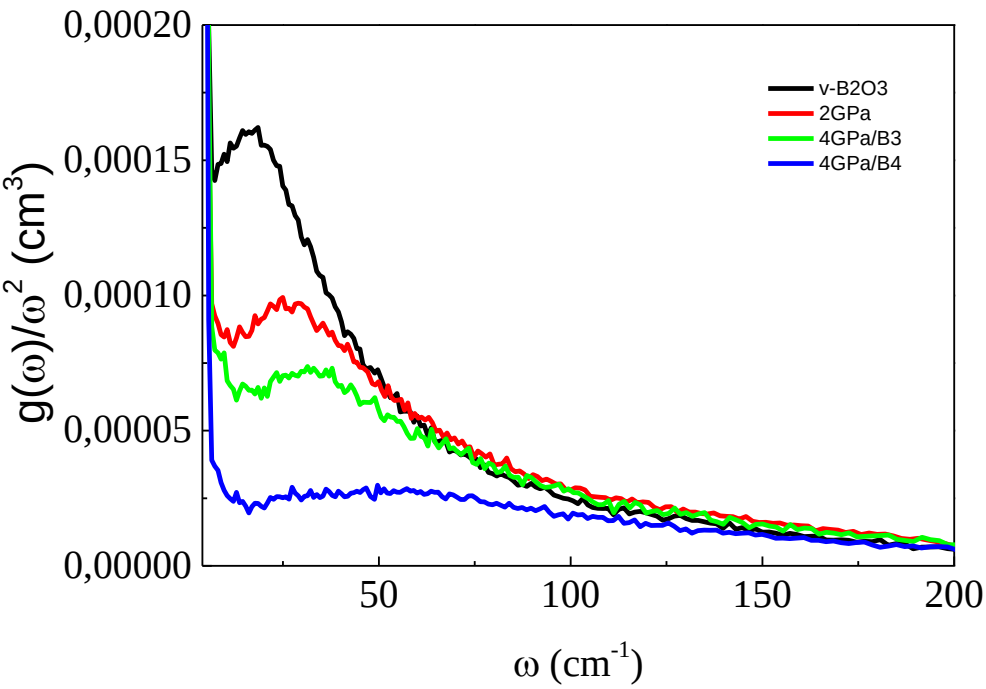

Figure 29. Vibrational density of states $g(\omega)/\omega^2$ by inelastic neutron scattering measurements as a function of frequency for densified borate glasses.

5.4.3 Specific-heat measurements

The temperature dependence of the reduced specific-heat C_p/T^3 for the investigated samples is shown in *Figure 30.*

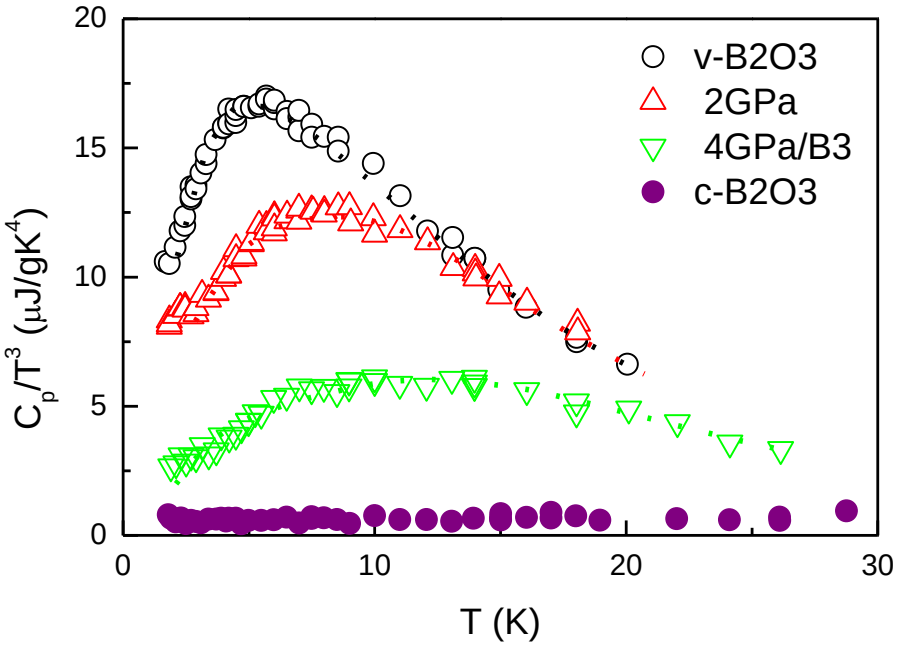

Figure 30. Temperature dependence of the specific heat as C_p/T^3 of the densified B_2O_3 glasses.

All the investigated glasses show a well-defined asymmetric broad peak, which is the evidence of an excess $C_p(T)$ over the specific-heat capacity of the Debye contribution $C_D(T)$ defined as

$$C_D = \frac{2\pi^2 k_B^4}{5\hbar^3\rho}\left[\frac{1}{3}\left(\frac{1}{v_L^3}+\frac{2}{v_T^3}\right)\right]T^3 = \frac{2\pi^2 k_B^4}{5\hbar^3\rho}\frac{T^3}{v_D^3} \qquad \textbf{(12)}$$

A growing densification depresses the excess specific heat $C_P(T)$ over the whole explored temperature range, giving rise to a significant decrease of the peak intensity and to an increase of the bump temperature T_{max}, which shifts from about 5.7 K in v-B2O3 to about 12 K in 4-GPa/B4 glass (see Table 4).

To point out the changes of the excess specific heat arising from the variations of the elastic continuum, the specific heat $C_P(T)$ scaled by $C_D(T)$ for the densified B_2O_3 glasses as a function of T/Θ_D is shown in *Figure 31*.

It increases its intensity with densification and exhibits an evident shift of the maxima.

This observation reflects a variation of T_{peak} stronger than that experienced by Θ_D. Importantly, by scaling the specific heats of densified B_2O_3 glasses by the specific-heat of the peak $(C_p/T^3)_{peak}$ in the bumps region, a surprising identical shape of the curves is evidenced (*Figure 32*).

These findings well agrees with the invariance of the shape of the scaled B_P revealed by Raman scattering (Figure 28) and confirm the results obtained in densified SiO_2 (31) and GeO_2 (32) glasses and alkaline borate glasses (33).

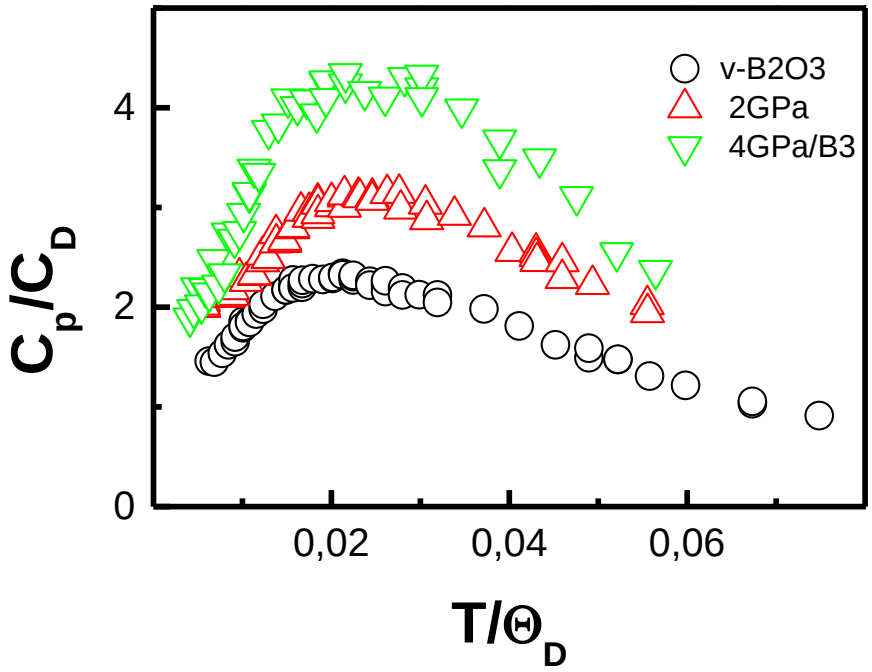

Figure 31. $C_P(T)$ scaled by $C_D(T)$ for the densified B_2O_3 glasses as a function of T/Θ_D.

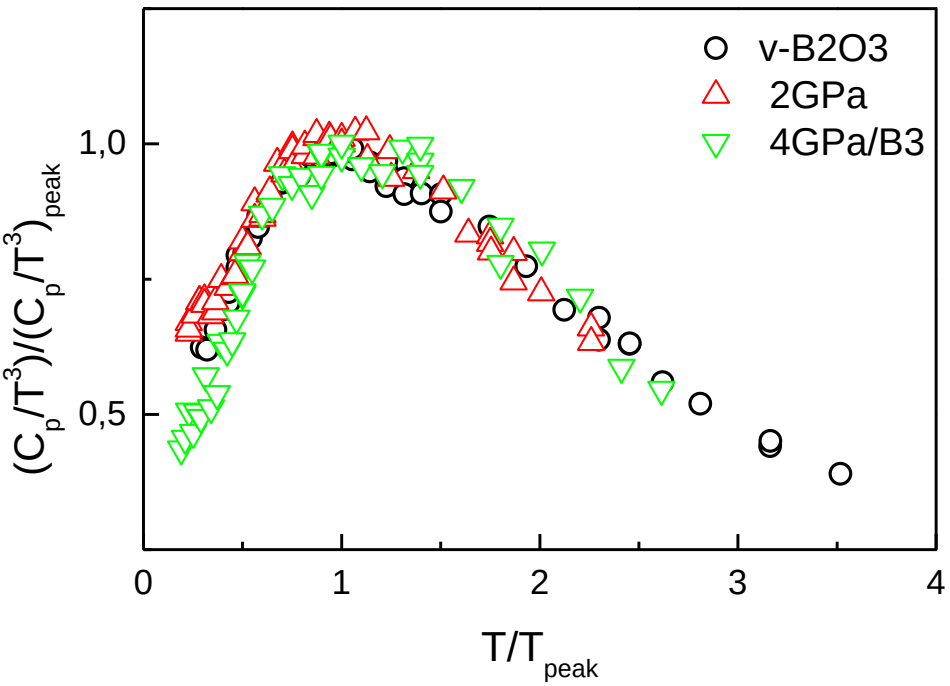

Figure 32. The specific heats of densified B_2O_3 glasses, plotted as $C_P(T)/T^3$, scaled by the specific-heat of the peak $(C_P/T^3)_{peak}$ as a function of T/T_{peak}.

Moreover, all the samples show an upturn below T=2.5 K, particularly evident in more densified glasses. It is usually ascribed to the existence of tunneling states in glasses exhibiting a linear dependence on temperature (34). It is more evident in samples where the peak intensity is lower and its maximum is shifted to higher temperatures.

More accurate measurements at lower temperature would be required for the study of this topic; however, it is beyond the purpose of this thesis.

Low-temperature specific heat and low-energy vibrational density of states are connected by the following equation:

$$C_P \approx C_V = 3Nk_B \int_0^{\omega_0} g(\omega)\left(\frac{\hbar\omega}{k_B T}\right)^2 \frac{e^{(\hbar\omega/k_B T)}}{\left[e^{(\hbar\omega/k_B T)}-1\right]^2} d\omega \qquad (13)$$

where N is the number density, K_B is the Boltzmann constant and ω_o the highest vibrational frequency.

In particular, the position of the bump in the specific heat refers directly to the boson peak, being the equivalent in temperature of the BP energy in the dominant phonon approximation.

5.4.4 Relations between Raman, neutron and specific heat results and determination of coupling coefficients C(ω)

The experimental results shown in the previous paragraphs evidence a good agreement between spectral shapes of densities of states and the specific-heat behavior. All the spectra are indeed characterized by a large peak showing a widening on the descending side (Figure 26, 29 and 30); moreover, the position and the intensity of the boson peak in $g(\omega)/\omega^2$ follows closely the changes with the density displayed in the C_p/T^3.

Samples	ρ_N (mol/Å^3)	φ	ω'_{BP} (cm^{-1})	ω_{BP} (cm^{-1})	T_{MAX} (K)
v-B2O3	0,07898	0.352	26	17	5.7
B2O3-2GPa	0,09006	0.401	37	26	7.7
B2O3-4GPa/B3	0,09404	0.419	51	32	10
B2O3-4GPa/B4	0,10265	0.457	68	47	12

Table 4. Values of the molecular number density ρ_N, atomic packing fractio **φ**, *BP frequency by Raman (*ω'_{BP}*) and neutron (*ω_{BP}**)** *scattering and the temperature T_{max} of the bump in the C_P/T^3 of the studied glasses.*

An accurate comparison between the experimental results points out that the change of the Raman intensities with the density in correspondence of the maximum are unusually small in proportion to those observed for T_{max} of the specific heat data.

This evidence leads to believe that the strength of the phonon-photon coupling constant $C(\omega)$ changes for the different processes of densification in a nontrivial way.

However, both low-energy Raman and neutron scattering spectra show maxima whose frequencies, ω_{BP} and $\omega'_{BP,}$ increase with density with the same rate of T_{max} in C_P/T^3 data (***Figure 33***).

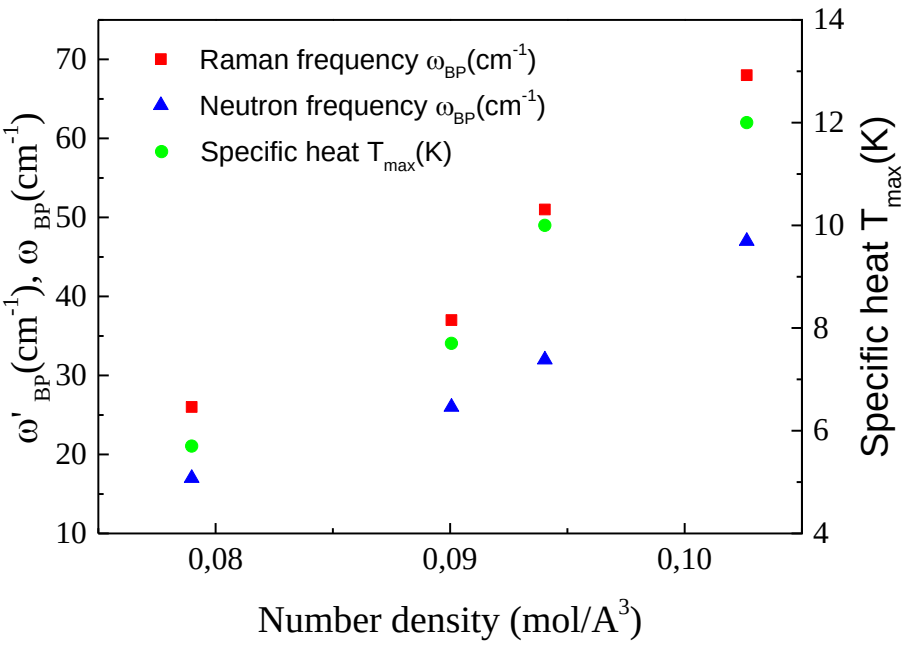

Figure 33. BP frequencies in Raman and neutron scattering measurements (ω'_{BP} and $\omega_{BP,}$ respectively) and temperature of the bump in C_P/T^3 (T_{max}) as a function of the molecular number density.

Consequently, both experimental probes seem to be sensitive to the same vibrations revealed in the specific-heat measurements.

Hence, these techniques are interchangeable in providing information about the boson peak.

Thanks to the availability of both neutron and Raman spectra, the determination of the Raman light-to vibration coupling coefficient $C(\omega)$ has been possible, by dividing the normalized Raman intensity I_N by $g(\omega)/\omega^2$ (*Equation 9*).

The knowledge of the frequency dependence of coupling coefficient $C(\omega)$ is very significant to clear up some questions about low-frequency vibrations, because it contains information on the vibrational wave function (27) and consequently can make easier the identification of the modes involved in the ambiguous dynamics of the boson peak.

The two most known models suggested for the description of $C(\omega)$ are based on different predictions: the first one, formulated by Shucker and Gammon (27), predicts that $C(\omega)$=const and assumes that the vibrations in glasses are localized on a distance much shorter than the light wavelength. The second model was proposed by Martin and Brenig (35) and suggests that at low frequency $C(\omega)\sim\omega^2$, as a consequence of the effect of the polarizability disorder on slightly damped acoustic waves.

More recently it has also found that quasi-plane acoustic waves with finite mean free path l also contribute to the low-frequency Raman spectrum with $C(\omega)\sim\omega^2$ when $l^{-1}\sim\omega^4$ (36) or with $C(\omega)$=const when $l^{-1}\sim\omega^2$ (37).

Although there is a widespread assumption that the vibrations around the boson peak are hybridized and cannot be easily separated, this issue is not yet fully settled.

A linear frequency dependence of $C(\omega)$ in the frequency region below 150 cm^{-1} is a behavior common to many glassy systems (38).

On the hand hand, a constant value of $C(\omega)$ is invoked by different models (38) and associated to the existence of localized vibrations.

The finding of a universal behavior of $C(\omega)$ for glasses having different structures should suggest the presence of a single type of vibrations in the BP region. Anyway, the possibility that two possible interrelated types of vibrations (localized and propagating) coexist, cannot be precluded (39).

The experimental determination of the elastic constant is a difficult task, just because in order to avoid the influence of the quasi-elastic contribution, very low-temperature light and neutron scattering data should be used. However, it's worth to remark that, although the spectroscopic data reported in this study have been collected at room temperature, the quasi-elastic contribution decays so fast that it is negligible above 20 cm^{-1} for all glasses, making the following analysis reasonable.

The coupling coefficients obtained for investigated samples are shown in Figure 34.

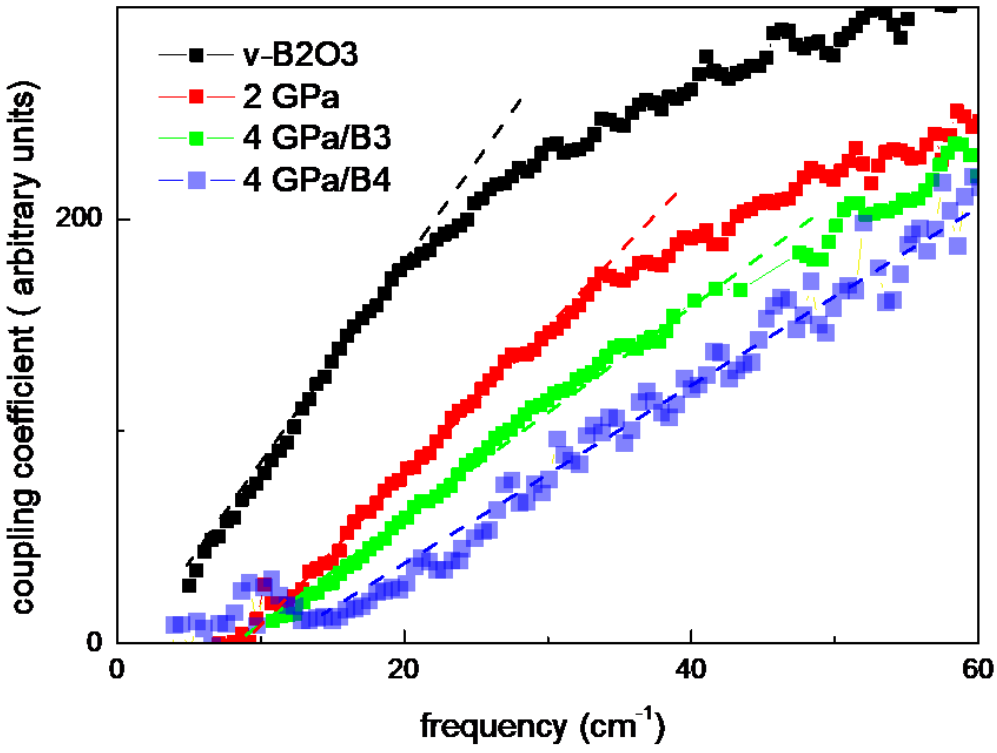

Figure 34. Frequency dependence of the coupling coefficient C(ω) densified B2O3. Dashed lines are descriptions by linear dependence.

In the low frequency region, $C(\omega)$ reveals a similar frequency behaviour in all the investigated samples, showing a linear trend in proximity of the frequency position of the Boson Peak.

Indeed, the linear regime is maintained up to higher frequencies in samples of increasing density. Furthermore, the magnitude of $C(\omega)$ is different for the different densified samples: for frequencies below 50 cm^{-1}, it decreases by increasing density, tending to a similar value at frequencies higher than 60 cm^{-1}.

As concerning the linear frequency dependence of $C(\omega)$, it has recently shown that a broad set of different glasses can be scaled to a single master plot with a frequency dependence $C(\omega)=A(\omega/\omega_{BP}+B)$, where B=0.5 and ω_{BP} is defined as the position of maximum of $g(\omega)/\omega^2$ (33).

In Figure 35, $C(\omega)$ plotted against the scaled frequency ω/ω_{BP} is shown.

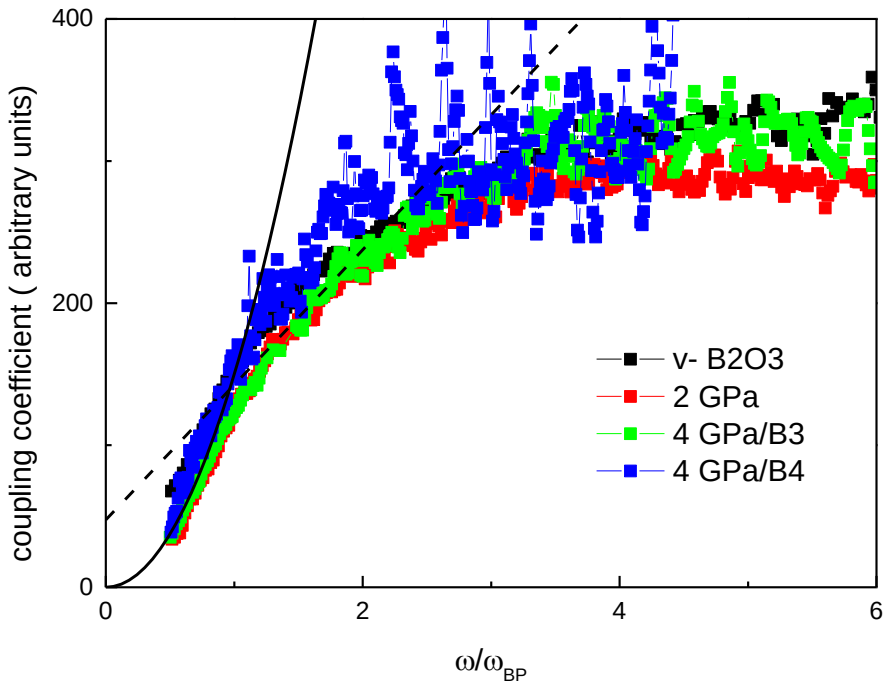

Figure 35. Frequency dependence of the coupling coefficient $C(\omega)$ of densified glasses as a function of the scaled frequency ω/ω_{BP}. The dashed-dotted line is a fit of $C(\omega) \propto \omega/\omega_{BP}+0.5$. The solid line is a fit $C(\omega) \propto \omega^{2}$.

Importantly, although the coupling coefficients show differences for the differently densified samples (Figure 34), they strikingly falls onto the same curve after the frequency is scaled by the boson peak position (Figure 35).
More precisely, above the boson peak ($\omega/\omega_{BP}>1$) a linear behavior described by the equation $C(\omega)=A(\omega/\omega_{BP}+0,5)$ is observed.

Conversely, in the region below and near the BP, the coupling coefficient strongly deviates from the previous linear behavior and, in analogy with the observation of Surovtsev and Sokolov (38), follows a quadratic frequency dependence $C(\omega) \propto \omega^2$, tending to the value $C(\omega)=0$ to the limit $\omega \rightarrow 0$, as expected in the case of scattering from acoustic-like vibrations (35) or from spatially attenuated acoustic waves (36).

This finding is observed in all the samples, leading to the conclusion that the boson peak wave functions are unaffected by the density.

The change in C(ω)-frequency dependence from parabolic to linear suggests a wide participation of acoustic modes to the boson peak dynamics. Therefore, the BP frequency marks the crossover to a different regime, where localized and extended excitations plausibly coexist.

Finally, the prediction of the Soft Potential Model as concerns the variations of the boson peak frequency under pressure has been verified (40).

According to SPM predictions

$$\omega_{BP}(P) = \omega_{BP}(0)\,(1+P/P_0)^{1/3} \qquad \textbf{(14)}$$

where P_0 is related to the bulk modulus K and two parameters of soft potentials: the strength of the random force f_0 between quasilocalized vibrations and a random deformation potential of the quasilocalized vibration (40).

It has been found that, assuming P_0 constant ($P_0=0.71$), the Equation 14 well describes the behavior of the boson peak frequency with pressure in all investigated densified samples, except for the 4GPa/B4 samples (***Figure 36***).

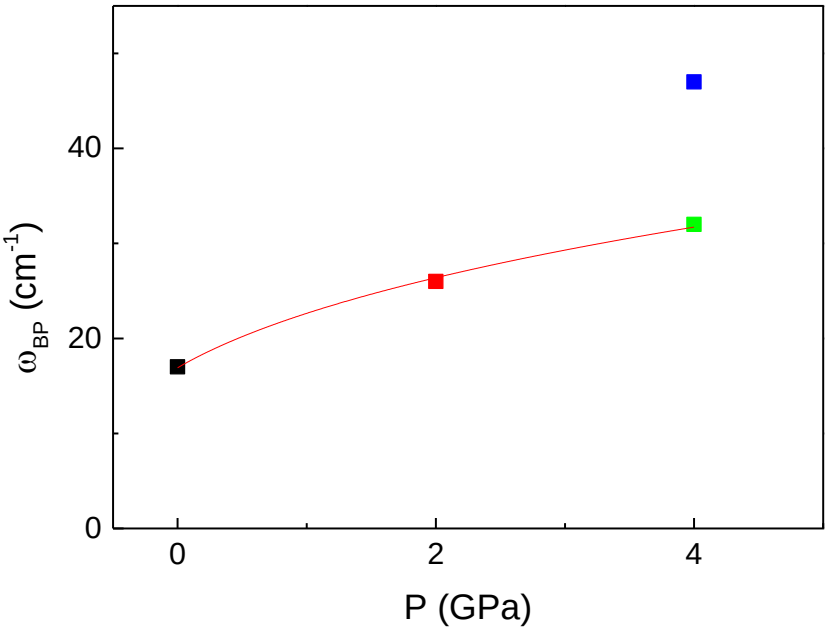

Figure 36. Pressure dependence of the boson peak frequency in densified B_2O_3 compared to the prediction of the soft potential model. Symbols are experimental data and line is the fit. The fit assumes P_0 is independent of pressure and equal to 0.71.

The deviation observed in 4GPa/B4 can be ascribed to the relevant changes of the atomic structure occurred during the hot compression, leading to the formation of BO_4 units.

5.4.5 Relation between the boson peak strength and the elastic moduli

Different hypothesis have been advanced about the boson peak origin, ascribing it to van Hove singularities located at high-symmetry points at the boundaries of the first Brillouin zone (41) or to the existence of a strongly dispersive transverse-acoustic branch (42).

Importantly, recent measurements on metallic glasses have pointed out a possible relation between the boson peak strength and the elastic moduli (43; 33).

In these studies, it was observed that, in many crystalline and glassy systems, the peak temperature T_{max} of the reduced low temperature specific heat is related to the crossover frequency, ω_{co}, where the Debye and the effective experimental VDOS cross for the first time (44).

The crossover frequency ω_{co} should correspond to the Brillouin-zone-boundary frequency for shear waves, which for elastically isotropic glasses is defined as

$$\omega_{CO} = \left(\frac{2}{\pi}\right)\left(\frac{c_{44}}{\rho}\right)^{1/2} K_{BZ} \qquad \textbf{(15)}$$

where ρ is the density, C_{44} is the elastic constant for pure transverse waves, and K_{BZ} is the wave vector magnitude at the end of the first pseudo-Brillouin zone. Therefore, the Equation 15 implies a linear correspondence between the frequency of the boson peak and the transverse velocity v_t, since $C_{44} = \rho v_t^2$.

The dependence of T_{max} on the shear velocity v_t, for the investigated samples is shown in Figure 37.

By increasing the density, the temperature of the bump in C_p/T^3 increases linearly with v_t, and it seems clear that the validity of the Equation 15 is

confirmed also by a wide group of glasses (33; 45), appearing as a promising general feature of glasses.

Furthermore, it's important to note that in these glasses the longitudinal sound velocity is related to the transverse component (Table 5) by the relation $v_L=1.7\ v_T$.

Taking these results into consideration, it is possible to affirm that transverse modes are directly involved in the boson peak dynamics settling its position. Moreover, the asymmetric shape of the boson peak, appearing as a broadening on its right tail (Figure 26 and 29) can be considered as the signature of the involvement of longitudinal modes, which are expected to contribute at higher frequencies and temperatures.

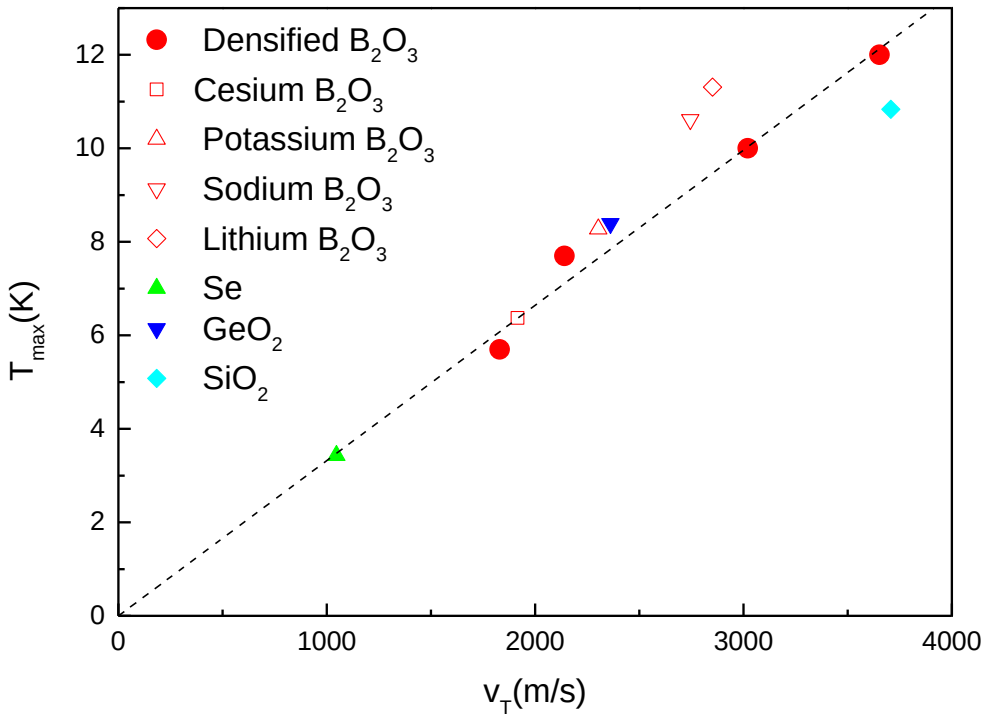

Figure 37. *Temperature T_{max} of the bump in the C_p/T^3 as a function of transverse velocity for densified borate glasses. In the figure the data of Se, GeO_2, SiO_2* **(45)** *and lithium, sodium, potassium, cesium borate glasses are also reported* **(33)**.

Samples	ρ_N (mol/Å^3)	V_L (m/s)	V_T (m/s)	B (GPa)	G (GPa)	Y (GPa)
v-B2O3	0.07898	3242	1830	11.04	6.11	15.48
B2O3-2GPa	0.09006	3737	2141	16.35	9.54	23.97
B2O3-4GPa/B3	0.09404	5287	3021	34.31	19.84	49.90
B2O3-4GPa/B4	0.10265	6393	3653	53.76	31.67	79.65
c- B2O3	0.11030	8344	4069	121.24	42.22	113.49

Table 5. Values of room temperature molecular number density ρ_N , longitudinal v_L and trasversal v_T sound velocity, shear (G), bulk (B) and Young's (Y) modulus, of B_2O_3 densified glasses, determined by ultrasonic measurements.

Since the structure of the investigated densified glasses and the atomic forces inside and between the structural units are basically of the same type, the strong differences in the vibrational dynamics and sound velocities are ascribed to the effects of the densification. Indeed, notwithstanding the short-range order is almost preserved over a wide range of pressure, an increase of density determines the shrinkage of interstitial voids and the consequent reduction of the distances between the boroxol units. Hence, the different size of the structural voids will imply the formation of bonds of different strength between the atoms and the surrounding groups, strictly influencing the Coulombian interaction and the potential energy gradient.

A more detailed information about the nature of molecular bonds can be inferred by the elastic moduli. The elastic bulk modulus (B), Young's modulus (Y), and shear modulus (G) of the investigated glasses have been determined from the experimental values of density ρ, longitudinal velocity v_l, and shear velocity v_t, using the Lamè coefficients $\lambda = \rho(v_l^2 - 2v_t^2)$ and $\mu = \rho v_t^2$ through the following standard relations:

$$Y = \mu \frac{3\lambda + 2\mu}{\lambda + \mu} \tag{16}$$

$$B = \frac{3\lambda + 2\mu}{3} \tag{17}$$

$$G = \mu \tag{18}$$

The measured shear, bulk, and Young's moduli follow the same trend of ultrasonic velocities with the density (Figure 38).

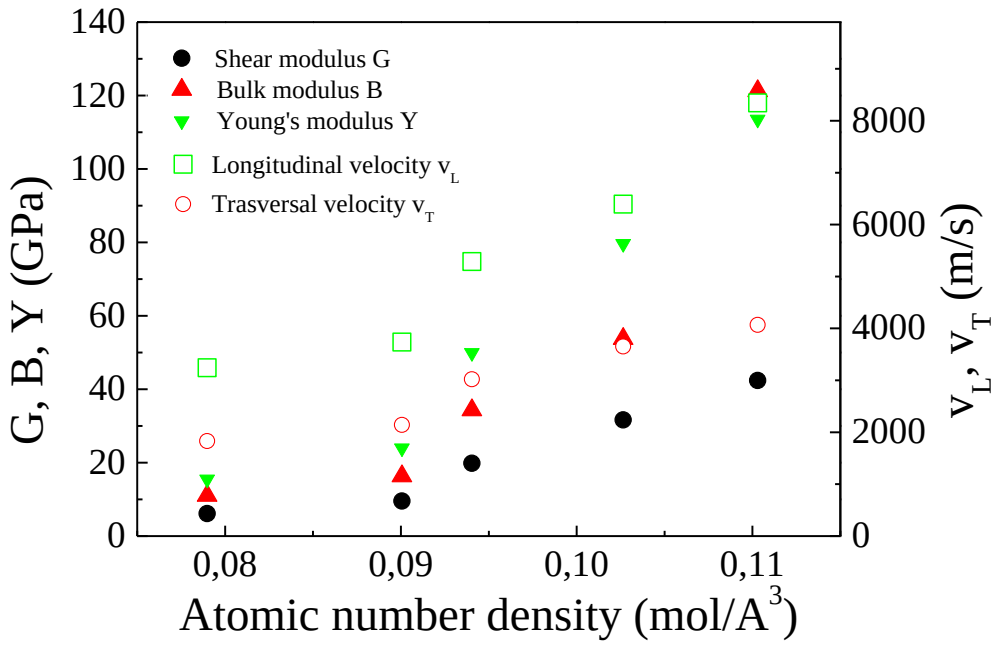

Figure 38. Longitudinal (v_L) and trasversal (v_t) velocities as a function of molecular number density. The elastic bulk (B), Young's (Y), and shear (G) moduli are also shown.

The reduced resistance to shear in less densified glasses could arise from their looser structure in comparison with more compacted ones.

According to the model proposed by Bridge and Higazy (46), the bulk modulus of the glass network depends on both the cross-link density and the bond-stretching force constant.

Therefore, the observed differences in the bulk modulus of the investigated glasses should mostly arise from marked differences in the bond-stretching force constants, related the size of the structural voids.

The densification determines a growing strength of interaction between the structural units and, as a consequence, the B-O environment overlooking interstitial voids undergoes a progressively stronger strain.

By considering the behavior of peak temperature in C_P/T^3 as a function of density (*Figure 33*), higher values in correspondence of greater densities reveal a strong sensitivity of the boson peak modes to the structural scale involving the voids force fields.

In the light of these evidences, it can be believed that vibrations merging into the boson peak arise from low atomic density regions and that they are strongly affected by constraints imposed by the density on transverse displacements of structural units overlooking these voids.

Therefore, the decrease in the intensity of the boson peak, clearly observable in Figure 26 and 30, would be the natural consequence of a transfer of these modes toward higher frequencies. Indeed, the densification, giving rise to stronger Coulombian bonds, determines a shift and to a considerable reduction in the amount of low-energy vibrations.

5.5 Structural and low energy–dynamical correlations in densified borate glasses

As pointed out by the presence of the first sharp diffraction peak (FSDP) in X-ray and neutron structure factor S(Q) of vitreous systems, a regularity in the structural order is supposed to exists beyond second nearest neighbors. The FSDP is indeed a manifestation of the structural peculiarities in the intermediate-range scale and its position, Q_1, provides an estimation of the related length scale:

$$R \approx \frac{2\pi}{Q_1} \tag{19}$$

On the other hand, the characteristic low-frequency modes in Raman and inelastic neutron scattering measurements (the Boson peak) have associated wavelengths lying just in the same length scale. Many scientists assume that the boson peak is the result of quasi-local excitations, characterized by a correlation radius (47; 48) defined by

$$\omega_{\max} \approx \frac{v_T}{2\pi c R_C} \tag{20}$$

where v_T is the transverse sound velocity and c is the velocity of light.

R_C is the dynamic correlation length and represents the range over which the system can be considered homogeneous for the phonons and for the light that they scatter (49).

Several model have suggested the existence of a strict connection between structural correlations on the mesoscopic length scale and low-energy dynamics (48; 49; 50; 51; 52) in glass systems.

In order to test the validity of these assumptions, the correlation length R (estimated by Equation 19) related to the FSDP position has been compared

in Figure 40 to the correlation length R_C associated to the boson peak in Raman spectra (estimated by Equation 20).

Samples	ω'_{BP} (cm^{-1})	Q_1 ($Å^{-1}$)	R_C (Å)	R (Å)
v-B2O3	26	1.58	3.74	3.97
B2O3-2GPa	37	1.74	3.07	3.61
B2O3-4GPa/B3	51	1.83	3.14	3.43
B2O3-4GPa/B4	68	1.85	2.85	3.39

Table 6. Frequencies of the boson peak maximum and parameters related to the FSDP in normal v-B2O3 and densified glasses. The related correlation lengths are also provided.

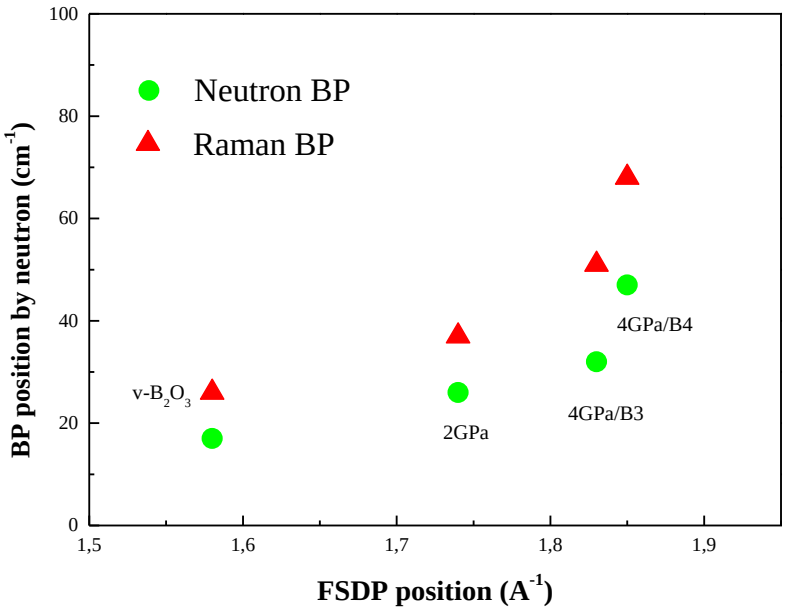

Figure 39. The boson peak frequencies, obtained by means neutron and Raman measurements as a function of the FSDP position.

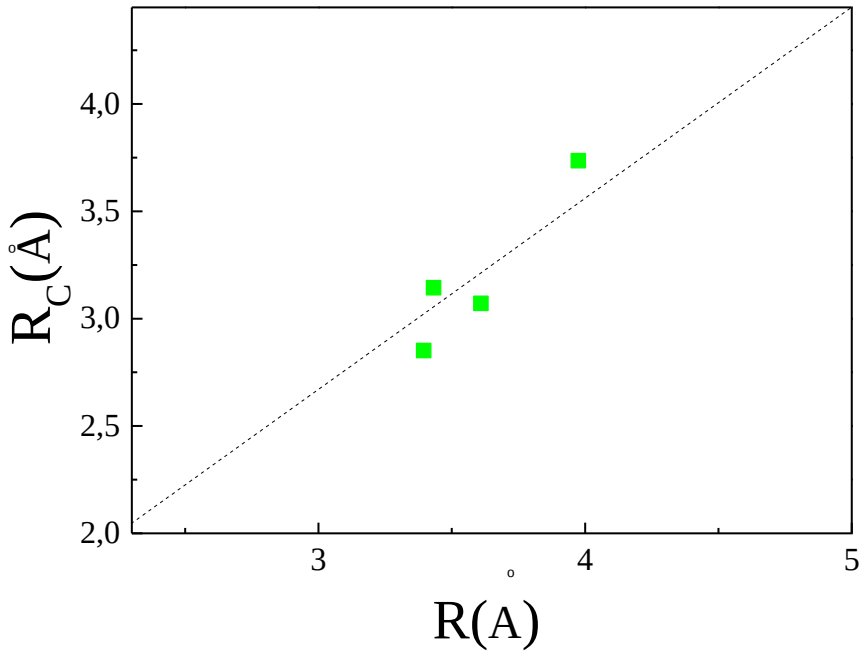

Figure 40. Correlation lengths R as obtained from Q_1 as a function of the dynamic correlation length R_C; the values are showed in Table 6.

.

This analysis shows that a strong correlation exists between the two lengths, supporting the hypothesis of the presence in glasses of strong localization of low-frequency vibrational excitations.

The values of the correlation lengths R_C become smaller by increasing the density, denoting a loss of correlation in the arrangement of densified systems. It could mean that the density causes the shrinkage of the network and provides an additional chemical disorder.

The sample densified at 4 GPa (4 GPa /B3 and 4 GPa/B4) does not show any important change in Q_1. This is due to the fact that the related length of the vitreous structure is formed in the supercooled melt and does not depend on the melting temperature, but on the quenching pressure, in accordance

with previous studies in glass-forming liquids and rapidly quenched glasses (53; 54).

This finding implies that the correlation length R_C of vitreous structures in the intermediate-range scale is closely related to some characteristic distances R between the underlying structural units contributing to the FSDP in the diffraction pattern (48).

We are thus led to conclude that in vitreous materials a structural order on a scale of 4-10 Å exists, which is responsible of the FSDP in S(Q) and determines the appearance of quasi-local vibrational excitations responsible of the BP.

5.6 In situ high-pressure study of α-quartz by Raman spectroscopy

As widely described in the previous chapters, amorphous solids are thermodynamically metastable and can be crystallized into one or more metastable or stable polycrystalline phases upon thermal annealing or high-pressure application. Thus, pressure is a thermodynamic variable that can be used to control the crystallization of amorphous solids.

The application of an external pressure remarkably enhances the thermal stability of the amorphous solids and promotes the formation of crystalline phases with larger densities. The transformation from amorphous to crystal phase involves a negative total volume change and inevitable plastic deformations that may create atomic defects giving rise to heterogeneous nucleation of the crystalline phase.

Thus, the study of the transformations from amorphous to crystal under pressure-application can provide a powerful way to shed light on some fundamental issues of glasses.

On the other hand, the investigation of pressure-induced solid-state amorphization is another important field of research in phase transitions at high pressure.

The number of substances found to become amorphous under high pressure is steadily increasing. In some solids, the amorphization is an irreversible process, with the sample remaining amorphous upon pressure release, while in others the crystal-to-amorphous transition is a perfectly reversible process.

In spite of the high level of research activity in the field, many features of pressure-induced amorphization are still unclear.

In a pressure induced amorphization process, the initial crystalline order may break down by means three different mechanisms: mechanical deformation, chemical decomposition and crystallographic transformation.

The first mechanism implies a non-homogeneous macroscopic deformation of the crystalline sample by non-hydrostatic shear components, preserving the short-range chemical order. The second mechanism implies the decomposition of an initially complex compound into simpler components. Finally, the crystallographic mechanism leads to a disorder in the crystal structure, both orientational and positional, but without any substantial atomic displacement or diffusion and without changes in the initial chemical composition. The final disordered isotropic state should be considered as a new phase (stable or metastable).

It appears clear that pressure-induced crystallization and pressure-induced amorphization are two sides of the same coin. The investigations of both issues can provide a deeper understanding of glassy properties and of the role of structural defects and shear instability in originating the Boson Peak.

Among the most studied substances found to become amorphous under high pressure there is the α-quartz. At room temperature and for pressures up to 3 GPa, α-quartz is the stable form of silica. At higher pressures, the quartz structure persists as a metastable state, which gradually transforms to an amorphous form in the 25-35-GPa range.

In the following, the results of a high pressure Raman investigation on α-quartz will be described. This represents a preliminary study of a pressure-induced amorphization process. At the same time, it is the first experiment in which a Diamond Anvil Cell has been used as experimental strategy to perform in situ pressure-investigations at the laboratories of the Physics Department of the University of Messina.

Room-temperature Raman spectra of α-quartz was carried out in the range 0 -26 GPa.

The pressure inside DAC cell has been determined by monitoring the wavelength of the characteristic fluorescence line of two different ruby grains (15 and 20 μm diameters), according to the Mao-Bell equation (55):

$$\boldsymbol{P\ (GPa) = \frac{A}{B}\left[\left(\frac{\lambda}{\lambda_0}\right)^{B} - 1\right]} \qquad \textbf{(21)}$$

where P is expressed in GPa, A is a parameter equal to 1904 GPa, λ_0 is the wavelength of the ruby fluorescence line R1 at room-pressure and temperature (694.25 nm); the B parameter is equal to 7.665 (quasi-hydrostatic conditions).

In Figure 41, the ruby fluorescence spectra at some of the investigated pressure are shown. The R lines shift at higher wavelenghts by increasing the applied pressure. The uncertainty on pressure measurements increases with pressure because of the loss of liquid hydrostaticity, as deductible in the line R enlargement.

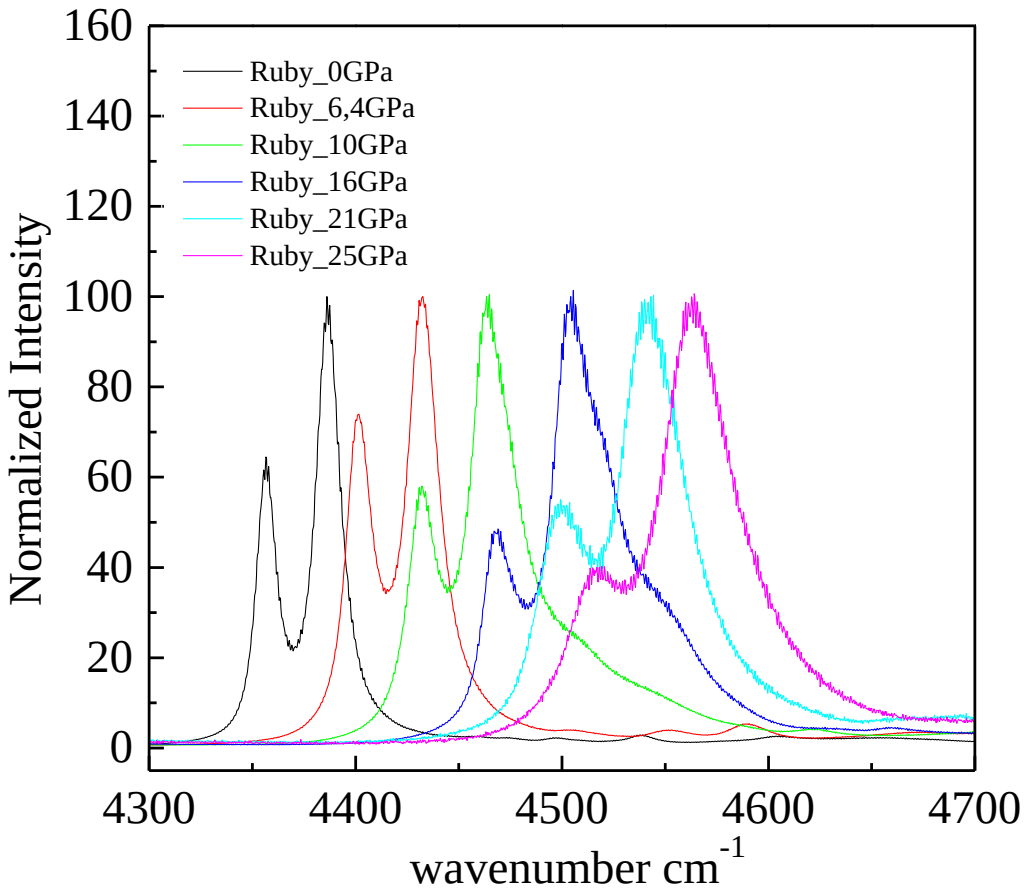

Figure 41. Emission spectra of the ruby grains inside the DAC cell at different pressures. The background-subtracted data are normalized to the R1 line intensity.

In Figure 42 the in situ Raman spectra of α-quartz at 0 GPa, 3,7 GPa, 7,5 GPa and 22 GPa are plotted. The frequency changes appear negligible for the modes 304, 393, 402 cm^{-1}. Conversely, a strong pressure dependence is observed for the modes 204, 263 and 463 cm^{-1}, that show a large initial increase of the frequency and a rapid flattening at higher pressure.

Figure 43 shows the Raman shifts as a function of pressure of six low frequency-vibrational modes.

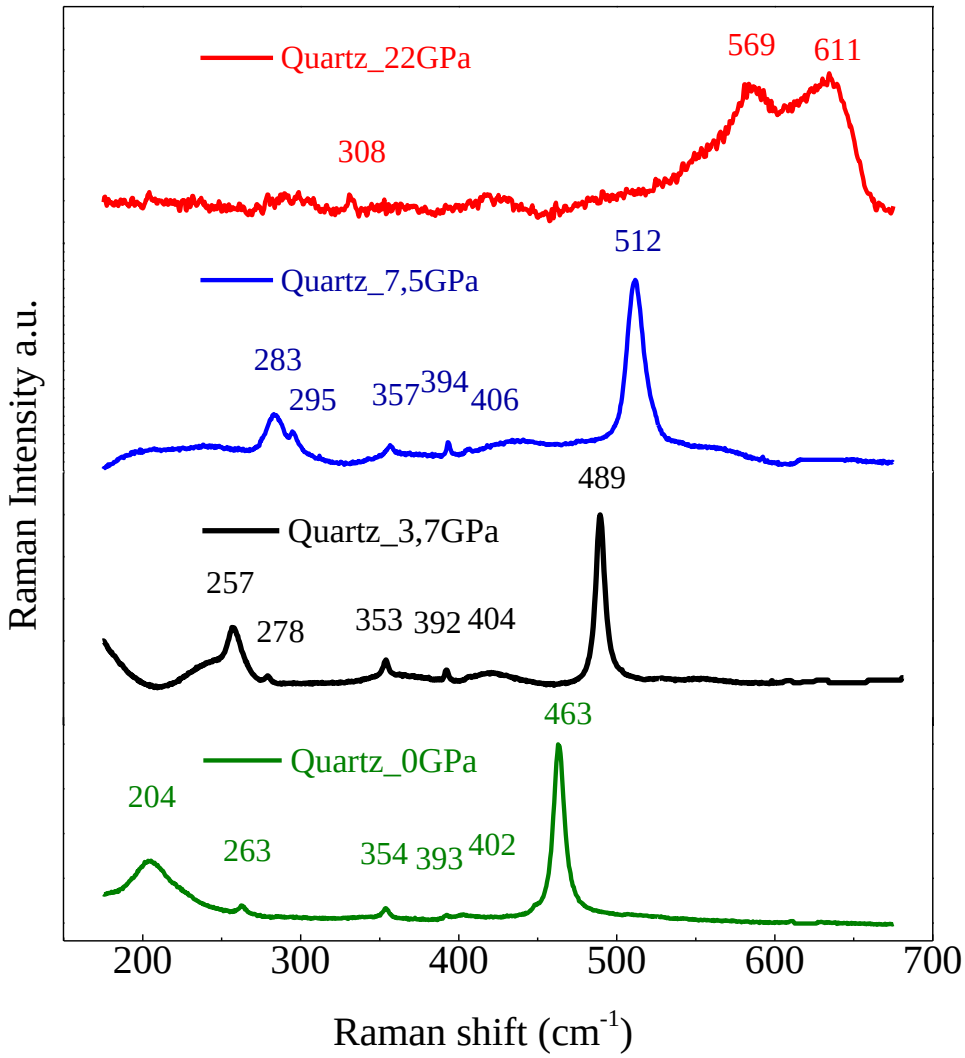

Figure 42. Effect of pressure on low frequency Raman spectra of α-quartz.The high-pressure data sets have been shifted vertically for clarity of presentation.

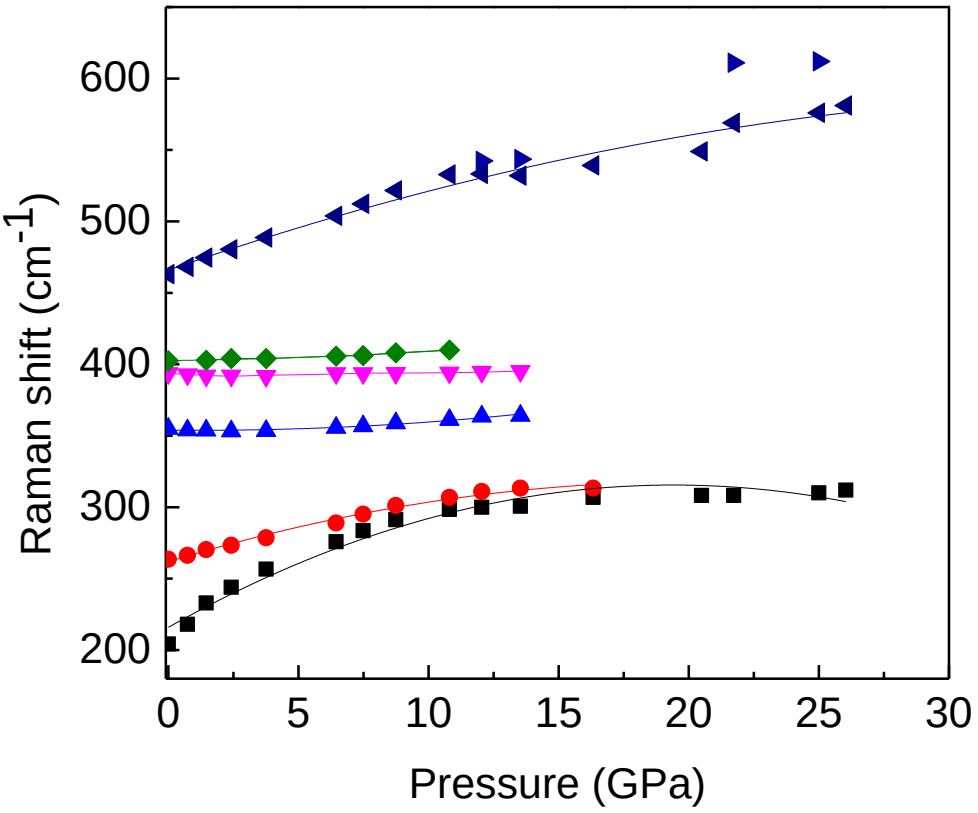

Figure 43. Frequency shifts of the Raman active modes in α-quartz as a function of pressure.

The variations in vibrational spectra are inferable to pressure-induced changes in structure of α-quartz. In the investigated low frequency range, they are ascribed to complex translations and rotations of SiO_4 tetrahedra (56).

Particularly, the strongest band at 463 cm^{-1} is ascribed to the symmetric Si-O-Si stretching modes and depends on the smallest ring sizes (and therefore smallest $\Theta_{Si\text{-}O\text{-}Si}$ angles) in the structure (57). The compression generates the reduction of the Si-O-Si angle, which has been shown to decrease from 144° under ambient conditions to 134° at 6 GPa (58), involving the observed consistent increase of frequency.

References

1. *J. W. Zwanziger, Solid State Nucl. Magn. Reson. 27, 5 (2005).*

2. J. Swenson, L. Borjesson, and W. S. Howells, Phys. Rev. B 52, 9310 (1995).

3. D. L. Price, et al., Phys. Rev. B 55, 11249 (1997).

4. J. Zhong and P.J. Bray, J. Non-Cryst. Solids 111, 67 (1989).

5. A.P. Sokolov, A. Kisliuk, M. Soltwisch and D. Quitmann, Phys. Rev. Lett. 69, 1540 (1992).

6. L. Börjesson, et al., Phys. Rev. B 39, 3404 (1989).

7. G. D'Angelo, et al., J. Phys. Chem. 114, 12565 (2010).

8. C.E. Stone, A.C. Hannon, T. Ishihara, N. Kitamura, Y. Shirakawa, R.N. Sinclair, N. Umesaki and A.C. Wright, J. Non-Cryst. Solids 293, 769 (2001).

9. A. Pasquarello and R. Car, Phys. Rev. Lett. 80, 5145 (1998).

10. L. Giacomazzi, et al., Phys. Rev. Lett. 95, 075505 (2005).

11. M. Micoulaut, et al., J. Phys.: Condens. Matter 18, R753 (2006).

12. M. Micoulaut, et al., Phys. Rev. B 88, 054203 (2013).

13. S. R. Elliott, J. Chem. Phys. 103, 2758 (1995).

14. M. Zanatta, et al., Phys. Rev. Lett. 112, 045501 (2014).

15. C. E. Stone, et al., J. Non-Cryst. Solids 293, 769 (2001).

16. Q. Mei, et al., Phys. Rev. B 74, 014203 (2006).

17. N. Kitamura, et al., J. Non-Cryst. Solids 274, 244 (2000).

18. E. Lorch, J. Phys. C: Solid State Phys. 2, 229 (1969).

19. A. Zeidler, et al., Phys. Rev. B, 90-2, 024206 (2014).

20. A. C. Hannon et al., J. Non-Cryst. Solids 177, 299 (1994).

21. U. Buchenau, N. Nücker, and A. J. Dianoux, Phys. Rev. Lett. 53, 2316 (1984).

22. A. P. Sokolov, et al., Phys. Rev. Lett. 71, 2062 (1993).

23. G. Carini Jr, G. Carini, G. D'Angelo, et al., Phys. Rev. Lett., 111-24, 245502 (2013).

24. P. A. V. Johnson, A. C. Wright, and R. N. Sinclair, J. Non-Cryst. Solids 50, 281 (1982).

25. G. Carini, Jr., E. Gilioli, G. Tripodo, and C. Vasi, Phys.Rev. B 84, 024207 (2011).

26. G. E. Gurr, et al., Acta Crystallogr. Sect. B 26, 906 (1970).

27. R. Shuker, R. W. Gammon, Phys. Rev. Lett. 25, 222 (1970).

28. G. Carini, et al., Phys. Rev.B 47, 3005 (1993).

29. A. Fontana, et al., Phys. Rev. Lett. 78, 1078 (1997).

30. N.V. Surovtsev, Jet al., J. Chem. Phys. 112, 2319 (2000).

31. X. Liu, et al., Z. Phys. B 99, 49 (1995).

32. L. Orsingher, et al., J. Chem. Phys. 132, 124508 (2010).

33. G. D'Angelo, et al., Phys. Rev. B, 79-1, 014206 (2009).

34. R. O. Pohl, Topics in Current Physics, 24, 27-52 (1981).

35. A. J. Martin, W. Brenig, Phys. Status Solidi B 64, 163 (1974).

36. E. Duval, et al. Philos. Mag. B 79, 2051 (1999).

37. E. Saviot, N. Duval, Phys. Rev. B 60, 18 (1999).

38. N. V. Surovtsev, A. P. Sokolov, Phys. Rev. B 66, 054205 (2002).

39. B. Hehlen, et al., Phys. Rev. Lett. 84, 5355 (2000).

40. V. L. Gurevich, D. A. Parshin and H. R. Schober, Phys. Rev. B 71, 014209-4 (2005).

41. S. I. Simdyankin, et al., Phys. Rev. B 65, 104302 (2002).

42. J. Harris, et al., Physica B 263-264, 357 (1999).

43. Y. Li, et al., Phys. Rev. B 74, 052201 (2006).

44. D. J. Safarik, R. B. Schwarz, and M. F. Hundley, Phys. Rev. Lett. 96, 195902 (2006).

45. R. O. Pohl, X. Liu, and E. Thompson, Rev. Mod. Phys. 74, 991 (2002).

46. B. Bridge and A. Higazy, Phys. Chem. Glasses 27, 1 (1986).

47. Duval, A. Boukenter, and T. Achibat, J. Phys, Condens. Matter 2, 10227 (1990).

48. A. P. Sokolov, et al. Phys. Rev. Lett. 69-10, 1540 (1992).

49. S. Chakraborty, et al. Journ. of Alloys and Compounds, 713, 95 (2017).

50. L. Börjesson, et al., Phys. Rev.Lett. 70-9, 1275 (1993).

51. A.S.Ahmad et al., J Low Temp Phys, 186-1, 172 (2017).

52. S. R. Elliott, Europhys.Lett., 19-3, 201 (1992).

53. M. Kriiger, et al.,J. Chem. Phys. 96, 7352 (1992).

54. V. K. Malinovsky, V. N. Novikov, A. P. Sokolov, Phys. Lett. A 123, 19 (1987).

55. H. K. Mao, P. M Bell, J. Shaner, D. J. Steinberg, Appl. Phys. 49, 3276 (1978).

56. R. J. Hemley, High-Pressure Research in Mineral Physics, 347 (1987).

57. S. K. Sharma et al., Nature, 292, 140 (1981).

58. L. Levien, C. T. Prewitt, Am. Mineral., 66, 324 (1981).

Conclusions

The vibrational dynamics and structural properties of a series of alkaline borate glasses, permanently densified B_2O_3 glasses and an α-quartz have been investigated. Furthermore, a set-up for in-situ high-pressure Raman experiments was developed.

Permanently densified B_2O_3 samples were obtained by using a high-pressure-high temperature apparatus achieving a densification up to the 30%.

The low energy vibrational dynamics and the structure were investigated by means inelastic neutron scattering, low temperature specific heat, Raman scattering and neutron diffraction.

The neutron diffraction spectra of the series of alkaline borate glasses showed the existence of strong differences in the intermediate range order as a function of the specific alkaline ion and of its concentration. It was found that the shape of the structure factor of alkaline borate glasses in the low-Q region emerges as a result of the existence of two length scales associated with the diameter of voids. A model is proposed in which the planar section of a void is an n-membered ring of all-side vertex sharing basic structural units. This description explains the anomalous compositional and pressure dependence of the FSDP in glasses as due to changes in the distribution of the sizes of the voids.

The analysis of the diffraction spectra of the densified B_2O_3 shows that the position of the FSDP moves to a higher momentum transfer, as the pressure is increased, providing indication of the change of the intermediate range order, whereas the short-range order remains unchanged.

The changes in the FSDP (shift in the position, reduction in its height) are due to a shrinkage of the structural voids.

Finally, the comparison of the S(Q) between glasses and corresponding crystals shows that diffraction lines for the crystalline phase are found in the same region where the FSDP is observed in glasses. We suggest that the width of the FSDP is caused by the overlapping of several broadened peaks that arise from voids of irregular shape and different size.

The detailed analysis of the Boson peak in densified B_2O_3 glasses, obtained by neutron, Raman and specific heat, demonstrates that under pressure (i) the boson peak position shifts more strongly than the sound modes, (ii) the intensity of the boson peak relative to the Debye level increases.

These results clearly indicate that changes in the boson peak are stronger than the elastic medium expectation, and that they are ascribed to a suppression of the low-frequency modes. The observed independence of the scaled spectral shape (spectra normalized by the intensity of BP at the maximum) suggests that the vibrations in glasses form a universal distribution and change in a similar way under compression. In other words, all the low-energy vibrational modes underlying the BP, extended and localized, are coupled and hybridized, determining an overall spectral distribution, whose spectral shape does not depend on the different packing fractions of the systems. Furthermore, a clear correlation between the boson peak frequency (or the temperature of the maximum in C_p/T^3) and the transverse sound velocity is found.

The Raman coefficient $C(\omega)$ has been evaluated and it appears almost similar for all glasses. Moreover, it is demonstrated that above the boson peak maximum, $C(\omega)$ has a linear dependence on frequency, $C(\omega)=A(\omega/\omega_{BP}+0,5)$ and a superlinear behaviour at frequencies below ω_{BP}.

It is believed that vibrations merging into the boson peak arise from low atomic density regions and that they are strongly influenced by constraints imposed by the densification on transverse displacements of structural units

overlooking these voids. These findings suggest a mainly transverse character of the excess vibrational modes in glasses.

The correlation lengths of densified glasses, estimated from the boson peak in Raman spectra and from the position of the first sharp diffraction peak, were compared. This comparison shows that these two lengths, which are respectively based on dynamic and static properties, are in good quantitative agreement. The present finding suggests that the low-frequency excitations are defined by the characteristic length of voids in the glassy structure. The large suppression of the low-energy dynamics is thought to be related to the shrinkage of the void space. Soft modes in the void space can plausibly be suppressed by its shrinkage.